Università degli studi di Napoli Federico II

Scuola Politecnica e delle Scienze di Base

Department of Industrial Engineering

PH.D. SCHOOL IN INDUSTRIAL ENGINEERING – XXXV CYCLE

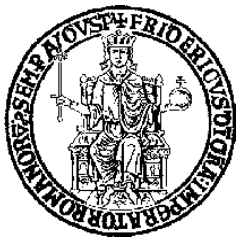

Doctoral Thesis

Advanced predictive combustion model for heavy-duty CNG fuelled engines

Ph.D. School Coordinator

Prof. Michele Grassi

Tutor:
Prof. Fabio Bozza
Prof. Vincenzo De Bellis
Dr. Ing. Carlo Beatrice

Ph.D. Candidate:
Marco Riccardi

Contents

Acknowledgments

Questa tesi di dottorato segna la fine di un percorso lungo ma anche pieno di soddisfazioni e ciò non sarebbe stato possibile senza il supporto di molte persone che ho il dovere ed il piacere di ringraziare.

Desidero innanzitutto ringraziare il mio tutor, il Dr. Carlo Beatrice, dirigente di ricerca presso il CNR-STEMS, per aver creduto in me concedendomi l'opportunità di lavorare su tematiche interessanti e di alto livello. Egli, nonostante diviso tra tanti progetti di ricerca, è sempre stato disponibile a confronti sicuramente illuminanti dal punto di vista scientifico.

Vorrei ringraziare, inoltre, il prof. Fabio Bozza, tutor di questo dottorato e docente durante il periodo di università, per la sua dedizione e esperienza scientifica, senza la quale questo percorso di dottorato non avrebbe visto la luce.

Un sincero ringraziamento va al prof. Vincenzo De Bellis che mi ha accompagnato fino alla fine di questo percorso con la sua professionalità, competenza e infinita pazienza, trovando sempre un momento per un confronto con me.

Devo inoltre ringraziare il Dr. Ing. Lorenzo Sforza e il prof. Tommaso Lucchini per il loro preziosissimo contributo scientifico durante la mia attività di ricerca.

Un grande ringraziamento va anche al Dr. Ing. Simon Langridge e al Dr. Ing. Mohsen Mirzaeian, che sono stati miei tutor durante il mio periodo all'estero presso FPT Motorenforschung AG, per il loro rigore scientifico, spessore umano e per la loro incredibile professionalità. Aver trascorso il mio periodo all'estero nel loro gruppo di ricerca ad Arbon è stato un pregio.

Un vivo grazie va anche al prof. Per Tunestal, dell'Università di Lund, per essere stato di fondamentale supporto durante l'attività di ricerca.

Un sentito ringraziamento va anche agli Ing. Diego Iudice e Michele Lopez, per essere stati sempre disponibili a chiarimenti su specifici test o simulazioni durante la mia attività di ricerca.

Ringrazio i miei amici, che in un modo o nell'altro sono sempre fonte di spensieratezza, avendomi dato la possibilità di alleggerire il carico durante questi anni.

Ringrazio mia mamma, mio fratello e la mia famiglia tutta per avermi supportato e sopportato durante questi anni, ma non solo.

Ringrazio quindi tutti, chi c'è e chi c'è stato; se sono giunto qui è grazie a tutte le persone che ho incontrato nella mia vita finora.

List of figures

List of tables

List of publications

- Riccardi, M., Tufano, D., Beatrice, C., Bozza, F. et al., "Toward Predictive Combustion Modeling of CNG SI Engines in 1D Simulation Tools," SAE Technical Paper 2020-01-2079, 2020, https://doi.org/10.4271/2020-01-2079.
- C. Beatrice, C. Capasso, S. Doulgeris, M. Riccardi, Z. Samaras and O. Veneri, "Model based evaluation of lithium ion capacitors use and management for plug-in hybrid vehicles," 2021 IEEE Vehicle Power and Propulsion Conference (VPPC), 2021, pp. 1-7, doi: 10.1109/VPPC53923.2021.9699329.
- Riccardi, M., De Bellis, V., Sforza, L., Beatrice, C. et al., "Advanced Turbulence Model for SI Combustion in a Heavy-Duty NG Engine," SAE Technical Paper 2022-01-0384, 2022, https://doi.org/10.4271/2022-01-0384.
- Riccardi M, De Bellis V, Sforza L, Beatrice C, Bozza F, Mirzaeian M. Advanced turbulence and combustion modeling for the study of a swirl-assisted natural gas spark-ignition heavy-duty engine. International Journal of Engine Research. 2023;0(0). doi:10.1177/14680874221150469
- Riccardi, M., De Bellis, V., Sforza, L., Tunestal., P., et al., " Experimental and numerical analysis of an active pre-chamber engine fuelled with natural gas," SAE Technical Paper 2023 (*in publishing*)

Abbreviation and nomenclature

Acronyms

0D/1D/3D	Zero/One/Three–Dimensional
AFTDC	After Firing Top dead center
BEV	Battery Electric Vehicle
BFTDC	Before Firing Top dead center
BMEP	Brake mean effective pressure
BSFC	Brake specific fuel consumption
CAD	Crank angle degree
CCV	Cycle to Cycle Variation
CFD	Computational Fluid Dynamics
CI	Compression Ignition
CNG	Compressed Natural Gas
CoV	Coefficient of Variation
DI	Direct Injection
ECU	Engine Control Unit
EGR	Exhaust Gas Recirculation
EOI	End of Injection
EU	European Union
FMEP	Friction Mean Effective Pressure
FTDC	Firing Top dead center
GHG	Green-House Gas
GWP	Global Warming Potential
HCCI	Homogeneous Charge Compression Ignition
HD	Heavy Duty
HEV	Hybrid Electric Vehicle
ICE	Internal Combustion Engine
IMEP	Indicated Mean Effective Pressure
IMPO	Integral of Modulus of Pressure Oscillations
LNG	Liquefied Natural Gas
MAPO	Maximum Amplitude of Pressure Oscillations
MBT	Maximum Brake Torque
MC	Main-Chamber
MFB	Mass fraction burned
MPI	Multi Point Injection
PC	Pre-Chamber
PFI	Port Fuel Injection
PHEV	Plug-in Hybrid Electric Vehicle
PTG	Power-to-Gas

RMSE	Root Mean Square Error
SA	Spark advance
SACI	Spark-Assisted Compression Ignition
SCE	Single-Cylinder Engine
SI	Spark ignition
SOI	Start Of Injection
TCO	Total Cost Ownership
TDC	Top Dead Center
TJI	Turbulent Jet Ignition
TKE	Turbulent Kinetic Energy
TWC	Three-Way Catalyst

Latin Symbols

A_L	Flame front laminar area
A_T	Flame front turbulent area
B	Cylinder bore
C_1, C_2, C_3, C_{tumb}	Tuning constants of K-k-eps turbulence model
$c_{fd0,S}$, $c_{fdm,S}$	Tuning constants of swirl decay function
$c_{fd0,T}$, $c_{fdm,T}$	Tuning constants of tumble decay function
c_{jet}	Fresh charge entrainment multiplier for the combustion model
c_k	Flame kernel growth multiplier
c_{Kin0}	Tuning constant of inlet flow coefficient
c_{PKk}	Tuning constant of turbulent production
$c_{r0,S}$, $c_{rm,S}$	Parameters for swirl radius adjustment
$c_{r0,T}$, $c_{rm,T}$	Parameters for tumble radius adjustment
c_s	Turbulent speed multiplier
c_{Sin}, c_{Sex}	Tuning constants of swirl flow coefficient
C_T	Tumble coefficient
c_t	Taylor length multiplier
c_{Tin0}	Tuning constant of tumble flow coefficient
c_{trans}	Laminar turbulent transition multiplier for the combustion model
c_{wc}	Wall combustion tuning multiplier for the combustion model
c_{wrk}	Wrinkling multiplier for the combustion model
D_3	Flame front fractal dimension

d_{bowl}	Piston bowl diameter
e	Internal energy
E	Energy
f	Function
$f_{d,S}$	Decay function of swirl
$f_{d,T}$	Decay function of tumble
H	Piston position referred to cylinder head
K	Turbulent kinetic energy
K	Mean flow kinetic energy
K_S	Kinetic energy related to swirl motion
K_T	Kinetic energy related to tumble motion
L_g	Geometric length scale
L_{max}	Flame wrinkling maximum scale
L_{min}	Flame wrinkling minimum scale
L_t	Integral Length Scale
m	Mass
N_{swirl}	Swirl number
N_{tumble}	Tumble number
P	Turbulence production
p	Pressure
P_k	Production of turbulent kinetic energy
P_ε	Production of dissipation rate
r_f	Flame radius
r_S	Swirl radius
r_T	Tumble radius
S	Swirl momentum
s_{bowl}	Piston bowl height
S_L	Laminar flame speed
S_{L0}	Unstretched Laminar flame speed
S_T	Turbulent flame speed
T	Time
T	Temperature, Tumble momentum
t_S	Characteristic time scale of swirl
t_T	Characteristic time scale of tumble
t_{TS}	Weighted average characteristic time scale
U	Mean flow velocity
u'	Turbulence intensity
U_a	Axial mean flow velocity
U_r	Radial mean flow velocity
U_S	Swirl velocity
U_{sq}	Squish velocity
U_T	Tumble velocity, turbulent flame speed
v	Flow velocity throughout the valve

$V(\theta)$	Instantaneous combustion chamber volume
V_{cyl}	Cylinder volume
X_{EGR}	Mass Fraction of Residual Gas

Greek Symbols

α	Temperature ratio exponent of laminar flame speed correlation
β	Pressure ratio exponent of laminar flame speed correlation
ε	Dissipation rate
λ	Relative air-to-fuel ratio
Λ_T	Taylor length scale
ν_t	Turbulent viscosity
ρ	Density
φ	Air/fuel equivalence ratio
ω	Angular velocity

Subscripts

0	Room conditions
10 / 50 / 90	Referring to 10 / 50 / 90% of mass fraction burned
b	Burned
cyl	Related to the cylinder
eng	Referred engine
entr	Entrainment
exb	Backward flow through the exhaust valve
exf	Forward flow through the exhaust valve
fractal	Related to fractal approach
inb	Backward flow through the intake valve
inc	Incoming flow inside the cylinder
inf	Forward flow through the intake valve
inj	Injected
jet	Related to turbulent jet
K	Related to mean flow kinetic energy
max	Maximum value
min	Minimum value
out	Outcoming flow from the cylinder
S	Related to swirl motion
T	Related to tumble motion

u	Unburned

Superscripts

.	Temporal derivative

Abstract

The problem of atmospheric air pollution, caused by the Internal Combustion Engines (ICEs), has never been greater than today. As a result of increasingly rigorous regulations, car manufacturers are continually compelled to discover appropriate technical solutions to meet this issue, without sacrificing engine performance requirements. Specifically, the new CO_2 emission limit for 2026, with a target of 80 g/km of CO_2 along the WLTC, has never pushed automobile manufacturers so hard to find creative and clean solutions to increase the fuel economy of vehicle fleets. However, the solution to this dilemma is still a matter of contention. To drive engine development and reduce the time-to-market, the employment of numerical analysis is mandatory. This requires a continuous improvement of the simulation models toward real predictive analyses able to reduce the experimental R&D efforts.

In this framework, 1D numerical codes are fundamental tools for system design, energy management optimization, and calibration. The simulation efforts carried out to assess the previous objectives is mainly affected in a 0D/1D modelling environment, where the whole engine system is schematized through a network of 1D pipes and 0D cylinders, the latter described in term of in-house developed quasi-dimensional models of the in-cylinder phenomena.

The present research activity is focused on the improvement of the phenomenological turbulence model, originally conceived to describe turbulence evolution in tumble-promoting engines. The turbulence model is developed with reference to a SI heavy-duty CNG engine derived from a diesel engine. In this architecture, due to the flat cylinder head, turbulence is also generated by swirl and squish flow motions, in addition to tumble motion. The presented turbulence model is validated against 3D CFD results, demonstrating to properly predict turbulence and *swirl*/*tumble* evolution under two different operating conditions, without the need for any case-dependent tuning.

The developed turbulence model is coupled to a phenomenological combustion model based on the fractal geometry theory applied to the flame front surface, where the turbulence is assumed to support flame propagation through an enhancement of the flame front area with respect to the laminar counterpart.

The above phenomenological model is applied for two engines: a Spark Ignition (SI) diesel-derived heavy-duty engine and an ultra-lean active pre-chamber engine.

Using a unique engine-dependent set of tuning constants, the validity of the global simulation models for both engines is evaluated by comparisons with 3D or experimental data, using a unique engine-dependent set of tuning constants.

In order to determine the optimal values of each control variable in the whole operating plane, a Rule-Based (RB) calibration technique has been adopted in both models.

The content of this doctoral thesis is divided into three macro areas.

The first part concerns an overview of internal combustion engine with a focus on the turbulent combustion theory for SI and active pre-chamber ultra-lean engines.

In the second part, an extensive exposure of the developed advanced turbulence and combustion models is presented.

In the last part, the assessment of the advanced turbulence model for a SI heavy-duty and ultra-lean pre-chamber engines is carried out. The extensive available database permitted to confirm the above-mentioned models' reliability.

Calibration of these models towards the fully-virtual vehicle design, which represents one of the next steps in this extensive research activity, is required to support engine development and meet the restrictive emission regulations.

1 Introduction

1.1 Background

In the recent years, the climate change and global warming are considered the most challenging problems that our societies need to face. The economic boom caused by industrial development has resulted in an unprecedented and accelerated worldwide change, which has had a substantial effect on air pollution and attendant health hazards [1]. The solution to these challenging issues requires a series of coordinated actions, including an increase in the proportion of renewable energy sources, a reduction in the use of carbon-based fuels, improvements in energy conversion efficiency, and structural changes to the economy, all of which are driven and supported by the introduction of stringent legislation.

The Paris Agreement has established a legally binding global mechanism for CO_2 reduction commitments. It was adopted by 196 Parties at the XXI Conference of the Parties of the United Nations Framework Convention on Climate Change, on December 2015 [2]. This agreement requires all countries to set emissions reduction commitments. It establishes a long-term objective of keeping the rise in global average temperature well below 2 °C over pre-industrial levels. However, according to experts, the promises are insufficient to avert a 1.5 °C increase in the world average temperature.

From 1990 to 2020, Figure 1.1a depicts the trend of Greenhouse Gas (GHG) emissions by sector. The initiatives made by the European Union (EU) throughout those years were already able to determine a constant decrease in CO_2-equivalent emissions, allowing the EU to surpass its 2020 reduction target of 20% and achieve a 21.7% reduction in GHG emissions in 2017. In 2020 it is about 34% below 1990 levels; compared to 2019, CO_2 emissions decreased by 9.9%, due to mainly the penetration of renewables and improvements in the energy efficiency [3]. Also, the Covid-19 pandemic and the associated recession contributed to the decrease measured in 2020. The lockdown measures implemented by the majority of European nations to decrease COVID-19 transmission in the spring of 2020 resulted in considerable reductions in air pollution emissions, mainly from road travel, aviation, and international shipping [4]. Greenhouse gas emissions from only transport sector account for 21.8% of the total GHG emissions in 2020, where about 95% is due to road transportation (Figure 1.1b). Since the transportation sector accounts for a huge part of global emissions, second only to energy supply and industry (40%), the only way to reach the EU's 2030 goal of a 40% reduction in greenhouse gas emissions the priority is to replace first of all fossil fuels and then to further improve all the technologies associated with this sector, especially those related to road transport.

To control GHG emissions in the road sector, emission standards on CO_2 were introduced in 2014 [5, 6], which set a CO_2 emissions standard at 95 g/km for passenger cars and 147 g/km for vans as of 2020. In the 2017, the European Commission presented a legislative proposal [7] on CO_2 limits for new cars and light commercial vehicles, that would have to be 15% lower in 2025 and 30% lower in 2030, compared to their respective limits in 2021. Regarding heavy-duty vehicles, a proposal regulation presented in 2018 [8], sets the first-ever CO_2 emission performance standards for new heavy-duty vehicles in the EU and incentivises low- and zero-emission vehicles. A "low-emission heavy-duty vehicle" is defined as a vehicle with a specific CO_2 emissions of less than 350 g/km. November 10, 2022 the EU Commission presented a proposal (Euro 7) to reduce air pollution from new motor vehicles sold in the EU to meet the European Green Deal's zero-pollution ambition, in which also minimum performance requirements for battery durability is set [9].

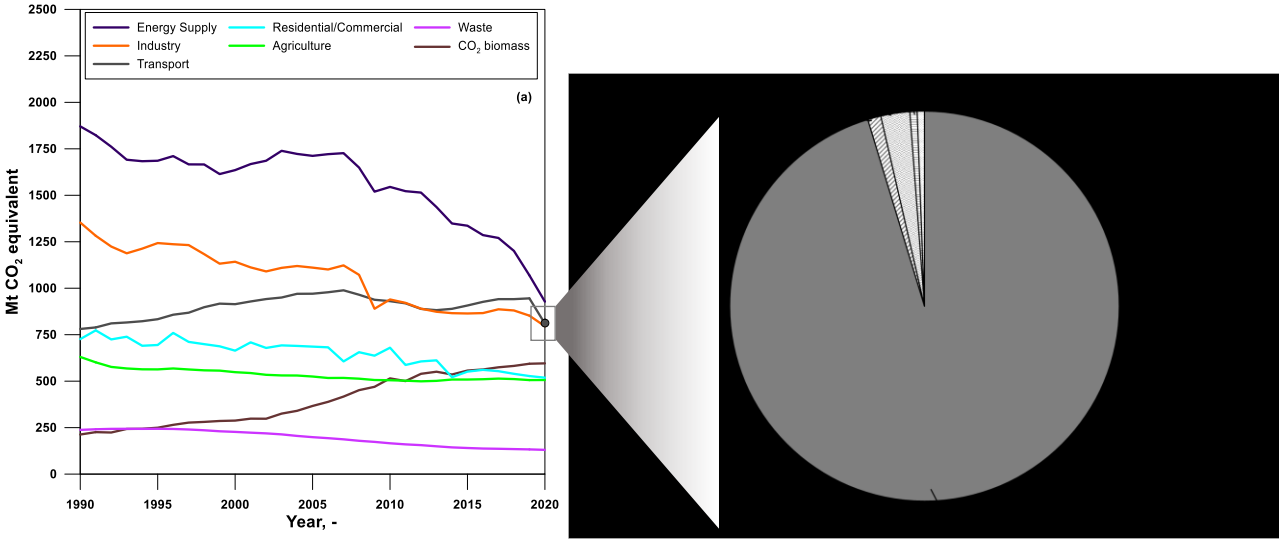

Figure 1.1 - GHG emissions by aggregated sector, Mt of equivalent CO_2 and percentage of GHG from the only transport sector (year 2020) [3]

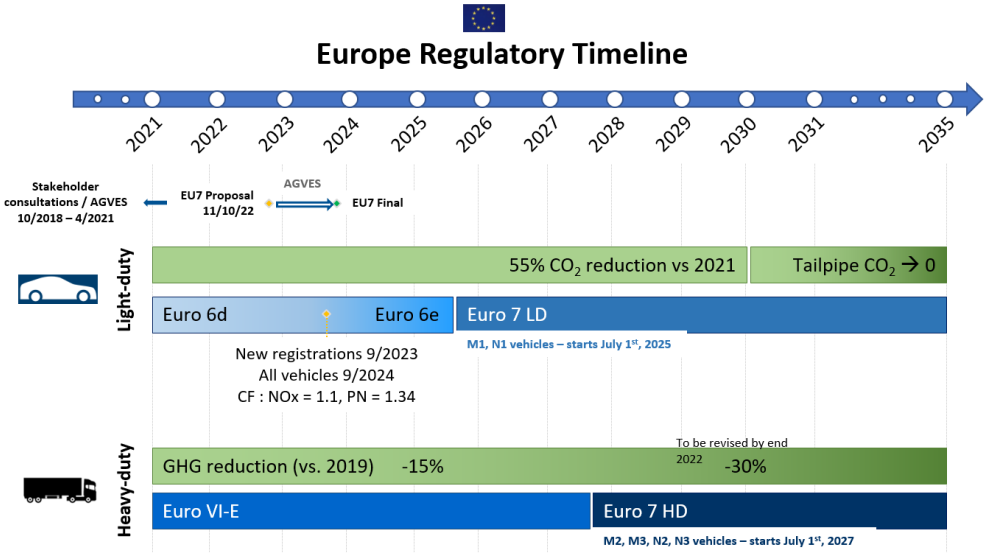

Figure 1.2 - CO_2 and pollutant emissions limits roadmap for light- and heavy-duty engines [10]

GHG emissions divided, on the year 2020, according to the type of vehicle are displayed in Figure 1.3. Passenger cars weigh about 59%, while light- and heavy-duty almost 40% together. It is, therefore, clear that research must definitely aim to develop innovative technologies and energy management systems also for these categories of vehicles.

In 2013, the U.S. Environmental Protection Agency determined that certain Volkswagen cars equipped with diesel engines emitted more than forty times the amount of NO_x claimed during laboratory testing. The company acknowledged that almost half a million vehicles were loaded with unauthorized ECU software designed to detect the regulatory approval test. This pollution crisis exploded across Europe and around the world, affecting 11 million vehicles and other automakers, including BMW, Porsche, and Audi, which were investigated [11]. This scandal affected the whole automobile industry, from Diesel to gasoline-based fuel propulsion systems, and led to the belief that Internal Combustion Engines (ICE) will be phased out within a few years owing to their inability to comply with severe EU regulations [12]. Regarding passenger cars and vans, already in 2030, more than 40% of new registrations are projected to be of zero tailpipe emission (battery electric or fuel cell H_2). The bulk of the surviving cars with internal combustion engines will be hybrids and plug-in hybrids. Regarding heavy-duty engines (trucks and buses), battery electric vehicles and fuel cells ones will gradually replace Diesel conventional technologies and they are almost split in the future. Heavy-duty engines fuelled with Compressed Natural Gas (CNG) will retain their importance over time. According to forecasts, the percentage of vehicles that will use this technology in 2050 is similar to that it could be found today [13].

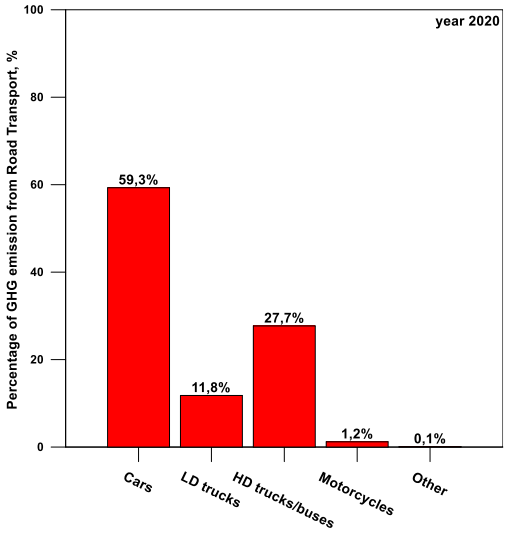

Figure 1.3 – Percentage of GHG emission from road transportation of the vehicle fleet (year 2020) [3]

To meet the requirements of future legislation, rather than a pure-electric future, an eclectic scenario comprised of technologies most suited to the context in which they are deployed should be anticipated in the next years. This implies that ICE-based vehicles, HEVs, PHEVs, BEVs, and even Fuel Cell-based vehicles will coexist on the market for an extended period, requiring automakers to overcome the limitations associated with each technology.

The performance of natural gas fuel in the heavy-duty sector is often evaluated against diesel fuel, which is the primary source of energy used by this transportation sector.

Different Natural Gas engine technologies could represent different solutions in heavy duty transportation. Each one could have a different impact on emissions reduction and engine efficiency.

The Table 1.1 below sums up the different engine technologies in heavy-duty transportation [14]. Heavy vehicles need great power and make long journeys, for these reasons the methane engine is particularly suitable.

Natural gas represents an effective alternative to the other fossil fuels thanks to the reduced pollutant and carbon dioxide emissions and considering that HC emissions exhibit a reduced photochemical reactivity and greenhouse effect with respect to conventional petroleum-based fuels. It is anyhow worth recalling that the above-mentioned positive effect could be impaired if the system fugitive emissions were to be considered. Moreover, the natural gas high anti-knock characteristic allows for increasing the compression ratio, thus boosting the engine efficiency. Still, CNG features lower burning speed and reduced volumetric efficiency with respect to liquid fuels [15].

Engine technology is pretty much the same as an Otto cycle engine with Spark Ignition, so there is no need for an overly complicated aftertreatment system for the emissions. TWC is still good for this type of engine, especially for those that work on the stoichiometric and allows to fall within the standards provided by the regulations. CNG Spark Ignition heavy-duty combustion systems commonly derive from diesel Compression Ignition (CI) engines in terms of cylinder head and combustion chamber geometry [16].

Engine technology	Current applications	Pros	Cons
Legacy Natural Gas-Lean Burn Spark Ignited	Was used only in refuse trucks and transit buses	Low PM emissions	No NO_X advantage compared to diesels, durability issues related to oil consumption
Stoichiometric Spark Ignited Natural Gas Engines	Refuse truck, transit bus, school bus, class- 8 Tractor (short delivery, port drayage)	Low PM emissions, low NO_X during in-use operation, simple aftertreatment configuration to meet optional near-zero NO_X standard	Lower range of operation compared to diesels, negative feedback from drivers related to performance
High-Pressure Direct Injection (HPDI) Dual Fuel (Compression Ignition)	Class- 8 Tractor (Inter-city goods movement)	Diesel like performance and range, lower NO_X compared to diesels	Higher cost of engine compared to diesels, engine component durability, older models were associated with LNG fuel tank venting
Diesel Engines	Refuse truck, transit bus, school bus, class- 8 Tractor (delivery, port drayage, long-haul, vocational applications)	High torque capability for heavy-payload applications, no fuelling infrastructure required by fleets, comparatively lower maintenance cost	High in-use NO_X emissions at low-load operating conditions, expensive aftertreatment configuration to meet optional near-zero NO_X standards

Table 1.1 - Summary of Engine Technology for heavy-duty vehicles fleet, Applications, Pros and Cons of each platform [14]

The use of biofuels or zero-carbon fuels, such as hydrogen, as well as the total adoption of electric vehicles (which would be completely CO_2 neutral only if strictly connected to the production of energy from renewable sources and to the management of end-of-life batteries) appear to be long-term solutions for heavy commercial vehicles that, on their own, would not be sufficient to meet the predetermined emission reduction goals. In terms of their ability to reduce greenhouse gas emissions, gaseous fuels have substantial benefits over fossil-derived fuels [17]. In 2019, the global output of natural gas reached a record high of 4088 Bcm (billion cubic meters), a 3.3% increase over 2018. Since the 2007-2008 financial crisis, natural gas output has increased at an annual compounded growth rate of 2.7%. At the level of the OECD (Organization for Economic Cooperation and Development), total natural gas output increased by 6.1%, surpassing the 1500 Bcm mark for the first time [19].

Due to these factors, as well as its wide availability in nature at competitive prices [20], the use of natural gas (NG) has become increasingly popular over the years, both in the energy production sector and as an alternative to traditional fuels for internal combustion engines in the automotive industry.

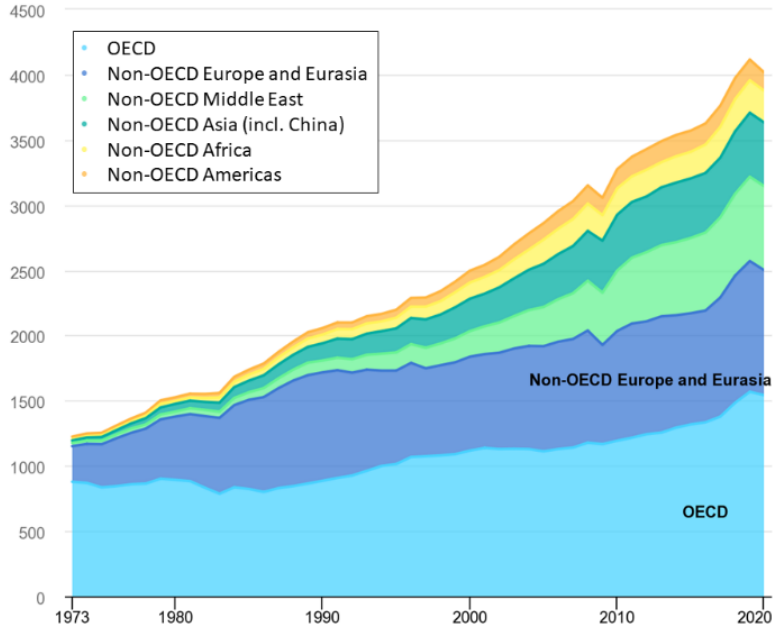

Figure 1.4 - World Natural Gas production by region, 1973-2020 [19]

The primary component of natural gas is methane, which has the greatest hydrogen/carbon ratio of all fuels and permits a lower CO_2 engine-out concentration (a decrease of more than 20% [21] and, thus, a smaller effect in terms of GHGs). If it is also noted that the development of this category of engines would entail the use of renewable methane, such as biogas, the positive impacts can be strongly enhanced. An additional factor to consider is the reduced PM emissions compared to conventional diesel engines [22]. At high compression ratio, a low flame speed and a lower temperature combustion allow the engine to emit less NO_x, and during lean air-fuel ratio (AFR) phases, the engine emits less CO than a conventional-fuel engine. However, the engine-out emissions of unburned methane are significantly higher, which is a disadvantage due to its high Global Warming Potential (GWP) and the difficulty in converting it due to the strong stability of the methane molecule, which has a tetrahedral structure with four equivalent C-H bonds and a strong connection between carbon and hydrogen [23].

1.2 Objective of the thesis

In this scenario, it is essential to matching the environmental targets keeping the costs of engine development affordable. Modelling of internal combustion engines is a multidisciplinary activity that is continuously growing and is more and more present during the development phase of an engine, mostly today when the time to production is reduced. For this reason, the creation of a *digital twin* of the real engine has acquired growing relevance, thanks to its lower financial burden, together with the need of an improved predictive capability. Among the other numerical approaches, the 1D models represent a proper compromise between reliability and

computational effort, especially if the engine behaviour has to be investigated over a number of operating conditions.

In the development process of an ICE, before the actual prototyping, a variety of computer simulation tools are used to estimate their performance with varying degrees of precision. Depending on the desired level of detail, these simulation tools may be based on three-dimensional (3D), one-dimensional (1D), or zero-dimensional (0D) models.

In view of the aforementioned concerns, the purpose of this research is to numerically analyse, using a hierarchical simulation-level method, heavy-duty spark-ignition engines with a focus on turbulence and combustion predictive sub-models. An ad hoc turbulence model, for HD engines, is developed and further validated during this PhD activity. To this aim two heavy-duty engines have been analysed, properly evaluating turbulence evolution and combustion process.

The first one is a stoichiometric SI heavy-duty engine fuelled with CNG, for commercial vehicle application. Two aspects make this engine an interesting case study: swirl-assisted in-cylinder flow motion, influencing the turbulence production, and the combustion of the gaseous fuel, slower than usual fossil-derived fuel.

The second one is an innovative single-cylinder heavy-duty engine fuelled with CNG, equipped with an active pre-chamber ignition system, which guarantees an ultra-lean operative (relative air/fuel ratio almost equal to 2), all over the engine operating plane. Pre-chamber ignition systems have gained a surge of interest in decreasing the fuel consumption and pollutant emissions [24], this is why research focuses heavily on this technology.

Turbulence is one of the most important aspects in Spark Ignition (SI) engines as it can significantly affect burn rates, heat transfer rates, combustion stability and thus performance. Turbulence originates from a large-scale motion that occurs during the induction process, which mainly consists of tumble motion in modern SI engines with a pentroof cylinder head. Despite its significance, most of the 0D turbulence models rely on calibration factors when calculating the evolution of tumble motion and its conversion into turbulence.

It is commonly recognized that tumble motion contributes to the improvement of flame front velocity in SI engines. When the piston is near TDC, the tumble motion is destroyed and converted in an increase in the Turbulent Kinetic Energy (TKE).

To preserve robustness and durability over the entire life cycle, most of CNG SI Heavy-Duty engines are derived from diesel engines, and properly converted to operate with stoichiometric combustion. The combustion chamber is commonly located in the piston crown and a flat cylinder head is used [16]. In the case of a flat

cylinder head with a bowl piston, tumble and swirl are both fundamental to the development of the turbulent motion field and the squish plays an important role, especially near the TDC, see Figure 1.5. By fragmenting these flows into small-scale turbulent eddies, *swirl*, *tumble*, and *squish* flows increase the intensity of turbulence during late compression. This accelerates the rate of combustion and enhances the speed of turbulent flames [18].

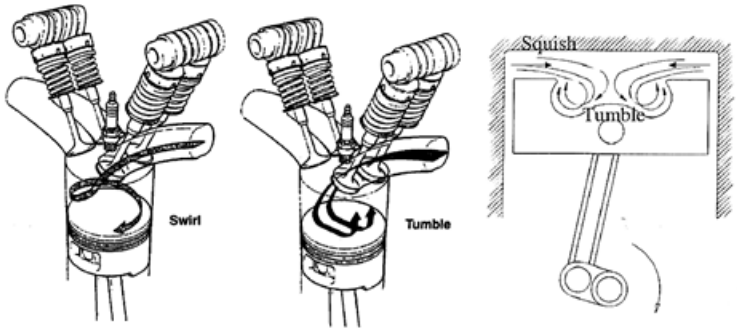

Figure 1.5 - Swirl, tumble and squish flows [17]

In this context, available turbulence models do not sufficiently describe all the ordered and unordered in-cylinder flow motion of a SI heavy-duty engine. Based on this context analysis, the research activity carried out within the PhD program is placed in an industrial context that foresees the use of ever faster and more reliable tools for the prediction of engine performances of the whole operating map, with the objective of developing the entire layout of future powertrains.

The focus of the research program aims at the turbulence model tailored for a SI diesel-derived heavy-duty engine fuelled with CNG, with a universal reliability for all SI engines. In addition, a fractal combustion model is coupled, with the turbulence one, in order to predict engine performances for all operating conditions.

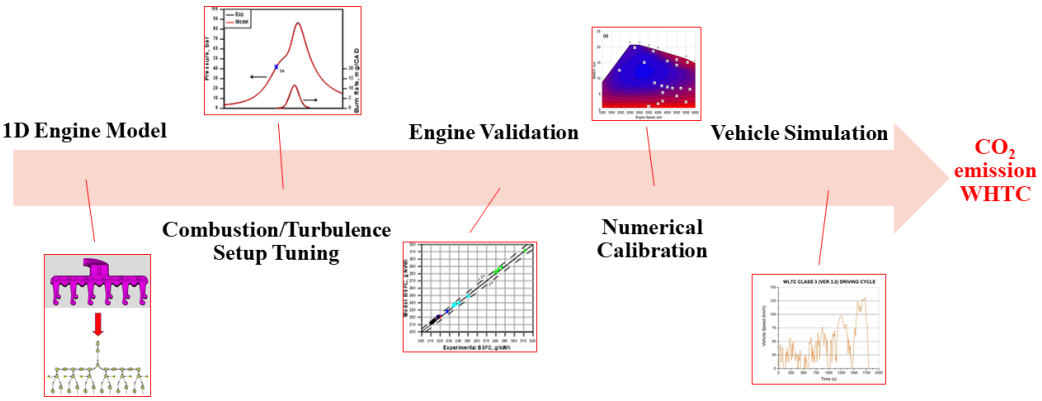

Figure 1.6 - Main modelling steps of the research activity

For the studied engines, the technique and key modelling processes depicted in Figure 1.6 were followed. Following a one-dimensional description of the flow inside the intake and exhaust pipes, the geometry of the tested engine is schematized in a commercial modelling framework. In order to recreate in-cylinder processes like as turbulence, combustion and heat transfer, phenomenological 0D submodels are utilized. Subsequently, in an effort to replicate the experimental calibration technique at the test bench, a rule-based calibration approach was also developed with the goal of identifying the ideal control parameter settings for the whole engine map. Then, after the engine maps were created, they could be included into a vehicle simulation to quantify the CO_2 emissions over a WHTC.

The thesis is divided as follows. Firstly, a brief introduction of the internal combustion engine will be provided, including the pertinent physical processes occurring within it: turbulence, combustion, and knock. The physical sub-models created to represent engine phenomena will be illustrated, with a focus on turbulence and combustion models. Then, simulation results analysing the tuning, validation, and numerical engine calibration techniques will be described. The main targets of the PhD program were totally fulfilled, regarding the application and improvement of turbulence and combustion models embedded for CNG heavy-duty engines. The models' improvement has been carried out by using a dedicated commercial software, GT-Suite by Gamma Technologies. Finally, pre-chamber engine technology, aiming to improve the heavy-duty ICE thermal efficiency, is presented and the simulation development and results will be reported and discussed.

Reference

1. Steffen, W., Broadgate, W., Deutsch, L., Gaffney, O., et al. “The Trajectory of the Anthropocene: The Great Acceleration”, The Anthropocene Review, 1-18, 2015, doi: 10.1177/2053019614564785.
2. Salman, M., Long, X., Wang, G., & Zha, D. (2022). Paris climate agreement and global environmental efficiency: new evidence from fuzzy regression discontinuity design. Energy Policy, 168, 113128.
3. European Environment Agency (EEA), "Annual European Union greenhouse gas inventory 1990-2020 and inventory report 2022", 2022. https://www.eea.europa.eu//publications/annual-european-union-greenhouse-gas-1.
4. Air quality in Europe – 2020 report, 2020, European Environment Agency, ISBN 978-92-9480-292-7
5. https://eur-lex.europa.eu/legal-content/EN/TXT/?uri=uriserv:OJ.L_.2014.103.01.0015.01.ENG
6. https://eur-lex.europa.eu/legal-content/EN/TXT/?uri=celex%3A32014R0253
7. https://www.europarl.europa.eu/thinktank/en/document/EPRS_BRI(2018)614689
8. https://eur-lex.europa.eu/legal-content/EN/TXT/?uri=COM:2018:284:FIN
9. https://ec.europa.eu/commission/presscorner/detail/en/ip_22_6495
10. https://mobilitynotes.com/summary-of-euro-7-vii-proposal-criteria-pollutants/
11. Nemeth, K. and Carvalho, J.M., “Dieselgate and Consumer Law: Repercussions of the Volkswagen scandal in the European Union” Journal of European Consumer and Market Law, 6 (1), pp.35-35,2017, ISSN: 2364-4710.
12. Sperling, D., “Future drive: Electric vehicles and sustainable transportation,” Island Press, 2013, ISBN: 9781559633277.
13. European Commission, Directorate-General for Internal Market, Industry, Entrepreneurship and SMEs, Ntziachristos, L., Papadopoulos, G., Samos, Z., et al., Euro 7 impact assessment study, Publications Office of the European Union, 2022, https://data.europa.eu/doi/10.2873/249061
14. Thiruvengadam, A., Besch, M., Padmanaban, V., Pradhan, S., & Demirgok, B. (2018). Natural gas vehicles in heavy-duty transportation-A review. Energy Policy, 122, 253–259. https://doi.org/10.1016/j.enpol.2018.07.052
15. Baratta, M., & Misul, D. (2015). Development of a method for the estimation of the behavior of a CNG engine over the NEDC cycle and its application to quantify for the effect of hydrogen addition to methane operations. Fuel, 140, 237–249. https://doi.org/10.1016/j.fuel.2014.09.088
16. Johansson, B. and Olsson, K., “Combustion Chambers for Natural Gas SI Engines Part I: Fluid Flow and Combustion,” SAE Tech. Pap. 950469, 1995, doi:10.4271/950469.

17. Kaplan, M. (2019). Influence of swirl, tumble and squish flows on combustion characteristics and emissions in internal combustion engine-review. International Journal of Automotive Engineering and Technologies, 8(2), 83-102.
18. Heywood, J., B., "Internal combustion engine fundamentals," Vol. 930, New York, Mcgraw-Hill, 1988, ISBN: 007028637X.
19. "Statics report: Natural Gas Information – Overview", International Energy Agency, Paris, 2020, https://www.iea.org/reports/natural-gas-information-overview.
20. International Energy Outlook 2016, U.S. Energy Information Administration, DOE/EIA-0484, 2016.
21. Kato T., Saeki K., Nishide H., Yamada T., "Development of CNG fueled engine with lean burn for small size commercial van". JSAE Rev 2001; 22:365-8
22. Cho, H. M., He, B. Q., "Spark ignition natural gas engines – A review", Energy Conversion and Management, 48(2): 608-618, 2007, doi:10.1016/j.enconman.2006.05.023.
23. National Center for Biotechnology Information (2020). PubChem Compound Summary for CID 297, Methane. Retrieved December 1, 2020 from pubchem.ncbi.nlm.nih.gov/compound/Methane.
24. Zhu, S., Akehurst, S., Lewis, A., & Yuan, H. (2022). A review of the pre-chamber ignition system applied on future low-carbon spark ignition engines. Renewable and Sustainable Energy Reviews, 154, 111872.

2 Overview of SI Internal Combustion Engine

An internal combustion engine has the aim to produce mechanical power from the chemical energy contained in the fuel, which is burned or oxidized inside the engine itself. Nowadays, SI and Compression Ignition (CI) engines are widely used in the transport and power generation sectors due to their simplicity, ruggedness and high power/weight ratio. Since this thesis is focused on SI engine for automotive application, only this kind of system will be briefly recalled in this chapter. In particular, the SI ICEs for heavy commercial applications are characterized by a four-stroke working cycle in which each cylinder requires four strokes of its piston, two revolutions of the crankshaft, to realize the thermodynamic cycle [1].

Currently most of the OEM's are manufacturing GDI engines due to its advantages over PFI engines. The limitation of the SI engine is that a higher compression ratio cannot be achieved due to knocking tendency, but this problem, in SI engine fuelled with CNG, is not so intense as conventional gasoline engine because of methane high Octane Number [2].

The four stroke cycle in an SI engine can be seen in Figure 2.1, where the piston and valve movement during the intake (a), compression (b), expansion (c=, exhaust (d) stroke are shown [1].

a. *Intake stroke*: during the intake stroke, the air and fuel are inducted into the engine through the open intake valves as the piston moves towards its lower position, bottom dead center (BDC).
b. *Compression stroke*: in the compression stroke both intake and exhaust valves are closed and the charge is compressed as the piston moves towards its upper position, top dead center (TDC).
c. *Expansion stroke*: close to TDC the air/fuel mixture is ignited, differently depending on the combustion principle. The combustion process usually occurs in the last part of the compression stroke and continues some time into the expansion stroke. During the expansion stroke the gases, burned or unburned, are expanded and work is produced.
d. *Exhaust stroke*: during the exhaust stroke, the exhaust valves are open and the piston pushes the burned gases out from the cylinder. The four stroke described are repeated continuously as long as the engine is running.

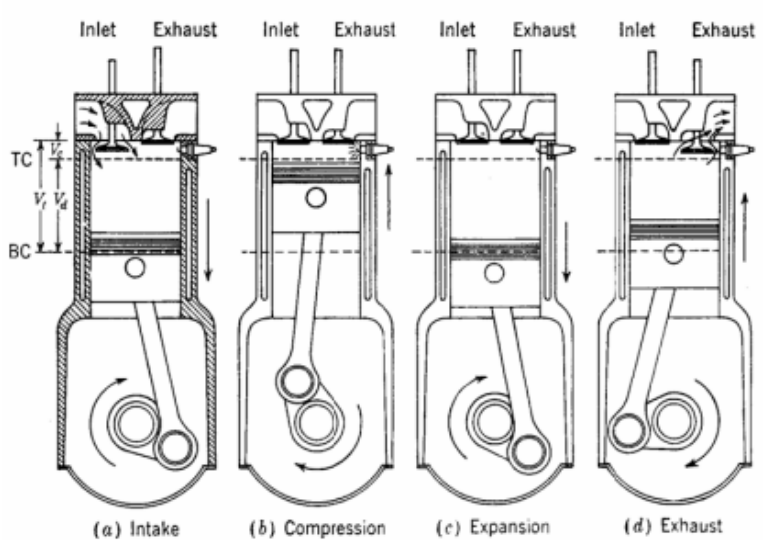

Figure 2.1 - The four stroke principle for a SI engine [1]

Each phase contributes significantly to the total power and efficiency of the cycle. During the intake phase, the necessary quantity of air/fuel mixture must be fed into the cylinder in order to achieve the specified load level with the correct mixture quality for combustion. The geometry of the intake pipes, the throttle valve, and the turbocharging system govern the air flow, while the fuel can be injected in either a Port Fuel Injection (PFI) or a Direct Injection fashion (DI). In the former, gasoline is injected into the intake port via a low-pressure system, whereas in the later, fuel is provided directly into the cylinder at a greater pressure. Injection at a high pressure is essential to achieve fuel penetration, diffusion, and vaporization. DI systems offer for improved fuel economy, with the danger of higher Particle Matter (PM) in the event of fuel wall impingement compared to PFI systems [3].

The intake ports must also ensure appropriate gas flow within the cylinder, since this affects the combustion process, heat transmission, and air/fuel mixture. By varying the direction of the intake ports, the geometry of the valves, and the form of the combustion chamber, three distinct gas movements may be generated: the tumble, the swirl, and the squish. This motion is produced into combustion chambers to boost the combustion rate and/or to guarantee proper charge mixing. As soon as the electric discharge across the spark plug occurs, a set amount of time before TDC, combustion commences. The flame kernel develops in a laminar way then turbulence makes flame front grow which spreads across the combustion chamber, and dies upon contact with the walls [1]. The length of the combustion process within a cylinder is normally between 40 and 60 CAD. As soon as the expansion phase concludes, the exhaust phase begins, allowing for the cylinder scavenging process and the admission of the following cycle's fresh charge.

2.1 Turbulent combustion

The flame propagation is one of the main factors which influences the combustion in the Spark Ignition engines. In PFI SI engines, the fuel and air are mixed inside the port and the combustion process can be imagined in two stages, growth and development of the flame and flame propagation throughout the cylinder.

The flame propagation inside the cylinder is affected by the following parameters.

- Fuel-air ratio – the velocity of the flame depends on the quality of the charge. If the mixture is lean or rich, the velocity of flame reduces compared to the stoichiometric mixture.
- Compression ratio – the combustion process is accelerated more with the increase in compression ratio because of an increase in the temperature.
- Intake air temperature and pressure – an increase in the intake temperature and pressure increase the flame speed
- Turbulence – the turbulent motion of the mixture helps in better mixing fuel and air.
- Engine speed – the turbulent flame speed increases almost linearly with the engine speed, due to the increasing of in-cylinder turbulence motion.

The flame is formed by the electric discharge in the spark plug, whereas the flow field is generated during the intake process and adjusted during the compression stroke. Using digital imaging, the 2D flame development of an optically accessible single-cylinder PFI engine is shown in Figure 2.2 [4]. Various selected crank angles are presented in order to characterize the primary phases of the combustion process. After the spark ignition, which occurs at 3 CAD BTDC, the first flame with a roughly round shape is seen at 2 CAD ATDC. *Early flame development* describes this phase in which the flame propagates primarily under laminar conditions.

Then, about 6 CAD ATDC, the turbulent flow interaction creates wrinkles and corrugates the flame front, resulting in an uneven flame form. This increases the rate of combustion, initiating the *turbulent flame propagation* phase. When the flame approaches the cylinder walls, between 15 and 16 ATDC, combustion ceases and the *flame termination phase* begins.

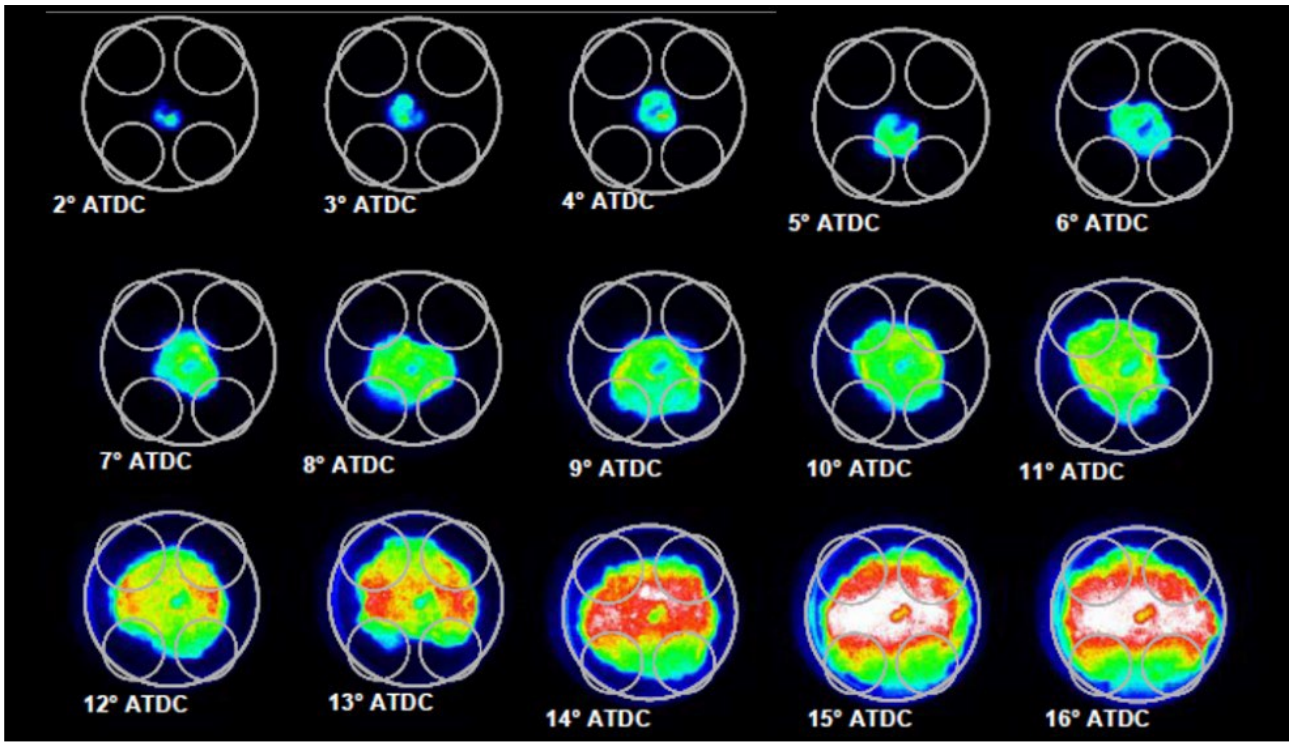

Figure 2.2 - UV-visible digital images of the flame propagation in gasoline SI engine [4], SA=3 CAD

The laminar flame speed, the turbulent field within the cylinder, and the SA setting all play crucial roles in the combustion process. This value depends on engine design, operating conditions, air/fuel ratio, etc. Typically, for a common SI engine, SA is adjusted so that 50% of the mixture is burned at 7-8 CAD ATDC (50% Mass Fraction Burned, MFB50) [1].

A flame kernel is generated between the spark plug electrodes following the ignition event. As indicated earlier, a smooth quasi-laminar flame of low thickness δ_L emerges initially, exhibiting laminar flame speed (S_L). It is the velocity of unburned gases entering a flat flame front in laminar flow regimes. In general, S_L is measured experimentally in a spherical sealed container by propagating a laminar flame radially outward from the center of the container at a regulated pressure and temperature [5]. Literature has several correlations derived from the collected data, the majority of which are based on the so-called *power law* formula [6, 7]:

$$S_L(\phi, T_u, p) = S_{L0}\left(\frac{T_u}{T_0}\right)^{\alpha}\left(\frac{p}{p_0}\right)^{\beta} \tag{2.1}$$

where S_{L0} is the flame velocity measured at a reference state, T_0, p_0, with a variable equivalence ratio ϕ. α and β mixture strength-dependent exponents which consider the pressure and temperature dependency.

The turbulence phenomenon is a 3D unsteady, rotational and highly diffusive flow, characterized by the presence of disordered eddies, ranging over a wide length scale

interval. The largest eddies are limited in size by the system boundaries, whereas the smallest ones are restricted by the molecular diffusion. The interaction among the eddies of various scales is responsible of a transfer of energy sequentially from the larger eddies gradually to the smaller ones, through a process known as the turbulent energy cascade. Due to the irregularity of a turbulent flow, this phenomenon is often characterized through statistical methods [1].

For an ICE in particular, an ensemble-averaging technique is utilized, in which the principal quantities are assessed at a fixed crank-angle θ over a large number of successive engine cycles. In this method, however, the turbulent quantities comprise cyclic fluctuations as well. The most often studied components are the mean velocity components ($\bar{u}$, $\bar{v}$, $\bar{w}$) and turbulent velocity components (u', v', w'), which are connected by the following expressions:

$$u(\theta) = \bar{u}(\theta) + u'(\theta);\ v(\theta) = \bar{v}(\theta) + v'(\theta);\ w(\theta) = \bar{w}(\theta) + w'(\theta) \tag{2.2}$$

Typically, the rough premise of a homogeneous and isotropic turbulent flow is presented to define the turbulent field inside the cylinder with relative ease. In this instance, two primary length scales can be distinguished, each coupled with a distinct time scale:

1. *Integral length scale* (L_t): reflects the greatest scale structure of the flow field, which is characterized by low frequency and significant fluctuations. It is defined as the integral of the autocorrelation coefficient of the variable velocity at two adjacent places in the flow in proportion to their separation.
2. *Kolmogorov length scale* (L_k): the lowest scale of turbulent motion, turbulent kinetic energy dissipates into heat.

Various combustion regimes are determined by the interaction of the flame and the turbulent flow environment. Each regime is connected with a distinct development and form of the flame. The comparison of previously determined characteristic lengths/velocities and timings is one of the most used methods for classifying the flame/turbulence interaction (Table 2.1).

Table 2.1 - Characteristic speed, length and time scales of the turbulent combustion

Scale	**Speed**	**Length**	**Time**
Chemical	S_L	δ_L	$\tau_L = \delta_L / S_L$
Kolmogorov	u_k	L_k	$\tau_k = L_k / u_k$
Integral	u'	L_t	$\tau_t = L_t / u'$

The Borghi diagram (Figure 2.3) may be used to show this comparison and identify all of the potential combustion regimes that might occur in a turbulent flame with premixed fuel [8].

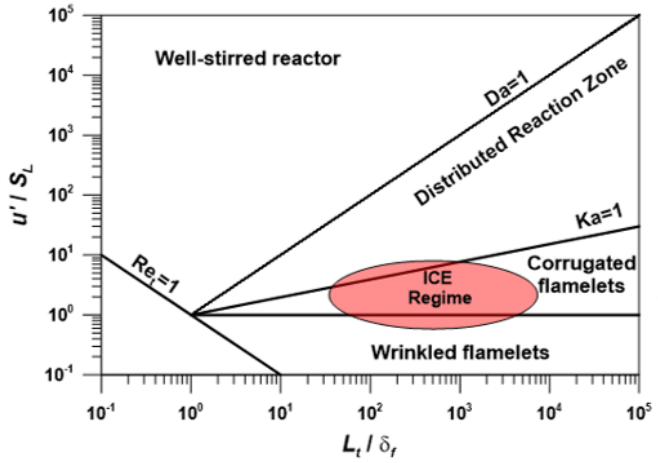

Regime	Re	Da	Ka	U'/SL	Flame
Wrinkled flamelets	>1	>1	<1	<1	
Corrugated flamelets	>1	>1	<1	>1	
Distribuited reaction zone	>1	>1	>1	>1	
Well-stirred reactor	>1	>1	>1	>1	
Broken reaction zone	>1	<1	>1	>1	

Figure 2.3 - Borghi diagram and list of turbulent premixed combustion regimes.

To do this, three dimensionless numbers must be introduced:

1. *Turbulent Reynolds number* (*Re*): explains the ratio of inertial to viscous forces. It primarily specifies the flow of motion inside the system. A turbulent flow has a Re number that is greater than the unit.

$$Re = \frac{u' L_t}{\nu}; \rightarrow \frac{u'}{S_L} = Re \left(\frac{L_t}{\delta_L}\right)^{-1} \tag{2.3}$$

2. *Damköhler number* (*Da*): relationship between turbulent and chemical time scales. With *Da* less than 1, turbulence is far quicker than chemistry, and combustion is governed mostly by chemical kinetics processes. In contrast, combustion, with a *Da* greater than the unit, is characterized by a highly rapid combustion reaction in relation to the turbulent phenomena.

$$Da = \frac{\tau_t}{\tau_L} = \left(\frac{L_t}{u'}\right) \Big/ \left(\frac{\delta_L}{S_L}\right); \rightarrow \frac{u'}{S_L} = Da^{-1} \frac{L_t}{\delta_L} \tag{2.4}$$

3. Karlovitz number (Ka): is the ratio of the chemical time scale to the Kolmogorov time scale. If *Ka* is less than 1, the flame thickness is less than the Kolmogorov scale; hence, chemical reactions within the flame front are not influenced by turbulent fields. When *Ka* gets greater than the unit, turbulent eddies enter the flame's reactive zone.

$$Ka = \frac{\tau_L}{\tau_k} = \left(\frac{L_t}{\delta_L}\right)^{-\frac{1}{2}} \Big/ \left(\frac{u'}{S_L}\right)^{\frac{3}{2}} = \left(\frac{\delta_L}{L_k}\right)^2 ; \rightarrow \frac{u'}{S_L} = Ka^{2/3}\left(\frac{L_t}{\delta_L}\right)^{2/3} \quad (2.5)$$

The aforementioned values are shown logarithmically in the Borghi diagram, where Re=1, Da=1, and Ka=1 indicate the limits of five distinct combustion regimes. These are depicted visually in Figure 2.3left and enumerated together with their corresponding flame morphology in Figure 2.3right. In *wrinkled flamelets*, the turbulence intensity is less than the laminar flame speed; hence, the turbulence lacks sufficient energy to corrugate the flame front. In addition, because *Ka* is less than the unit, chemical kinetics are insensitive to the presence of turbulence. The tiniest eddies cannot enter the flame front because they are larger than the thickness of the flame. As soon as the turbulence intensity surpasses the laminar velocity, the combustion regime enters the zone of *corrugated flamelets*. Here, the turbulence corrugates the flame front and may also form burned gas pockets within the zone of new gases. The *Ka* is still less than one, hence the turbulence has no effect on the flame structure. In the zone of *Distributed reactions*, *Ka* becomes more than 1, and the tiniest eddies penetrate the pre-heat zone of the flame, but not the reaction zone, since the thickness of the reaction zone is still greater than the largest eddies. The turbulent convection within the flame front enhances both heat transmission and mass transfer. Only when *Da* reaches a value lower than the unit, *well-stirred reaction zone,* the chemical kinetics govern the combustion. Indeed, the turbulence is so severe that it creates a perfect mixing of the reactants and combustion products, preventing the formation of a flame front. The last regime is the broken reaction zone ($Ka >> 100$), which is not visible on the Borghi diagram. In this regime, turbulent eddies reach the reaction zone, and hence there is no flame. Experimentation revealed that ICE operates primarily in the zone depicted by the red circle in Figure 2.3, where the chemical reaction may be readily represented by the laminar flame characteristics. This is one of the most prevalent ideas around which the bulk of combustion models are founded.

2.2 Knock phenomena

The knock phenomenon is one of the most dangerous forms of anomalous combustion that can occur in a SI ICE. It is a very complex phenomena, however, a simply description is repeated in the following.

Autoignition of the end-gas is noticed as a noise that is conveyed through the engine construction. It causes a quick heat release, which stimulates the propagation of pressure waves throughout the combustion chamber. This undesired occurrence must be prevented for several reasons. Initially, thermal losses rise because pressure fluctuations encourage heat transfer, hence limiting available work. Secondly, the

pressure wave reflections might destroy the lubrication coating around the cylinder, causing the engine to seize.

Lastly, when the severity of the knock is relatively high, irreparable damage might be caused to the cylinder, as seen in Figure 2.4.

In fact, excessive knock transfers heat to the combustion walls, causing the cylinder head and piston to overheat. The increased cylinder temperature increases the frequency of the knock, resulting in a progressively heavier phenomenon. Without correct control, this might quickly result in engine failure.

Figure 2.4 - Damaged piston examples from heavy engine knock [9].

The pressure waves induced by the presence of the knock generate a not uniform pressure distribution, consequently different pressure values can be recorded if the transducer is moved within the cylinder. In the literature, many approaches for the measurement and characterisation of the knock intensity are being offered [10]. Analysis of in-cylinder pressure signals using a pressure transducer flush-mounted in the combustion chamber is the method most commonly used. The acquired pressure trace is subsequently processed using a band-pass filter in the frequency range of 4-20 kHz. The low cut-off is utilized to filter out the normal combustion noise (low frequencies), while the high cut-off is necessary to eliminate the signal disruption caused by sensor resonances.

In order to measure the magnitude of the phenomena, it is necessary to develop a knock index: Integral of Modulus of Pressure Oscillations (IMPO) and Maximum Amplitude of Pressure Oscillations (MAPO) are the most prevalently employed ones [11]. In general, both are checked for each cycle within a defined crank angle window, which is normally 40-60 CAD from the spark occurrence. The indices are then averaged across a number of successive cycles (at least 100). MAPO and IMPO are monitored to prevent knocking by adjusting the timing of the spark. Indeed, retarding the time of the spark reduces the knock intensity, whereas an advanced spark increases the likelihood of knocking. Consequently, the SA is determined by

the engine speed at which the MAPO/IMPO index meets a predetermined goal threshold. It is important to note that aberrant combustion is the factor that restricts the compression ratio of SI ICE the most.

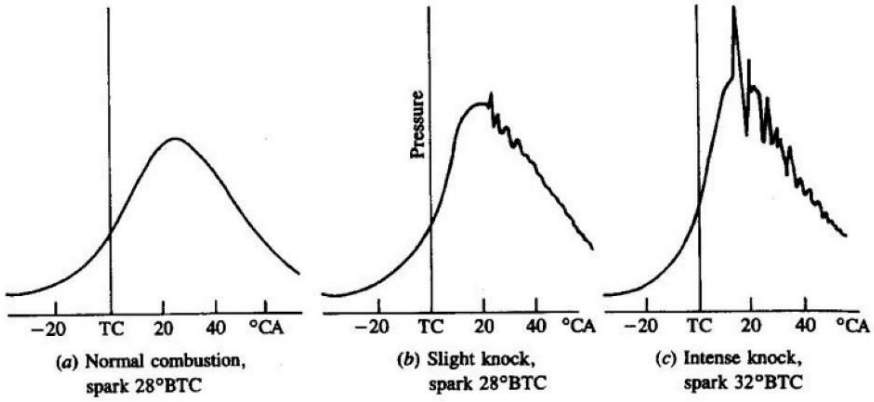

Figure 2.5 - Knocking effect at different spark timings [1]

Figure 2.5 shows the knocking effect against different spark timing. In the long run, knock effects are not desirable as it ruins the piston and reduces the engine life.

2.3 Cycle to Cycle variation

By adjusting the engine's control variables, such as Spark Advance (SA), valve timing, throttle position, and air-to-fuel ratio, it is possible to manage the combustion process and maintain the needed load for a certain engine architecture. As is well known, even when the control variables stay constant, two successive cycles are never identical. In fact, fluctuations in local flow motion in the turbulence levels inside the cylinder, in the mixture homogeneity and composition, particularly near the spark plug, lead to a phenomenon known as Cycle to Cycle Variation (CCV).

This behaviour should likewise be restricted in ICE. Indeed, the CCV is primarily responsible for changes in the rate of heat release, and therefore in the amount of useful work performed by a single combustion event, altering the stability of the braking torque, which has a direct effect on the vehicle's drivability. In contrast to the knock, the CCV cannot be totally eliminated but can only be restricted owing to its inherent nature. It has been established experimentally that the early phase of flame production is the most crucial combustion phase for the CCV. A combustion that begins slowly, such as when there is an excess of air or a significant proportion of residual gas, is more likely to exhibit cycle fluctuations.

In general, the intensity of the CCV is determined by the acquisition and post-processing of 300 to 500 consecutive pressure traces, analyzing the Coefficient of Variation (CoV) of a parameter associated with in-cylinder pressure, the combustion process, or engine performance. CoVs related with the Indicated Mean Effective Pressure (IMEP) and the in-cylinder peak pressure are the most widely used. The former is typically used to define the engine's drivability, and its value should be less

than 2 to 3 percent. While the latter has a more direct effect on the onset of knock, its CoV is often greater than that of the IMEP.

Due to the CoV phenomenon, given a fixed operating state, a train of pressure cycles will be observable, of which the average, fastest, and slowest cycles are often taken into account for engine control. Typically, the ideal spark time is determined by referencing the average cycle. Concerning close-to-knock circumstances, the severe cycles must be watched with particular care, since they restrict engine function. In fact, the quickest cycles restrict the compression ratio and determine the fuel octane required due to the likelihood of knocking being the highest. On the contrary, the slowest cycles impose the lean operating limit since they have the largest probability of incomplete combustion.

2.4 Ultra-lean combustion

Moreover, in recent years, automakers have shifted toward new SI engine topologies with unusual combustion principles in an effort to get major improvements throughout the engine plane. In fact, with the advent of the CO_2 emission restrictions in vehicle homologation, it is required to design a high-efficiency engine under the majority of its working circumstances. The most effective strategies for SI engine are to operate with lean mixture and high compression ratio. Indeed, engines intended for lean combustion can utilize greater compression ratios, resulting in superior performance, efficient fuel consumption, and lower engine-out hydrocarbon emissions than standard gasoline engines.

In place of classic stoichiometric engines, natural gas engines adopting lean burn combustion technology have been adopted, which has two good advantages: first, extra air in the mixture lowers the temperature of the combustion process, hence reducing the generation of NO_x compared to typical stoichiometric engines. The combustion process is more efficient and more energy is produced from the same amount of fuel when there is an excess of oxygen [12]. However, SI-ICEs based on flame propagation can only operate with a slight amount of extra air, limiting the true value of this combustion paradigm. In fact, lean mixtures decrease the laminar flame speed, resulting in unacceptable cyclic variability, misfire, and massive HC-CO production [1, 13].

Different strategies have been explored in the present literature in an effort to extend these limits. One of these is the Homogeneous Charge Compression Ignition (HCCI) [14], that is a form of combustion in which fuel and air are good premixed and compressed to the point of auto-ignition, combining characteristics of conventional gasoline and diesel engines. This kind of technology demonstrated problematic ignition timing control, restricted power output and poor cold-start performances.

Spark-Assisted Compression Ignition (SACI) is a modified version of HCCI [15]. SACI is a combustion strategy that employs a spark plug to ignite a deflagration flame that creates enough ignition energy to cause autoignition in the remaining charge.

Another solution that permits to easily implement an ultra-lean combustion is the pre-chamber (PC) ignition system, where a modest volume containing the spark-plug is linked to the Main-Chamber (MC) by means of small orifices. Such system is already in use in low-speed large-bore gas engine, but non yet in road applications.

The primary challenges that must be addressed by all of these engine architectures relate to the accurate control of the combustion development and emission formation.

In this PhD thesis, more attention will be spent for the PC mechanism and more details will be presented in the next section.

2.4.1 Pre-chamber engine

In the 1910s, the pre-chamber combustion system was reported for the first time on a Ricardo Dolphin engine that utilized a passive auxiliary intake valve to manage the flow of fuel-rich mixture into the pre-chamber cavity [16]. In certain configurations, an extra fuel injector was proposed to provide fuel to the pre-chamber, and the Honda compound vortex-controlled combustion system might be the most effective example [17, 18, 19]. By eliminating the supplementary pre-chamber fuelling, a number of alternative engine ideas were offered, including torch cell engines developed by Toyota [20], Ford [21], and Volkswagen [22]. These early research projects were mostly on large-volume pre-chamber combustion devices. The increased thickness of the pre-chamber wall increases heat transfer losses and hydrocarbon (HC) emissions.

The jet ignition is a subset of the pre-chamber combustion system, which Nikolai Semenov created in the late 1950s and Lev Ivanovich Gussak refined [23, 24]. The pre-chamber capacity in this design is just 2–3% of the clearing volume, and the single throat linking the pre-chamber to the main chamber is replaced with a nozzle with many orifices.

The combustion initiated by the TJI technology differs significantly from the standard SI combustion. The mixture in the pre-chamber is ignited with a spark plug, and the pressure increase caused by the flame propagation propels the hot products and active radicals into the main chamber via the jet orifices. The turbulent jets' high turbulence intensity and various ignition spots encourage combustion in the main chamber. Thus, the TJI is an excellent method for speeding combustion, enhancing combustion stability, and increasing the SI engine's lean combustion limit.

Emissions created in the cylinder depend heavily on the production of air-fuel mixes, ignition, and combustion processes. Increased hydrocarbons (HC), carbon monoxide

(CO), and particulate matter (PM) are a result of the short period for fuel evaporation and mixing in direct-injected gasoline engines. In a real-world application of TJI, the pre-chamber configuration, the extra fuel injection, the lambda level, and the engine loads also play significant roles in determining raw emissions. However, the lean-burn TJI system's extra air and lower combustion temperatures ensure low NO_x emissions, while HC an CO are strongly affected by the combustion calibration of the lean mixture.

The Table 2.2 compares the SI and CI systems with the TJI system based on their combustion characteristics. According to the comparison characteristics, the TJI engine is more fuel efficient and emits less pollutants than the standard SI engine. With an additional fuel injection system, the TJI engine can equal the performance of the CI engine.

Table 2.2 - Comparison of different combustion concepts in internal combustion engines [25-28]

	SI	CI	HCCI	TJI
Ignition	Spark ignition, single point	Auto ignition, single point	Auto ignition, multi-points	Spark Ignition, multi-points
Fuel Injection	Gasoline like fuels, port or direct injection	Diesel like fuels, direct injection	Flexible fuels, port or early direct injection	Flexible fuels in the pre-chamber if applicable
Air-fuel ratio	~1	1.2-2-2	2-8, depending on the fuel	Stoichiometric or lean
Flame	Turbulent flame propagation	Diffusion flame propagation	Homogeneous oxidation	Turbulent flame propagation
Major emissions	HC, CO and NO_X	NO_X and PM	HC and CO	Subject to design
Fuel economy	Good	Better	Best	Better

The pre-chamber ignition systems are categorized into two types (Figure 2.6): passive and active pre-chamber. During the compression stroke, the passive pre-chamber is filled with homogenous fuel-air combinations from the main chamber. To precisely manage the equivalence ratio of the stratified mixture, the active pre-chamber system is coupled with an auxiliary fuel-metering device. Thus, the passive and active pre-chamber systems are also known as the homogeneous and stratified pre-chamber systems, respectively.

Similar to a traditional SI engine, a spark plug ignites the mixture in the pre-chamber, followed by conventional premixed flame propagation. Since the flame dynamics in the main chamber differ from those of a standard SI engine, the timing of the spark must be modified to compensate the difference.

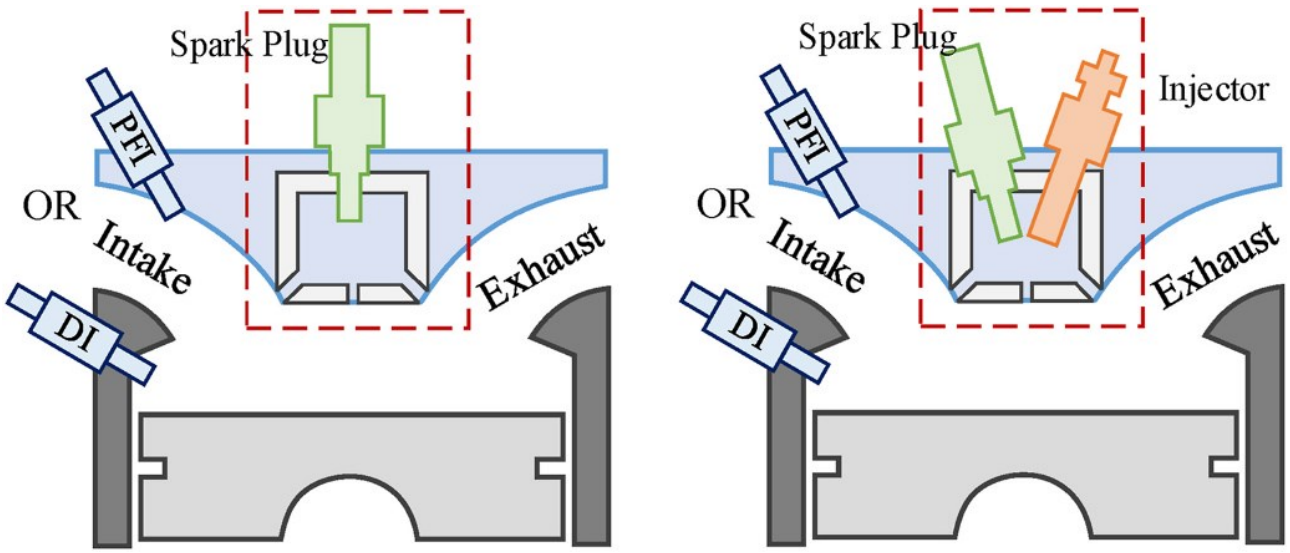

Figure 2.6 - Configurations of passive (left) and active (right) pre-chamber ignition systems [25Figure 2.6]

Following the pre-chamber combustion, the pressure differential caused by the pre-chamber combustion forces the flame and partly oxidized species into the main chamber. According to changes in temperature and the mass percentage of the intermediate reaction products, the jet ejection from the pre-chamber into the main chamber may generally be separated into three phases. Due to the spatial arrangement of the spark electrodes, the unburned mixture exits the pre-chamber during the initial cold jet phase. In the second phase, the intermediate reaction products are ejected from the pre-chamber and ignite the mixture in the main chamber. The third phase is distinguished by a markedly lowered temperature of the ejected mixture and low mass fractions of the intermediate reaction products. This signifies that the dense portion of the mixture in the pre-chamber will ultimately be expelled.

In addition, pressure traces and high-speed images, obtained with an experimental campaign by using an optical-access engine, may provide further information regarding the jet ejection process. In Figure 2.7 is shown that the first visible jets appear 9 Crank Angle Degrees (CAD) before the top dead center (TDC). Further examination of the optical pictures reveals that reactive and bright jets develop in the main chamber but soon dissipate as a result of a sharp reduction in pressure and temperature in the main chamber and the entrainment of new charge. High-temperature turbulent jets carrying chemically reactive radicals (O, H, and OH) ignite the mixture in the main chamber by chemical, thermal and turbulent processes, which dominate the main chamber's whole combustion process. A high jet velocity results in a greater distance of penetration, and more air-fuel mixture might be pushed into the main chamber, also known as the turbulence effect. The pre-chamber ignition system with numerous ignition sources might increase the ignition energy by more than two orders of magnitude compared to the ordinary spark plug [30].

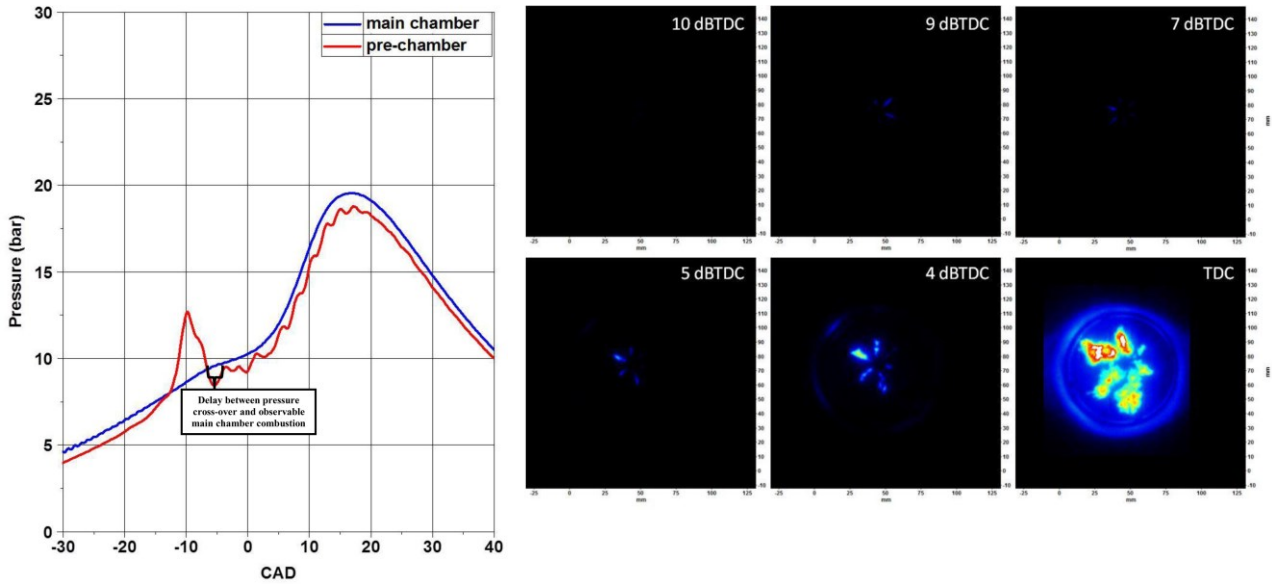

Figure 2.7 - Pressure traces (left) and visualizations (right) during jet ejection processes on an optical engine [29]

Further examination of the combustion process in the main chamber reveals that it begins in many spots within the hot jets. After the whole entrained matter within the hot jets has swiftly burnt, the flame reaches the jet borders and then advances as a well-established flame front outside the jets. Consequently, the turbulence effect is primarily responsible for the flame propagation within the main chamber.

Reference

1. Heywood, J. (1988). Internal Combustion Engine Fundamentals. New York, US: McGraw-Hill Education.
2. Mokhatab, S., Poe, W. A., & Mak, J. Y. (2015). Handbook of Natural Gas Transmission and Processing: Principles and Practices. Amsterdam, Holland: Elsevier Science.
3. Chen, L., Liang, Z., Zhang, X. and Shuai, S., "Characterizing particulate matter emissions from GDI and PFI vehicles under transient and cold start conditions," Fuel, 189, pp.131-140, 2017, doi:1016/j.fuel.2016.10.055.
4. Bozza, F., Gimelli, A., Merola, S.S., Vaglieco, B.M., "Validation of a fractal combustion model through flame imaging," SAE transactions, pp.973-987, 2005., doi:https://www.jstor.org/stable/44722057.
5. Metghalchi, M., Keck, J., "Laminar burning velocity of propane-air mixtures at high temperature and pressure," Combustion and flame, 38, pp.143-154, 1980, doi:10.1016/0010-2180(80)90046-2.
6. Amirante, R., Distaso, E., Tamburrano, P., Reitz, R. D, "Laminar flame speed correlations for methane, ethane, propane and their mixtures, and natural gas and gasoline for spark-ignition engine simulations," International Journal of Engine Research, 18(9), 951-970, 2017, doi: 10.1177/146808747720018
7. Amirante, R., E. Distaso, P. Tamburrano, R. D. Reitz. "Analytical correlations for modeling the laminar flame speed of natural gas surrogate mixtures," Energy Procedia 126 (2017): 850-857, doi: 10.1016/j.egypro.2017.08.289.
8. Peters, N., "Laminar flamelet concepts in turbulent combustion", Symposium (International) on Combustion 21(1): 1231-1250, 1988, doi:10.1016/S0082-0784(88)80355-2.
9. d'Adamo A. Numerical modelling of abnormal combustion in high-performance spark-ignition engines PhD Thesis. Italy: University of Modena and Reggio Emilia; 2015. http://dx.doi.org/10.13140/RG.2.1.1159.2405.
10. Millo, F., Ferraro, C., "Knock in S.I. Engines: A Comparison between Different Techniques for Detection and Control," SAE Technical Paper 982477, 1998, doi:10.4271/982477.
11. Brecq G., Bellettre J., Tazerout M., "A New Indicator for Knock Detection in Gas SI Engines," International Journal of Thermal Sciences, 42, pp.523-532, doi:10.1016/S1290-0729(02)00052-2.
12. Perin, M. and Achek, T., "Lean Burn Engines," SAE Technical Paper 2013-36-0402, 2013, https://doi.org/10.4271/2013-36-0402.
13. Rapp, V., Killingsworth, N., Therkelsen, P., et al., "Lean Combustion, 2nd Edition," Lean-Burn Internal Combustion Engines, Elsevier, 2016, 111-146, doi:10.1016/C2013-0-13446-0.

14. Stanglmaier, R., Roberts, C., “Homogeneous charge compression ignition (HCCI): benefits, compromises, and future engine applications,” SAE transactions, pp.2138-2145,1999, doi: www.jstor.org/stable/44741335.
15. Okita, R., “Mazda SKYACTIV-G Engine with New Boosting Technology,” In Advanced Clean Cars Symposium: The Road Ahead, Air Resources Board, Sacramento, USA, 27th–28th September,2016
16. Turkish MC. 3-valve stratified charge engines: evolvement, analysis and progression. SAE Trans 1974:3483–503.
17. Dale J, Oppenheim A. Enhanced ignition for IC engines with premixed gases. SAE Trans 810146 1981:606–21.
18. Oppenheim AK. Prospects for combustion in piston engines. SAE Trans 2002: 1707–21.
19. Yagi S, Dath T, Ukawa H, Fujii I. Research and development of honda cvcc engine. Paper C13/75 presented at IMechE Conference1976.
20. Noguchi M, Sanda S, Nakamura N. Development of Toyota lean burn engine. 1976. p. 2358–73. SAE Transactions.
21. Adams TG. Torch ignition for combustion control of lean mixtures. 1979. SAE Technical Paper 790440.
22. Brandstetter W. The volkswagen lean burn pc-engine concept. 1980. p. 1804–21. SAE Transactions.
23. Stadler A, Sauerland H, H¨artl M, Wachtmeister G. The potential of gasoline fueled pre-chamber ignition combined with elevated compression ratio. 2020. SAE Technical Paper 2020-01-0279.
24. Gussak L, Karpov V, Tikhonov YV. The application of lag-process in prechamber engines. SAE Trans 1979:2355–80.
25. Zhu, S., Akehurst, S., Lewis, A., & Yuan, H. (2022). A review of the pre-chamber ignition system applied on future low-carbon spark ignition engines. Renewable and Sustainable Energy Reviews, 154, 111872.
26. Telli GD, Altafini CR, Costa CA, Rosa JS, Martins ME, Oliveira Rocha LA. A comprehensive review of homogeneous charge compression ignition (HCCI) engines: Advantages, challenges and evolution. SAE Technical Paper 2020-36-0042. 2021.
27. Agarwal AK, Singh AP, Maurya RK. Evolution, challenges and path forward for low temperature combustion engines. Prog Energy Combust Sci 2017;61:1–56.
28. Bendu H, Murugan S. Homogeneous charge compression ignition (HCCI) combustion: mixture preparation and control strategies in diesel engines. Renew Sustain Energy Rev 2014;38:732–46.

29. Bunce M, Blaxill H, Kulatilaka W, Jiang N. The effects of turbulent jet characteristics on engine performance using a pre-chamber combustor. 2014. SAE Technical Paper 2014-01-1195.
30. Distaso E, Amirante R, Cassone E, De Palma P, Sementa P, Tamburrano P, et al. Analysis of the combustion process in a lean-burning turbulent jet ignition engine fueled with methane. Energy Convers Manag 2020;223:113257.

3 Methodologies for Internal Combustion Engine Modelling

The development of a new engine is a very complex process and the experimental activity has to comply with the all the phenomena discussed in the previous chapters, resulting in increasing cost and duration of engine development. As a result, numerical analysis are crucial owing to its cheaper costs, which contributes to the reduction of engine development time [1]. The modelling of ICE is a multidisciplinary subject involving several areas, and it may be categorized into four primary groups based on the approximation level employed, as shown in Table 3.1.

Table 3.1 - Classification of the numerical approaches.

Model type	Typical application
0D	Combustion
1D	Gas Exchange
Quasi-dimensional	Combustion
3D	Flow field, Combustion

Zero-dimensional (0D) methods solve the mass and energy conservation equations on the premise that thermodynamic parameters are a function of time alone. Any spatial dependence is therefore disregarded, and it is believed that the working fluid is at rest. This method's capacity to mimic in-cylinder operations in less computing time is its primary benefit. The typical disadvantage is the absence of pressure wave propagation in the pipes, which severely limits the ability to forecast volumetric efficiency.

Due to the fact that they calculate the unsteady flow equations in the exterior pipes in the mean flow direction, 1D models are able to circumvent the aforementioned limitation. In this method, all thermo-fluid-dynamic properties are deemed uniform along each pipe segment. To effectively forecast the overall engine behavior, 1D models are typically paired with a precise 0D description of in-cylinder processes (quasi-dimensional phenomenological submodels). Due to the favorable balance between precision and processing time, they are increasingly utilized to analyze worldwide engine performance and, more recently, to enable engine optimization and calibration [2].

On the basis of the integration of the Navier Stokes equations, 3D techniques provide extensive fluid-dynamic data for the complicated 3D domains. Due to their significant computing effort, these models are utilized to simulate the unsteady mean and turbulent flow motion inside a small area of the engine, often the intake air-box, after-treatment devices, and cylinder, under a limited set of operating circumstances.

In the present research, the selected technique is based on a 1D description of the flow within the intake and exhaust pipes, whereas phenomenological 0D sub-models

are employed to simulate in-cylinder processes. However, 3D techniques will also be used, with a particular emphasis on their function in assisting the creation and validation of a 0D turbulence sub-model.

3.1 0D approaches

As stated before, with a 0D method, all variables are unambiguously time-dependent and uniform over the whole control region. As a result, just the mass and energy conservation equations, Eq. (3.1), (3.2) must be solved, as shown below:

$$\frac{dm}{dt} = \dot{m}_{in} - \dot{m}_{out} + \dot{m}_{inj} \tag{3.1}$$

$$\frac{d(me)}{dt} = -p\frac{dV}{dt} - \frac{dQ_w}{dt} + \dot{m}_{in}h_{in} - \dot{m}_{out}h_{out} + \dot{m}_{inj}h_f^0 \tag{3.2}$$

The first two components of equation (3.1) represent the incoming and outgoing mass flow rates through the valves, while the last term relates to the fuel injection flow rate. In equation (3.2), the first term represents the mechanical power transferred by the fluid to the piston, the second term represents the heat transfer rate through the walls of the combustion chamber, and the last three terms represent the enthalpy fluxes associated with the mass exchanges through the control surface. Typically, eq. (3.2) is rewritten as a function of the temperature variation eq. (3.3), taking into account the dependence of the internal energy on temperature and composition. This formulation expresses the energy released by the combustion process as a function of the variation in the burnt gas percentage, from reactants to products, $\frac{dx_b}{dt}$.

$$\frac{dT}{dt} = \frac{1}{mc_v}\left(-p\frac{dV}{dt} - \frac{dQ_w}{dt} + \dot{m}_{in}h_{in} - \dot{m}_{out}h_{out} + \dot{m}_{inj}h_f^0 - e\frac{dm}{dt} - \frac{\partial e}{\partial x_b}\frac{dx_b}{dt}\right) \tag{3.3}$$

Several sub-models are employed to solve these equations in order to account for the lack of velocity field data. Numerous correlations exist in the current literature for the gas-cylinder wall heat transfer, which are mostly based on the in-cylinder thermodynamic state and engine speed.

For ICE modelling, the Woschni [3], Hohenberg [4], and Annand [5] correlations are extensively used. This thesis employs a Hohenberg-like correlation, which will be discussed in the next section. The instantaneous flow through the valves is determined using the isentropic flux equation in subsonic, eq. (3.4), or sonic, eq. (3.5), circumstances.

$$\frac{dm}{dt} = c_d A_{ref} p_1 \sqrt{\frac{2k}{k-1}\frac{1}{RT_1}\left[\left(\frac{p_2}{p_1}\right)^{\frac{2}{k}} - \left(\frac{p_2}{p_1}\right)^{\frac{k+1}{k}}\right]}$$

(3.4)

$$\frac{dm}{dt} = c_d A_{ref} p_1 \sqrt{\frac{k}{RT_1}\left[\left(\frac{2}{k+1}\right)^{\frac{k+1}{k-1}}\right]}$$

(3.5)

p_1 and T_1 represent the pressure and temperature of the upstream flow, whereas p_2 is the downstream pressure. k is the ratio of heat capacity, and A_{ref} is the reference area. The discharge coefficient, c_d, is the ratio of the actual flow to the isentropic flow, and it is determined empirically under steady-state circumstances. In general, this value is determined by the geometry, lift, and flow direction (direct / reverse) of the valve.

The burning rate (dx_b/dt) may be directly imposed, or it may be predicted using predictive combustion models. Typically, the former strategy is utilized during the first phase of model development. If available, the "*experimental*" burning rate can be imposed by extracting it from the experimental pressure traces using so-called reverse analysis to solve equations (3.1) and (3.3). Otherwise, a Wiebe function assuming a pre-set burnt fraction profile as a function of crank angle is utilized [6].

As a result of the number of thermodynamic zones into which the control volume is subdivided, a zero-dimensional model may be further subclassified into three distinct types. Specifically, it is feasible to employ a single, two, or multiple-zone strategy. At each time step, the equations (3.1) and (3.3) are solved for each zone's unique thermodynamic state involving energy and mass interactions. During the intake and exhaust phases, it is acceptable to assume that the cylinder's composition is consistent across its whole. As a result, a single zone is utilized. As soon as the spark happens, however, the combustion chamber is primarily separated into two zones, the unburned and the burnt zones (two-zone approach).

Multi-zone models are also commonly utilized when it is necessary to estimate pollutant emissions such as NO_x, since the presence of a temperature gradient in the unburned zone has a significant impact on the accuracy of their prediction.

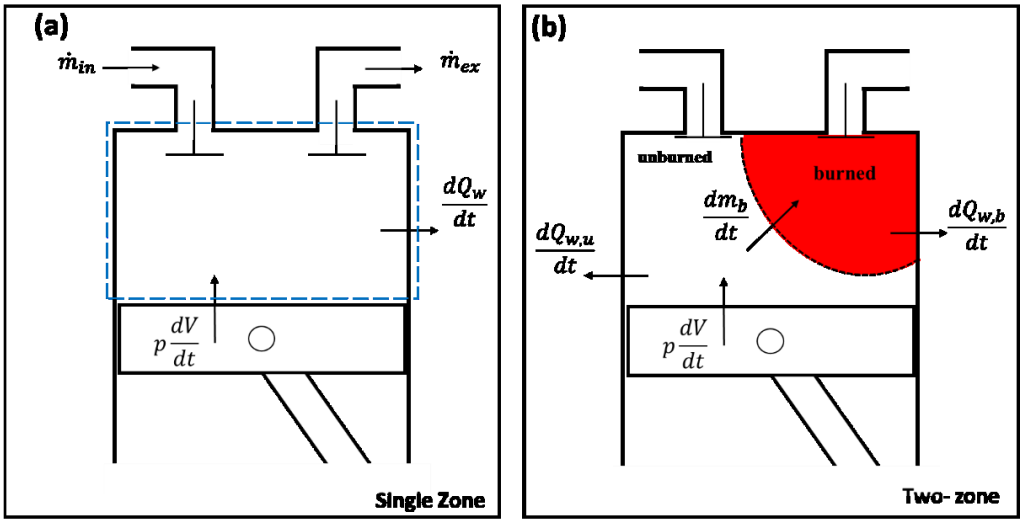

Figure 3.1 - Single zone combustion scheme (a) and two-zones combustion scheme (b)

Since many years, several combustion models for SI engines have been suggested, attempting to physically analyse the burning rate under the assumption that turbulence enhances combustion [7, 8, 9]. The transition from laminar to turbulent flame and the process that induces the turbulence-related increase in burn rate are the fundamental distinctions between these two types. Other techniques, such as the one presented in [10], where the combustion chamber is characterized as a stochastic reactor and the combustion is modelled using probability density functions, are also utilized. Certainly, the eddy burn-up technique and the fractal model are the most extensively utilized combustion models. The former explains the flame entrainment and subsequent combustion of the unburned mixture, and was shown to be consistent with the experimental burnt mass fraction trends [11, 12]. Using the notions of fractal geometry, the latter paper attempts to explicitly explain the improvement of flame front surface [13, 14]. Several comparisons of both techniques are available in the literature, leading to the conclusion that, with the exception of tuning efforts, both models are capable of accurately simulating the combustion within standard SI engines [7, 15]. Due to a more solid physical background, the fractal technique was chosen for this dissertation, proving that it can be applied, if appropriately developed, to both conventional SI and pre-chamber engines.

3.2 1D approaches

The partial differential equation system in (3.6) gives the conservative version of the flow equations (continuity, energy, and momentum) assuming an inviscid, adiabatic 1D flow schematization in a variable area pipe. Each thermodynamic attribute and the flow velocity, u, are merely a function of location, x, and time, t, in this model:

$$\begin{cases} \dfrac{\partial \rho}{\partial t} + \dfrac{\partial \rho u}{\partial x} + \rho u \left(\dfrac{1}{\Omega}\dfrac{d\Omega}{dx}\right) = \dfrac{\partial \rho}{\partial t} + \dfrac{\partial \rho u}{\partial x} + \rho u \alpha_A = 0 \\ \dfrac{\partial (\rho E)}{\partial t} + \dfrac{\partial (\rho u H)}{\partial x} + \rho u H \left(\dfrac{1}{\Omega}\dfrac{d\Omega}{dx}\right) = \dfrac{\partial (\rho E)}{\partial t} + \dfrac{\partial (\rho u H)}{\partial x} + \rho u H \alpha_A = 0 \\ \dfrac{\partial (\rho u)}{\partial t} + \dfrac{\partial (\rho u^2 + p)}{\partial x} + \rho u^2 \left(\dfrac{1}{\Omega}\dfrac{d\Omega}{dx}\right) = \dfrac{\partial (\rho u)}{\partial t} + \dfrac{\partial (\rho u^2 + p)}{\partial x} + \rho u^2 \alpha_A = 0 \end{cases}$$

(3.6)

The aforementioned equations can also be stated in a more compact vector form (3.7), where *U* represents the vector of conservative variables, *F* represents the flow vector and *S* represents the source term vector.

$$\frac{\partial U}{\partial t} + \frac{\partial F(U)}{\partial x} = S \quad U = \begin{Bmatrix} \rho \\ \rho u \\ \rho E \end{Bmatrix}; \quad F = \begin{Bmatrix} \rho u \\ \rho u^2 + p \\ \rho u H \end{Bmatrix} \quad S = -\begin{Bmatrix} \rho u \alpha_A \\ \rho u^2 \alpha_A \\ \rho u H \alpha_A \end{Bmatrix}$$

(3.7)

To accurately represent the flow within the intake and exhaust pipes of an ICE, additional variables must be taken into account, including gas-wall friction, heat exchange, and the scalar transport of injected fuel and residuals species. The system then acquires the shape shown in (3.8), where the final two rows correspond, respectively, to the propagation of residual gases and vapour fuel percentage.

$$U = \begin{Bmatrix} \rho \\ \rho u \\ \rho E \\ \rho x_r \\ \rho x_f \end{Bmatrix}; \quad F = \begin{Bmatrix} \rho u \\ \rho u^2 + p \\ \rho u H \\ \rho u x_r \\ \rho u x_f \end{Bmatrix}; \quad S = -\begin{Bmatrix} \rho u \alpha_A \\ \rho u^2 \left(\alpha_A + \dfrac{2 f_a}{D}\dfrac{u}{|u|}\right) \\ \left(\rho u H \alpha_A - \dfrac{4q}{D}\right) \\ \rho u x_r \alpha_A \\ \rho u x_f \alpha_A \end{Bmatrix}$$

(3.8)

where f_a is the friction coefficient determined using the Poiseuille or Blasius formula as a function of the pipe velocity.

x_r and x_f represent, as stated, the residual gas fraction and vapor fuel fraction, respectively, and are calculated according to the equation (3.9).

$$x_r = \frac{m_r}{m}; \quad x_f = \frac{m_f}{m}$$

(3.9)

q denotes the heat flow through the pipe walls, which is given by the following equation:

$$q = \frac{1}{2}\rho|u|f_a c_p(T_{wall} - T)$$

(3.10)

3.3 3D approaches

Based on the resolution of the mass, momentum, and energy equations as a function of time along the three spatial coordinates, 3D models solve the Navier-Stokes equations. These equations constitute a nonlinear system of partial differential equations that are suitably schematized on a computational grid and solved in the control volume. Due to the system's complexity, it is generally addressed using Computational Fluid Dynamics (CFD) software via three alternative methods:

1. *Direct Numerical Simulation* (*DNS*): direct discretization of the Navier-Stokes equations. However, the computational cost is significant in terms of both time and storage. In fact, for an accurate solution, the computing grid must be so tiny that it can capture all temporal and spatial turbulence scales, even the tiniest (Kolmogorov scale). These are principally used for engine simulations only for CFD numerical analysis.
2. *Reynolds Averaged Navier-Stokes* (*RANS*) *equations*: decomposition of the turbulent field into its time-averaged and fluctuating quantities. The RANS equations are obtained by averaging the original flow equations across time. Therefore, RANS represent the time-averaged behavior, or phase-averaged flow realizations in the case of quasi-periodic flows such as those in internal combustion engines. The time-averaging adds additional terms, known as "Reynolds stresses," whose solution requires the construction of suitable turbulence submodels in order to solve the problem.
3. *Large Eddy Simulation* (*LES*): the larger eddies, which are substantially impacted by the domain's shape, are solved directly. To save computing time, only the smallest scales are accurately modelled. Today are also used for in-cylinder combustion description.

It is important to note that the high degree of accuracy achieved by 0D-1D models, such as the one utilized in this PhD Thesis, is a result of the integration of all the previously discussed methodologies. In the modern automobile industry, it is normal practice to utilise both 0D-1D and 3D simulations to aid in the engine development phase. Indeed, this strategy permits overcoming limitations and combining the benefits of each discipline. On the one hand, 3D models allow for realistic studies of the engine's fluid-dynamic behaviour, but the research is limited to a small number of scenarios due to the high processing costs. In general, the purpose of 3D research is to get knowledge that cannot be easily obtained by experimental campaigns, hence facilitating a better understanding of physical processes. On the other hand, 0D/1D models may explore the whole engine system in less time and with great precision.

However, if the in-cylinder process formulation is poor, the findings cannot be deemed practical.

As an illustration, the next section describes briefly how 0D/1D/3D techniques were merged during this study endeavour. Four steps were taken in particular to describe the engine with the conventional spark plug system:

1. From the engine's geometric characteristics, a 0D/1D model was constructed. At various engine speeds, preliminary 1D simulations of motored processes were done.
2. As a boundary condition for the 3D in-cylinder motored studies focusing on the characterisation of the in-cylinder flow motion, the time-varying pressure and temperature calculated in 1D were enforced. Throughout the whole engine cycle, the mean and turbulent flow fields were extracted in detail.
3. The data from step 2 were used to calibrate the 0D turbulence model, which was required for the combustion model closure, which will be detailed in further depth in the following section.
4. After the turbulence model was calibrated, the 1D engine model was run under firing circumstances. The combustion model was primarily tuned against experimental data in an effort to match in-cylinder pressure cycles.

When a new engine, far from the current state of the art, is being studied, it may be necessary to design new in-cylinder models or, if feasible, to strengthen the ones already in use.

3.4 Turbulent combustion modelling for conventional SI engine

The turbulent combustion model is the main topic of this PhD thesis. The objective was to improve with respect to the state of the art the prediction of the heat release rate, the in-cylinder pressure profile and, consequently, the engine performances. The investigated phenomenological combustion models are based on a two-zone, burnt and unburned, description of the combustion chamber. Both models are based on the concept that aerodynamic turbulence increases the burn rate relative to laminar propagation. In this section, the theory of two turbulent combustion model will be presented. In the next chapter a comparison between the two models will be shown.

3.4.1 Eddy burn-up combustion model (SITurb)

In research and industrial contexts, the commercial software GT-Suite is largely employed for numerical simulations. This software uses a version of eddy burn-up as turbulent combustion model, the so-called SITurb. Despite the fractal model, developed by University of Naples, is used during this research activity, a comparison between the two models has been considered mandatory.

The eddy burn-up model is based on original approach proposed by Keck [16, 17], whose conceptual scheme is reported in Figure 3.2. The eddy burn-up combustion model forecasts the burn rate for SI engines with homogenous charge. This model of combustion is based on a two-zone, entrainment and burn-up concept. This model's prediction takes into account the cylinder shape, spark location and timing, airflow, and fuel characteristics. These equations determine the mass entrainment rate into the flame front and the burn rate:

$$\frac{dm_e}{dt} = \rho_u A_L (U_T + S_L) \tag{3.11}$$

$$\frac{dm_b}{dt} = \frac{(m_e - m_b)}{\tau} \tag{3.12}$$

$$\tau = c_t \frac{\Lambda_T}{S_L} \tag{3.13}$$

$$U_T = c_s u' \left(1 - \frac{1}{1 + c_k \left(\frac{r_f}{L_t} \right)^2} \right) \tag{3.14}$$

where,

m_e = entrained mass of unburned mixture

t = time

ρ_u = unburned gas density

A_L = “smooth” flame front area

U_T = turbulent flame speed

S_L = laminar flame speed

m_b = burned mass

τ = time constant

Λ_T = Taylor microscale length

u' = turbulent intensity

r_f = flame radius

L_t = integral length scale of turbulence

c_t = Taylor length multiplier

c_s = turbulent speed multiplier

c_k = flame kernel growth multiplier

Following the scheme, the combustion phenomena is separated into two major mechanisms, the first of which is the entrainment of unburned mixture into the turbulent flame brush, whose thickness is proportional to the Taylor length scale λ [18] where the entrainment rate is defined by eq. (3.11). In a subsequent phase, according to eq. (3.12), the entrained but still unburned mass, (m_e-m_b), is oxidized in a characteristic time scale, τ (eq. (3.13)).

In the different variants of the eddy burn-up model [17, 19, 20], the transition from laminar to turbulent combustion is characterized by the introduction of the appropriate adjustments. Typically, these modifications are associated with the characteristic length and time scales of combustion and turbulence.

Morel [20] suggested the model in which the transition is governed by the ratio between the flame radius, r_f, and the integral length scale of turbulence, L_t (eq. (3.14)).

The Eddy burn-up model needs no particular treatment of combustion ending and flame-wall interaction. Eq. (3.12) represents an exponential burn rate decline, which reproduces automatically the normal burn fraction tail. Consequently, a more direct regulation of burn rate deceleration during wall-combustion is impossible.

Actually, experiments suggest a corrugated flame front, with occasionally unburned gas pockets that burn inwards. Consequently, rather than offering a physical description of the combustion process, equations (3.11)-(3.14) should be seen as a mathematical model of the S-shaped burn fraction profile.

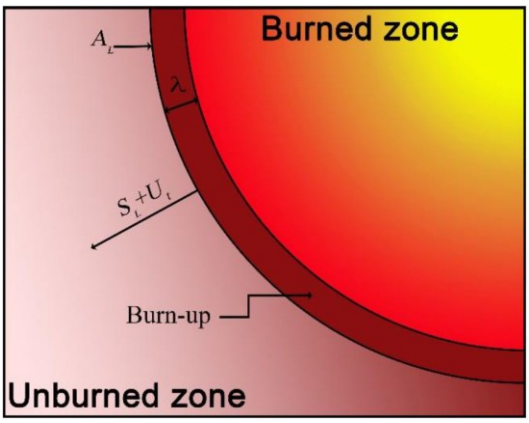

Figure 3.2 - Eddy burn-up combustion scheme

3.4.2 Fractal combustion Model

Several decades ago, the first form of the fractal combustion model was proposed [21]. This strategy is directly based on the combustion regime of a standard SI engine, which belongs to the zone of wrinkled-corrugated flamelets (Figure 2.3). As previously mentioned, the interaction between the turbulence and the flame front results in an increase in the combustion rate due to the flame front's increased surface, A_T. This geometrical increase is explained by the model using fractal geometry ideas. Multiple experimental investigations demonstrated that a wrinkled flame front exhibits fractal activity, resulting in the self-similarity of its fundamental structure [13, 22, 23, 24]. This makes possible to link the turbulent flame front extend to the laminar flame front one based on the characteristic speed, time, and length scales of turbulence [21, 25].

According to this concept, the burn rate may be expressed as a function of the *wrinkling factor*, which is the ratio of the turbulent to the laminar flame area A_T/A_L:

$$\left(\frac{dm_b}{dt}\right)_{fractal} = \rho_u A_T S_L = \rho_u A_L S_L \left(\frac{A_T}{A_L}\right) = \rho_u A_L S_L \left(\frac{L_{max}}{L_{min}}\right)^{D_3-2}$$

(3.15)

This wrinkling ratio is calculated based on the fractal dimension D_3, the maximum and minimum wrinkling scales L_{max} and L_{min}, and the classical expression given in [9]. D_3 is considered to be dependent on turbulence intensity, u', and laminar flame speed, S_L, as stated in [24], according to the following equation:

$$D_3 = \frac{2.35u' + 2.00S_L}{u' + S_L}$$

(3.16)

In addition, the wrinkling scales can be viewed as the macro and micro vortices of the turbulent flow field. L_{max} is proportional to a macroscopic dimension of the flame front, considered to be proportional to the flame radius r_f, via the tuning constant c_{wrk} (wrinkling multiplier).

$$L_{max} = c_{wrk} r_f$$

(3.17)

L_{min} is typically associated to the size of the smallest turbulent eddy [21], as measured by the Kolmogorov length scale, L_k.

$$L_{min} = L_k$$

(3.18)

The aforementioned concept, depicted schematically in Figure 3.3, is applicable to a fully formed and freely growing turbulent flame. Concerning early flame formation and combustion completion, the model must be modified appropriately.

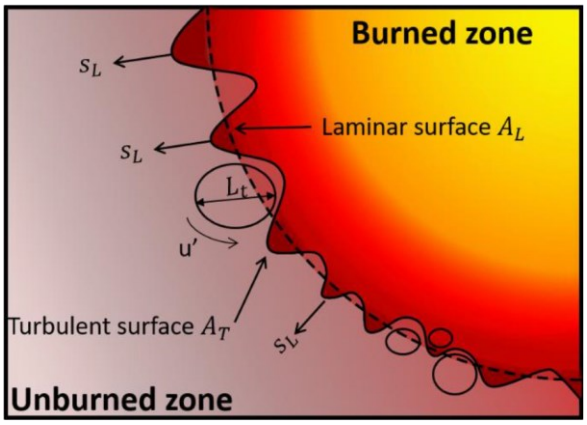

Figure 3.3 - Schematic of the fractal combustion model

As previously stated, the start of combustion is characterized by laminar propagation as opposed to turbulent propagation, in which the flame front is not completely corrugated. The transition from laminar to turbulent combustion is then characterized by an increase in fractal dimension D_3, according to equations (3.19) and (3.20)

$$D_3 = \frac{D_{3,max}u' + D_{3,min}S_L}{u' + S_L} \tag{3.19}$$

$$D_{3,min} = 2.00\,; \quad D_{3,min} = 2.00(1 - w_{trans}) + 2.35w_{trans} \tag{3.20}$$

The wrinkling development is governed by the variable w_{trans} in eq. (3.21), which is a function of a characteristic time scale, t_{trans}, and a model tuning constant, c_{trans} (transition multiplier). The characteristic time scale is determined using the kinetic energy of turbulence, k, and its dissipation rate, ε.

$$w_{trans} = \int \frac{dt}{c_{trans}t_{trans}}\,; \quad t_{trans} = \frac{k}{\varepsilon} \tag{3.21}$$

In contrast, when the flame front interacts with the walls of the combustion chamber, another change to the burning rate is introduced. Although a precise description of flame-wall interaction is much beyond the capabilities of a quasi-dimensional model, it can be claimed that flame front wrinkling no longer happens near the walls and that the burning rate decreases.

Therefore, the total burning rate is stated as a weighted average of a completely fractal burning rate and a laminar wall combustion, according to the equations (3.22) and (3.23).

$$\left(\frac{dm_b}{dt}\right) = (1 - w_{wall})\left(\frac{dm_b}{dt}\right)_{fractal} + w_{wall}\left(\frac{dm_b}{dt}\right)_{wall}$$

(3.22)

$$\left(\frac{dm_b}{dt}\right)_{wall} = \rho_u A_L S_L$$

(3.23)

w_{wall} characterizes the transition from turbulent to wall combustion by the ratio of the area wetted by the flame front on the piston, head, and cylinder, A_w, to the total area of the flame front, A_{tot}. This ratio is multiplied by the mass fraction of burnt gas, x_b, multiplied by an exponent multiplied by the tuning constant, x_{wc} (wall combustion multiplier).

$$w_{wall} = \frac{A_w}{A_{tot}} x_b^{10x_{wc}}$$

(3.24)

Under the conventional assumption of a smooth spherically shaped surface centered on the sparkplug, the A_L estimation is performed using a tabular method in order to save calculation time. The off-line automated approach computes the intersections between an "ideal" smoothed spherical flame front and the piston/head/cylinder surfaces. At each time step, the look-up table is read and the laminar flame area is calculated based on the current piston position and the burnt gas volume.

The laminar flame speed can be calculated by a numerical correlation. An examination of published publications demonstrates that different writers have in the past proposed a variety of laminar flame speed compositions for gasoline. These may be classified into two primary categories: experimentally-based, such as [26] and [27], and reaction kinetics-based, described in [28, 29]. On the one hand, the most significant drawback of the previous technique is the limited measuring range of relative air/fuel ratio and low pressure owing to technological concerns [28, 30]. As a result, these correlations may result in erroneous predictions when used beyond the measurement range, like for the typical high pressures and temperatures of SI engine operations. The kinetic-based technique, on the other hand, permits the investigation of a broader variety of boundary conditions using kinetic calculations; nevertheless, the reliability of these models is highly dependent on the specified kinetic scheme and surrogate fuel formulation. During this research activity, an experimentally-derived correlation, for a blend of methane, ethane and propane, is used [31, 32]. This

formulation was the most suitable choice to better reproduce the laminar flame speed that occurs in engines fuelled with CNG.

Since a specifically correlation referred to CNG blend is not available in the literature, the experimentally based correlation holding for a variable composition blend of methane, ethane and propane was considered the most reasonable approach.

The correlation is based on the so-called "*power law*" formula:

$$S_L(\phi, T_u, p) = S_{L0}\left(\frac{T_u}{T_0}\right)^{\alpha}\left(\frac{p}{p_0}\right)^{\beta}$$

(3.25)

where S_{L0} is the flame velocity measured at a reference state, T_0, p_0, with a variable equivalence ratio ϕ. α and β are mixture strength-dependent exponents, considered to be second-order polynomial functions of ϕ, whose expression are:

$$\alpha = \alpha_0 + \alpha_1\phi + \alpha_2\phi^2$$

(3.26)

$$\beta = \beta_0 + \beta_1\phi + \beta_2\phi^2$$

(3.27)

where the values of each parameter are listed in Table 3.2

The Dirrenberger correlation [32], eq. (3.28), is used for the estimation of S_{L0} and the related parameters are defined according to [31] and reported in Table 3.2. χ_1 and χ_2 are the volume concentrations of ethane and propane, respectively.

$$S_{L0}(\phi, \chi_1, \chi_2) = (1 + \upsilon_1\chi_1^{\tau_1})(1 + \upsilon_2\chi_2^{\tau_2})W\phi^{\eta(1-\chi_1)^{f_1}(1-\chi_2)^{f_2}}e^{-\xi(\phi-\sigma-\Omega_1\chi_1-\Omega_2\chi_2)^2}$$

(3.28)

Table 3.2 - Coefficients of the laminar flame speed correlation

T_0=298 K, p_0=1.01 bar T_{range}= [298-500 K]; p_{range}= [1-25 atm]; ϕ_{range}=[0.6-2.1]			
W	38.85	α_2	5.75
η	-0.20	β_0	-1.47
ξ	6.45	β_1	2.00
σ	1.08	β_2	-0.90
α_0	7.98	e_1	2.06
α_1	-12.15	e_2	0.77

Also the impact of the residual gas (Residual Exhaust Gas – X_{EGR}) is modelled, by using a correction term (eq. (3.29)), which multiplies the laminar flame speed given by eq. (3.25). This formulation [33] overcomes the flame speed zeroing which results from the widely adopted correction proposed in [34], at high X_{EGR}.

$$EGR_{factor} = (1 - e_1 X_{EGR}^{e_2})$$

(3.29)

where the correction coefficients e_1 and e_2 are listed in Table 3.2.

3.4.3 *K-k-T-S* Turbulence model

For the fractal combustion model completion, the method necessitates a number of factors associated with the turbulent field created within the combustion chamber, like u', L_k, L_t and ε.

The main topic of this research activity was to develop a turbulence model that properly suits with a heavy-duty SI engine. The in-cylinder turbulence is generated due to three main ordered flow motions, *tumble*, *squish* and *swirl*. Each of these contributes to the developing of the turbulence phenomenon. Regarding a diesel-derived SI heavy-duty engine, the swirl motion is predominant during the intake and compression phases and, for this reason, a proper model has been developed.

A phenomenological procedure, derived from the 3D RNG $k-\varepsilon$ turbulence formulation, synthesised using a 0D framework, leading to the scheme described below [35]:

$$\frac{dmK}{dt} = (\dot{m}K)_{inc} - (\dot{m}K)_{out} + mK\frac{\dot{\rho}}{\rho} - P - P_T - P_S + \dot{K}_{inj}$$

(3.30)

$$\frac{dmk}{dt} = (\dot{m}k)_{inc} - (\dot{m}k)_{out} + \frac{2}{3}\frac{\dot{\rho}}{\rho}\left(-mv_t\frac{\dot{\rho}}{\rho} + mk\right) + P + P_T + P_S - m\varepsilon$$

(3.31)

$$\frac{dmT}{dt} = (\dot{m}T)_{inc} - (\dot{m}T)_{out} - f_{dT}\frac{mT}{t_T}$$

(3.32)

$$\frac{dmS}{dt} = (\dot{m}S)_{inc} - (\dot{m}S)_{out} - f_{dS}\frac{mS}{t_S}$$

(3.33)

The equations shown above govern the evolution of the following flow quantities:

1. Mean kinetic energy $K = (1/2)U^2$, where U is the mean velocity inside the cylinder.
2. Turbulent kinetic energy $k = (3/2)u'^2$, where *u'* is the intensity of the turbulent field inside the cylinder, assumed to be homogeneous and isotropic.
3. Specific angular momentum of the tumble motion $T = U_T r_T$, where U_T is the tumble vortex velocity and r_T is the tumble radius. The kinetic energy K_T related to tumble momentum is $U_T^2/2$. Tumble speed is commonly expressed in a non-dimensional form as tumble number $N_T = U_T/(\omega_{eng} r_T)$, where ω_{eng} is the engine angular speed.
4. Specific angular momentum of the swirl motion $S = U_S r_S$, where U_S is the swirl vortex velocity and r_S is the swirl radius. The kinetic energy K_S related to swirl momentum is $U_S^2/2$. As well as tumble number, swirl number is defined as: $N_S = U_S/(\omega_{eng} r_S)$.

The term m is the in-cylinder mass, while $\dot{K}_{inj}$ is the kinetic energy associated with possible direct fuel injection.

3.4.3.1 Convective flows

The first and the second term in the above equations describe incoming and outcoming convective flows through the valves. The following equations are used:

$$(\dot{m}K)_{inc} = \frac{1}{2}\left[\dot{m}_{inf}\left(c_{Kin0} v_{Kinf}\right)^2 + \dot{m}_{exf} v_{Kexf}^2 + \dot{m}_{exb} v_{Kexb}^2\right] \tag{3.34}$$

$$(\dot{m}K)_{out} = K(\dot{m}_{inb} + \dot{m}_{exf}) \tag{3.35}$$

$$(\dot{m}k)_{inc} = 0 \tag{3.36}$$

$$(\dot{m}k)_{out} = k(\dot{m}_{inb} + \dot{m}_{exf}) \tag{3.37}$$

$$(\dot{m}T)_{inc} = r_T\left(\dot{m}_{inf} c_{Tin0} v_{Tinf} - \dot{m}_{exf} v_{Texf} - \dot{m}_{exb} v_{Texb}\right) \tag{3.38}$$

$$(\dot{m}T)_{out} = T(\dot{m}_{inb} + \dot{m}_{exf}) \tag{3.39}$$

$$(\dot{m}S)_{inc} = r_S(\dot{m}_{inf} c_{Sin} v_{Sinf} - \dot{m}_{exf} c_{Sex} v_{Sexf} - \dot{m}_{exb} v_{Sexb}) \tag{3.40}$$

$$(\dot{m}S)_{out} = S(\dot{m}_{inb} + \dot{m}_{exf})$$

(3.41)

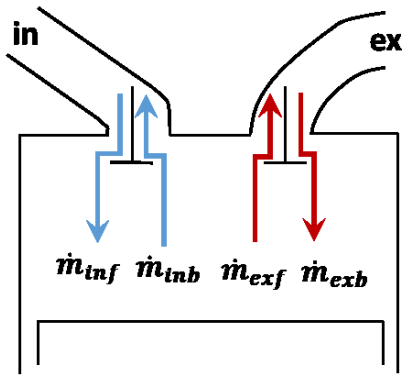

Figure 3.4 - Schematic of valve flows

In the Equations above $\dot{m}_{in}$ and $\dot{m}_{ex}$ indicate the mass flow passing through the intake and exhaust valves, respectively. The subscripts *f* and *b* indicate the directions of the flow through the valves, that can be forward or backward (Figure 3.4). Instantaneous mass flows are calculated through a simple nozzle-like model, accounting for the pressure difference across the valve and the effective flow area, related to the instantaneous flow coefficient and valve lift.

In equations (3.34), (3.38) and (3.40), the velocities v_K, v_T and v_S include the flow losses through the valves. More precisely, they comprise the discharge, the tumble, and the swirl coefficients, respectively. These coefficients are automatically specified as a function of the valve lift. Even if the model does not explicitly describe the actual shape of intake runners, the influence of intake port design on ordered and unordered motions is considered in the above coefficients. The possibility to tune the discharge, tumble, and swirl momentum is offered by the global multipliers c_{Kin0}, c_{Tin0}, c_{Sin}, and c_{Sex}. The last two terms of equations (3.38) and (3.40) give a subtractive contribution to the tumble and swirl intensities, assuming that the exhaust flow, both in forward and backward direction, produces a reverse tumble and swirl, opposite to the ones produced by intake flows.

3.4.3.2 Decay functions

In the equations (3.32) and (3.33), the terms $f_{dT}\frac{mT}{t_T}$ and $f_{dS}\frac{mS}{t_S}$ express the decay of the two main ordered motions due to the shear stresses with the combustion chamber walls. A decay function f_d is used for the tumble and another one for the swirl, considering a characteristic time scale t_T for the tumble and t_S for the swirl.

$$f_{dT} = c_{fd0,T} + c_{fdm,T}\left[\max\left(\frac{B}{H}, 1\right) - 1\right]$$

(3.42)

$$t_T = \frac{r_T}{u'}$$

(3.43)

$$f_{dS} = c_{fd0,S} + c_{fdm,S} \left| \frac{U_{sq}}{U_S} \right|$$

(3.44)

$$t_S = \frac{r_S}{u'}$$

(3.45)

Both decay functions for tumble and swirl are dependent on a fixed term and a time-varying term. The former is active during the whole engine cycle and expresses the dissipation of ordered flow structures caused by internal viscous forces, while the latter takes into account the dissipation effects caused by the piston rising (Figure 3.5 andFigure 3.6). Specifically, the second term of tumble decay indicates its collapse caused by the piston rising, and it is inversely proportional to the piston position, H, normalized by the cylinder bore, B (Figure 3.5). This component is supposed to be proportional to the ratio of the squish velocity, U_{sq}, to the swirl velocity, U_S. To adjust the two contributions to tumble and swirl decays, equations (3.42) and (3.44) present two parameters, $c_{fd0,x}$ and $c_{fdm,x}$. Equations (3.43) and (3.45) show that the characteristic time scales, t_T, and t_S, of tumble and swirl are assumed to inversely depend on the turbulence intensity and directly on the related radii. The radii of tumble and swirl are calculated based on geometrical data of the cylinder and piston according to equations (3.46) and (3.47).

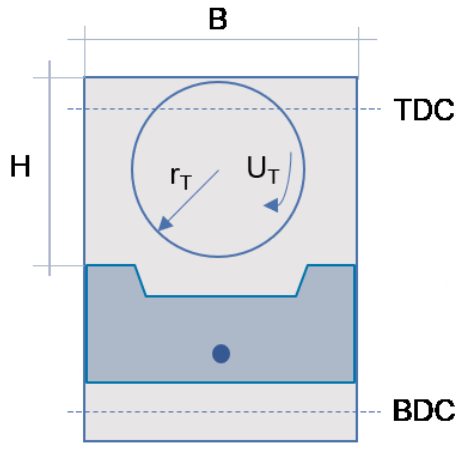

Figure 3.5 - Qualitative sketch of the tumble vortex

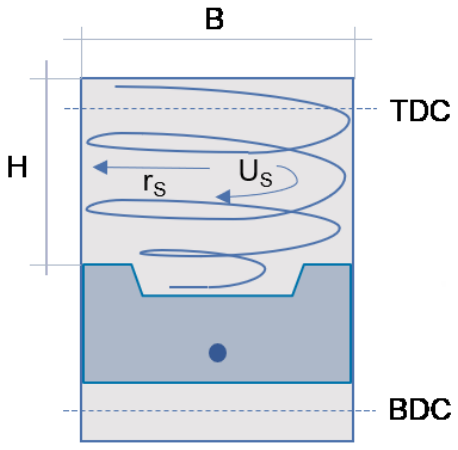

Figure 3.6 - Qualitative sketch of the swirl vortex

$$r_{T,S} = c_{r0T,S} + c_{rmT,S} \frac{1}{4} \sqrt{B_\vartheta^2 + (H + s_{bowl})^2}$$

(3.46)

$$B_\vartheta = \frac{(V_{cyl} - V_{bowl}) \cdot B + V_{bowl} \cdot d_{bowl}}{V_{cyl}}$$

(3.47)

In equation (3.46), B_θ and (H+s_{bowl}) are instantaneous representative dimensions along radial and axial directions around which ordered motions arise, whereas c_{r0T} and c_{rmT} (or c_{r0S} and c_{rmS}) are two parameters that allow the tumble (or swirl) radius to be adjusted. d_{bowl} and s_{bowl} are the diameter and the height of the piston bowl, respectively (Figure 3.7). B_θ is a time-variant parameter (eq. (3.47)), it is equal to the bore B if the piston is at BDC, while it is equal to the bowl diameter if, ideally, there is no space between the top of the piston and the cylinder head. In the equation (3.47), V_{cyl} is the instantaneous cylinder volume, and V_{bowl} is the piston bowl volume.

The mean velocity of the squish motion inside the cylinder, U_{sq}, is quantified by equation (3.48) [36]. This velocity depends in turn on its axial, U_a, and radial, U_r, components that are related to main geometric characteristics of the cylinder and piston bowl and on the cylinder volume variation rate.

$$U_{sq} = \frac{1}{3}\left(U_r\left(1 + \frac{d_{bowl}}{B}\right) + U_a\left(\frac{d_{bowl}}{B}\right)^2\right)$$

(3.48)

$$U_r = \frac{dV_{cyl}}{dt} \cdot \frac{V_{bowl}}{V \cdot (V_{cyl} - V_{bowl})} \cdot \frac{B^2 - d_{bowl}^2}{4d_{bowl}}$$

(3.49)

$$U_a = \frac{dV_{cyl}}{dt} \cdot \frac{s_{bowl}}{V}$$

(3.50)

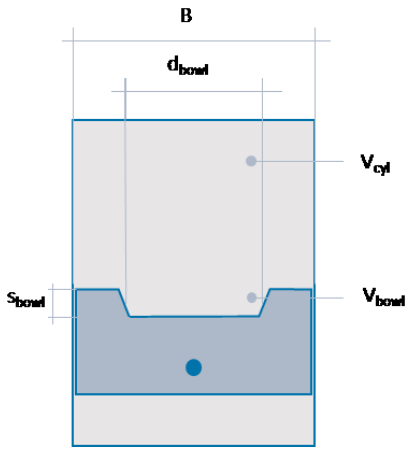

Figure 3.7 - Qualitative sketch of the main geometrical data of cylinder and piston

3.4.3.3 Production term

The energy cascade mechanism is modelled by the terms P, P_S and P_T in equations (3.30) and (3.31). Those terms are subtractive for the kinetic energy $_K$ associated to the mean flow, while they are additional terms for the turbulent kinetic energy k.

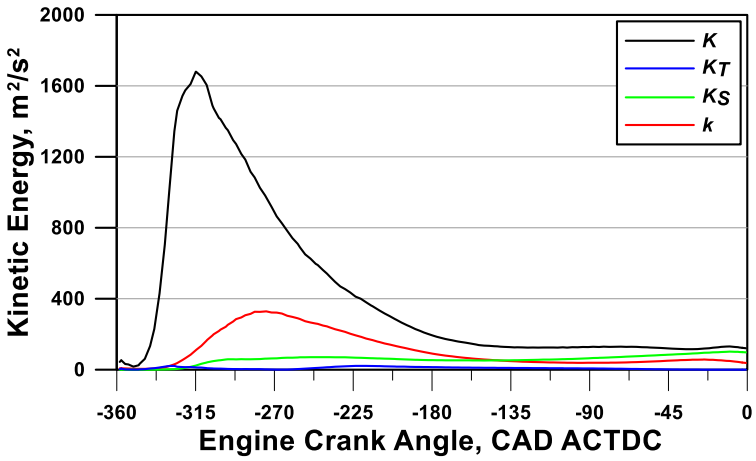

Figure 3.8 - Kinetic energies associated to mean, tumble, swirl and turbulent flows

Since most of the flow structures generated during the intake phase are unordered, the mean flow kinetic energy is significantly greater than the tumble and swirl-associated kinetic energies. In the engine design under study, the tumble motion is weak while the swirl motion is prominent. Due to the conservation of angular momentum, the swirl vortex velocity increases as the piston rises, and the swirl radius decreases as a result of the flow motion entering the piston bowl. Due to the high swirl vortex velocity, shear stresses and internal viscous forces increase the turbulence kinetic energy close to the TDC (Figure 3.8).

The turbulent production due to unordered flows is computed by the difference between the overall mean flow kinetic energy K and the ones associated to the two ordered flow motions, K_T and K_S.

$$P = c_{PKk} m \frac{K - K_T - K_S}{t_{TS}} \tag{3.51}$$

In the equation above c_{PKk} is a tuning constant to modulate the energy transfer from the mean flow to the turbulent one, t_{TS} is a characteristic time scale determined by a weighted average, equation (3.52), depending on tumble and swirl intensities, equation (3.53).

$$t_{TS} = w t_T + (1 - w) t_S \tag{3.52}$$

$$w = \frac{|U_T|}{\sqrt{U_T^2 + U_S^2}}$$

(3.53)

Ordered motions also contribute to turbulence production depending on their dissipation rates, modelled by the last terms in equations (3.32) and (3.33). The productions of turbulent kinetic energy related to tumble and swirl decays are evaluated by differentiating tumble- and swirl-related kinetic energy definitions, as reported below:

$$P_X = \frac{U_X}{r_X}\left(f_{dX}\frac{mX}{t_X}\right)$$

(3.54)

where X indicates either swirl or tumble.

3.4.3.4 Dissipation term

In the equation (3.31), the dissipation rate ε is determined through the equation (3.55).

$$L_t = c_\mu^{3/4}\frac{k^{3/2}}{\varepsilon}$$

(3.55)

where c_μ is a constant and L_t is the turbulence integral length scale. As demonstrated in prior research [37], this value varies marginally depending on the engine operations (speed, load, valve strategy, etc.), but largely depends on the engine type and combustion chamber shape. For this reason, it is imposed a sequence of S-shaped functions to describe the evolution of L_t during the engine cycle. The parameters of these functions are chosen to accommodate the L_t trend accord to results of 3D simulations.

3.4.3.5 Sensitivity analysis of the turbulence tuning constants

The turbulence model includes ten tuning constants, namely:

- c_{Kin0}, acting on mean flow production during the intake stroke;
- c_{Tin0}, acting on tumble production during the intake stroke;
- $c_{fd0,T}$, defining the offset of the decay function for the tumble because of the viscous forces;
- $c_{fdm,T}$, adjusting the intensity of the tumble collapse near the TDC;
- c_{PKk}, adjusting the turbulence production from mean flow;
- c_{Sin}, acting on swirl production during the intake stroke (inlet);
- c_{Sex}, acting on swirl production during exhaust stroke (outlet);

- $c_{fd0,S}$, defining the offset of the decay function for the swirl because of the viscous forces;
- $c_{fdm,S}$, adjusting the intensity of the swirl/squish interaction before the TDC;

To evaluate the effect of the tuning constants on the turbulence submodel, a sensitivity analysis is presented below.

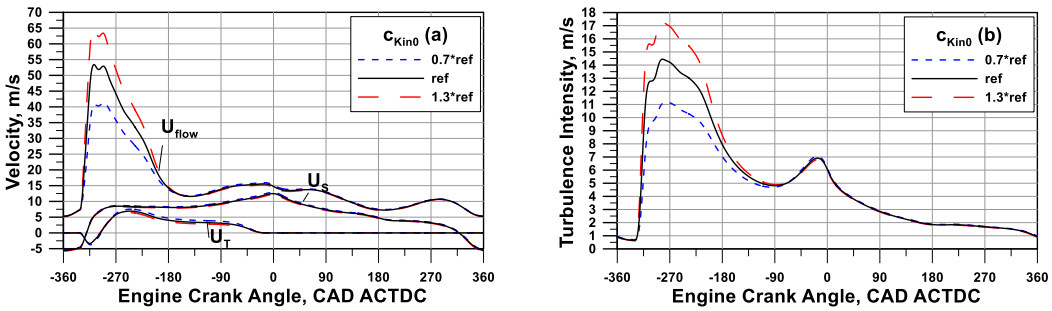

Figure 3.9 - c_{Kin0} effect on mean flow, tumble and swirl velocities (a) and turbulence intensity (b)

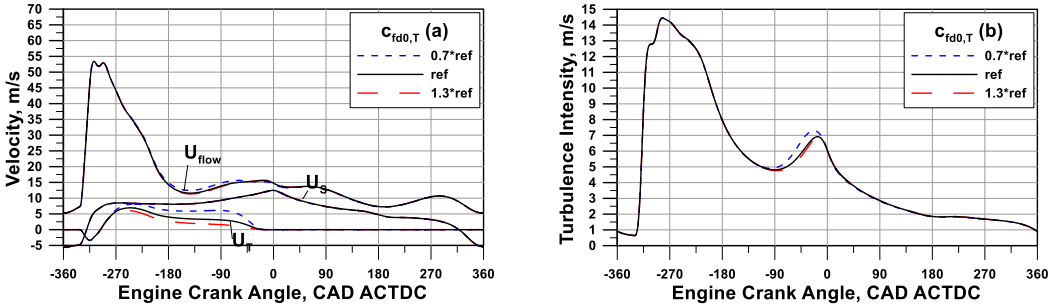

Figure 3.10 - $c_{fd0,T}$ effect on mean flow, tumble and swirl velocities (a) and turbulence intensity (b)

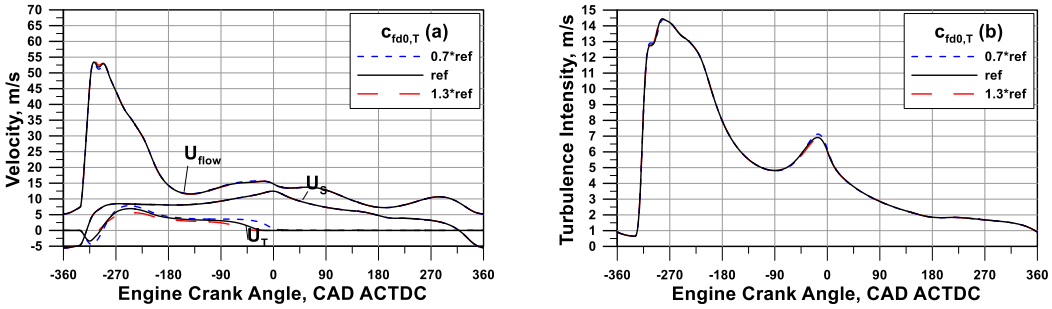

Figure 3.11 - $c_{fdm,T}$ effect on mean flow, tumble and swirl velocities (a) and turbulence intensity (b)

The Figure 3.9-3.15 depict the effect of each tuning constant, by varying those from a reference value of ±30%. The impact on the mean flow, tumble and swirl velocities is highlighted on the left figures, while the turbulence intensity variations are plotted on the right ones.

Figure 3.9 shows that c_{Kin0} significantly modifies the mean flow and the turbulence peaks in the middle of the intake stroke, which however turns in a reduced alteration of the turbulence speed-up, close to the TDC.

Figure 3.10 highlights that an increased (reduced) decay function offset, $c_{fd0,T}$, promotes (lowers) the decay of both mean flow and tumble velocities, turning in a

less (more) intense turbulence production close to the TDC. The role of $c_{fdm,T}$ is shown in Figure 3.11. This underlines that this parameter controls the crank angle of the tumble collapse, with minor impact on the turbulence peaks. In Figure 3.12, the effect of c_{PKk} is illustrated: this constant does not affect the tumble and swirl levels, while it modifies the turbulence trend during the compression stroke. It can be noted that a higher c_{PKk} determines a lower turbulence during the compression, due to a lower U, although similar u' peaks are reached before TDC.

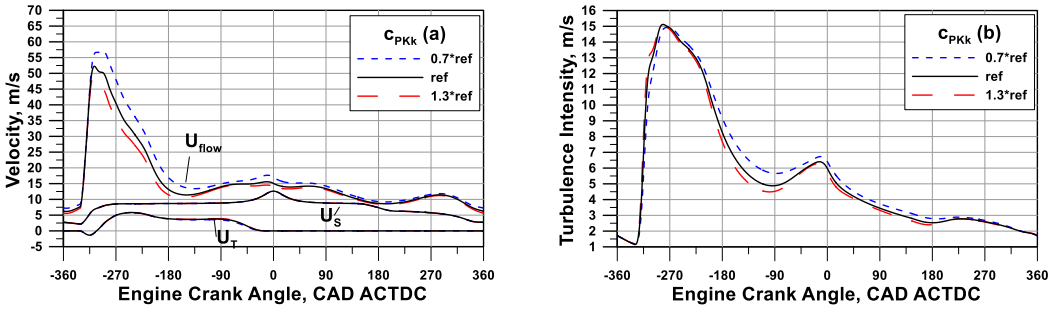

Figure 3.12 - c_{PKk} effect on mean flow, tumble and swirl velocities (a) and turbulence intensity (b)

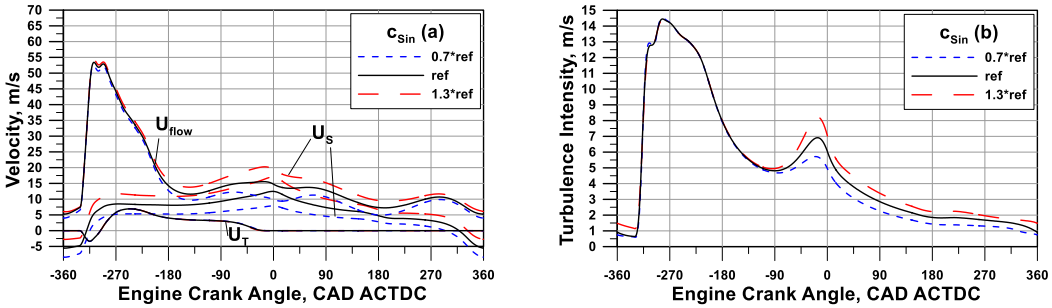

Figure 3.13 - c_{Sin} effect on mean flow, tumble and swirl velocites (a) and turbulence intensity (b)

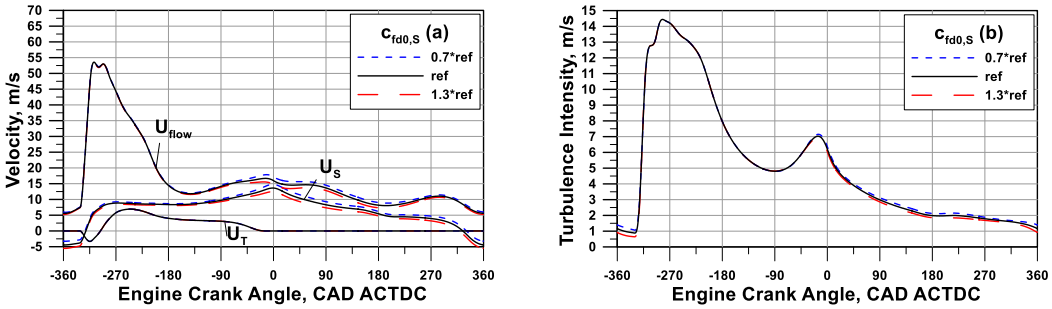

Figure 3.14 - $c_{fd0,S}$ effect on mean flow, tumble and swirl velocities (a) and turbulence intensity (b)

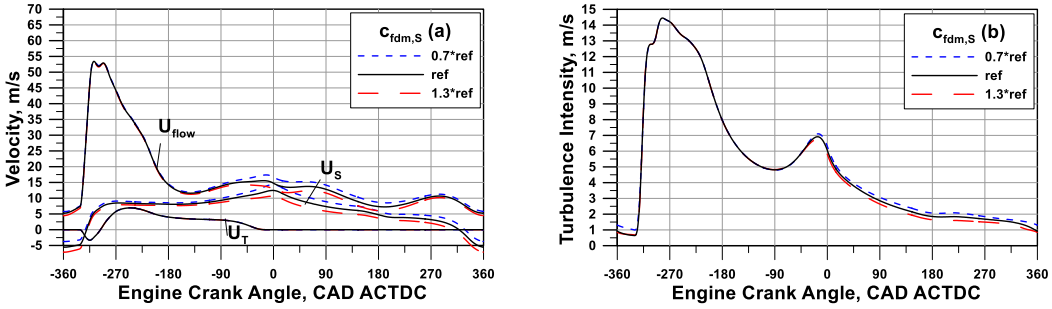

Figure 3.15 - $c_{fdm,S}$ effect on mean flow, tumble and swirl velocities (a) and turbulence intensity (b)

Figure 3.13 shows the impact of c_{Sin} on mean flow and swirl velocities. As expected, it promotes (lowers) the increasing (reducing) of swirl during the intake stroke, determining a higher (lower) initial velocity value. The generation of turbulence is given by the amount of kinetic energy in disordered form (K - K_T - K_S). Hence, despite of higher U and U_S, the production of u' in compression is not intense, then recovers to the TDC for the production term directly related to the swirl speed-up.

In the Figure 3.14 and Figure 3.15, the parameters that regulate the swirl decay function are presented. The figures highlight that the effects on mean flow and swirl velocity are qualitatively the same as the ones of tumble decay function. $c_{fd0,S}$ adjusts the swirl decay function offset, so it promotes (lowers) the decay of mean flow and swirl velocities during all cycle. $c_{fdm,S}$ controls the swirl decay around the TDC, adjusting its peak value.

Under the so far discussed sensitivity analysis, a tuning procedure can be advised. The primary step is matching the ordered flow of tumble and swirl with the 3D-derived results, adjusting firstly c_{Tin0} and c_{Sin}. Secondly, c_{Kin0} is identified to reproduce the 3D mean flow velocity peak during intake. The tumble collapse (the swirl peak) can be further handled by $c_{fd0,T}$ and $c_{fdm,T}$ ($c_{fd0,S}$ and $c_{fdm,S}$). The c_{PKk} multiplier is fine-tuned to adjust the mean flow and turbulence trends, without a significant impact on the tumble and swirl levels and turbulence speed-up before TDC.

3.4.4 *K-k-ε* Turbulence model.

A brief description of this model is presented, due to the subsequent comparison with the turbulence model developed during this research activity. This approach is embedded in the commercial software GT-SUITE and it is extensively described in [38]. It is developed for SI *tumble*-assisted engine, so this is the result of significant effort directed towards developing zero-dimensional flow models that account for its effects.

This model takes into account the energy cascade mechanism and dissipation rate description together, combined via three differential equations: one for the mean kinetic energy K, one for the turbulent kinetic energy k and one for the turbulent dissipation rate ε.

$$\frac{d(mK)}{dt} = C_{in}(1-\alpha_{in})E_{in} + K\dot{m}_{out} - P_k \tag{3.56}$$

$$\frac{d(mk)}{dt} = C_{in}\alpha_{in}E_{in} + k\dot{m}_{out} + P_k + C_{tumb}T - m\varepsilon \tag{3.57}$$

$$\frac{d(m\varepsilon)}{dt} = C_{in}E_{in}\frac{\sqrt{k}}{L_g} + \varepsilon\dot{m}_{out} + P_\varepsilon + C_{tumb}T\frac{\sqrt{k}}{L_g} - 1.92\frac{m\varepsilon^2}{k}$$

(3.58)

The above equations contain the same quantities as shown in the section 3.4.3: *K* is the mean kinetic energy, *k* is the turbulent kinetic energy and *ε* is the turbulent dissipation rate.

$$E_{in} = (1 - C_T)\frac{1}{2}\dot{m}_{in}v_{in}^2$$

(3.59)

E_{in} is the energy associated to the inlet flow, so the first term of each equation describes the production related to the flow entering the cylinder. $\dot{m}_{in}$ and v_{in}^2 are the mass flow rate and isentropic velocity of the flow entering the cylinder, respectively. C_T is the tumble coefficient associated with the valves, measured on bench and provided as input in the 0D model.

L_g is representative of a geometric length scale, defined as follow:

$$L_g = C_{len} \times \min(s, 0.5B)$$

(3.60)

where *B* is the cylinder bore and *s* the instantaneous piston stroke.

The terms P_k and P_ε model the production of turbulent kinetic energy and dissipation rate, respectively. These parameters are computed as follows:

$$P_k = C_\beta v_T\frac{2mK}{L_g^2} - \frac{2}{3}mk\left(\frac{\dot{\rho}}{\rho}\right) - \frac{2}{3}mv_T\left(\frac{\dot{\rho}}{\rho}\right)^2$$

(3.61)

$$P_\varepsilon = \frac{\varepsilon}{k}\left[5.76C_\beta v_T\frac{mK}{L_g^2} - 2mk\left(\frac{\dot{\rho}}{\rho}\right) - \frac{2.64}{3}mv_T\left(\frac{\dot{\rho}}{\rho}\right)^2\right]$$

(3.62)

where v_T is the turbulent viscosity and ρ is the density of the charge inside the cylinder.

This model, as well as the *K-k* family approaches, use tuning constants to predict the in-cylinder flow motion. The model involved four tuning constants and permits a no case-dependent calibration, responding well to different operating conditions and matching results from 3D-CFD with reasonable accuracy.

The model parameter C_{in}=0.18C_1 takes into account the actual flow velocities through the valve and C_1 is t the tuning constant that considers the magnitude of the inflow source term. C_β=0.38C_2 is a model parameter which considers the magnitude of the production source terms and C_2 is its tuning constant. The model parameter C_{len}=0.18C_3 modulates the value of the length scale, where C_3 is the associated tuning constant. The terms with the quantity T represent the generation of turbulence caused by the decay of the tumble macro-vortex during the compression stroke, whereas C_{tumb} is a tuning constant that governs the intensity of this process.

This 0D turbulence model can be calibrated to match 3D-CFD outcomes by using four tuning constants:

- C_1 – controls the levels of mean and turbulent kinetic energies during inflow into the cylinder
- C_2, C_3 – control the production of turbulence from the mean flow
- C_{tumb} – controls the contribution of tumble decay to turbulence production

3.5 Turbulent combustion modelling for Pre-chamber SI engine

Despite the various experimental studies available in the literature on a pre-chamber SI engine [39-45], numerical analyses are essential for improving and comprehending the underlying physics of this innovative architecture for on-road heavy-duty engines. In fact, technological and economic factors severely restrict experimental campaigns for this type of engine. Consequently, experimental investigations on mixture preparation and combustion development within a pre-chamber with such a small capacity can be difficult even with optical engines. In addition, the examination of the effects of various design elements, such as the placement of the injector, the position of the spark plug, and the number, length, and diameter of the holes, needs substantial time and costs. Under this perspective, a 3D-CFD model may give precise insights into the pre-chamber mixing and combustion processes, hence aiding in the appropriate comprehension and optimization of a jet ignition process. Several studies were conducted towards this goal, with some focusing on design optimization and others on the investigation of various operating situations. Shah [46] examined the influence of the pre-chamber volume and the hole diameter on jet propagation in the main chamber and concluded that the ideal design must be chosen by balancing two opposing effects. Indeed, in a smallest pre-chamber the pressure built up across the chambers causes a short burst of pre-chamber ejection instead of a long-lasting jet which promotes turbulent mixing in the main chamber. Whereas the largest pre-chamber causes sufficient pressure build-up but may not exhaust completely before main chamber ignites, hence contributing to loss in overall combustion efficiency [46]. Moreover, for a given pre-chamber volume, a smaller nozzle diameter will result in a greater flow restriction over the chamber, resulting in a high combustion enhancement, yet quenching phenomena may occur. In contrast, a larger nozzle

diameter creates short-lived bursts of pre-chamber ejection, which does not provide enough turbulence to support lean combustion. Analysed in [47] are the effects of hole orientation and pre-chamber volume on the turbulence field.

Due to the formation of tumble motion inside the pre-chamber, the results indicate a greater TKE-level at the spark plug for the larger pre-chamber. This is not the case for the smaller chamber. However, the requisite high turbulence level near the spark plug can only be obtained with a hole orientation that also creates a swirling motion. The impact of important design and engine parameters on the fluid mechanics and thermodynamic properties of active and passive pre-chambers was investigated in a more comprehensive research [48] using 3D-CFD modelling and experimental activity.

The detailed results and several others found in the literature demonstrate that the optimal chamber layout is dependent on the behaviour of a variety of pre-chamber factors in the correct combination. Therefore, a highly specialized understanding of the engine under investigation is required, since it will not be feasible to achieve all the suggested benefits merely by adding a pre-chamber to the combustion system.

The interplay between combustion, chemical kinetics, and turbulence happening in a pre-chamber engine may be best described using 3D analysis due to the complexity of all the processes described. However, due to the high computing time, the full engine working plane is hardly to explore. In contrast, this may be accomplished either by time-consuming experimentation or through a numerical engine calibration based on 0D/1D techniques, but with a loss of accuracy.

To achieve the objective, the building of the 0D/1D model had to be capable of sensing the primary physical phenomena governing the combustion process in a pre-chamber engine, which was a formidable undertaking. Clearly, the effort associated with model creation began with a review of the existing literature.

To do this, a number of models offered in the literature were evaluated for their capacity to physically represent the many events occurring in a pre-chamber. In [49], turbulence (K-k-ε) and heat transport models for a passive pre-chamber are developed. In terms of pressure traces and turbulence variables, the model is able to faithfully recreate 3D reference data. Due to the lack of linkage with a combustion model, the scope of this study was restricted to the investigation of the compression stroke. In [50], heat transmission was assessed using a PC-engine-adapted correlation. To represent the combustion processes in both chambers, a Wiebe function was imposed with the sacrifice of the model's predictability.

Other methodologies explain the combustion process in an active PC in a more phenomenological approach [51]. The early phase of MC combustion is governed, according to a prevalent theory, by a conical hot jet from the PC. As an example, a

model dependence based on the second Karlovitz number calculated at the PC hole output was introduced in [52]. Until the Karlovitz number is greater than one, it is considered that the hot jet turbulent flow created by the PC controls the combustion. Consequently, the flame propagation is considered self-sustaining, comparable to a conventional engine, due to the in-MC turbulence amplification. In [53], the combustion growth was estimated using an extra entrainment effect in which the fresh charge is entrained into the burning jet. Due to jet penetration, an increase in the flame front area was also postulated in [54]. Assumed to be a function of a typical jet length, the transition from a drop-shaped flame to a hemisphere.

Although all these methodologies provide a fairly complete description of the events happening in a pre-chamber engine, the range of validation is sometimes restricted to a small number of operating situations, particularly with regard to air/fuel quality. As a result, the dependability of these techniques is insufficient for simulating the entire engine under varying loads, speeds and mixture qualities.

3.5.1 Fractal Model description

The combustion model is an improved version of the fractal method developed at the University of Naples in the last years [14], that is described in the previous section. It has been rearranged to handle the combustion occurring in both MC and PC. In a conventional SI engine, the combustion speed is enhanced by the turbulence, which in turn is mainly produced during the intake and compression strokes.

In a PC engine, as reported in [55], the combustion in the MC is additionally promoted and supported by the turbulent jets ejecting from the PC, especially during the early combustion stage. To consider this phenomenology, the burn rate expression is computed as the sum of two terms, see eq. (3.63):

$$\left(\frac{dm_b}{dt}\right)_{overall} = \left(\frac{dm_b}{dt}\right)_{fractal} + \left(\frac{dm_b}{dt}\right)_{jet} \tag{3.63}$$

The first term describes the burning rate occurring in a conventional engine, where a corrugated thin flame front, with surface A_T, locally propagates at laminar speed, S_L:

$$\left(\frac{dm_b}{dt}\right)_{fractal} = \rho_u A_T S_L = \rho_u A_L S_L \left(\frac{A_T}{A_L}\right) = \rho_u A_L S_L \left(\frac{L_{max}}{L_{min}}\right)^{D_3-2} \tag{3.64}$$

The freshly written parameters were provided in the previous section, thus the second term of the equation (3.63) will receive more focus.

The burning rate contribution due to the turbulent jets is computed under the hypothesis that the jets entrain fresh charge (air and fuel) and that the entrained mass

progressively burns and releases heat. The heat release rate is assumed to be proportional to the difference between the current entrained mass (m_{entr}) and its burned portion ($m_{b,entr}$), and inversely proportional to a characteristic timescale τ, see eq. (3.66). Following the well-known eddy burn-up approach [17], this last is calculated as the ratio between the Taylor length scale, Λ_T, and the laminar flame speed, S_L. The current total entrained mass, m_{entr}, is computed by the integration of its time derivative, eq. (3.67), which, in turn, is estimated by the semiempirical correlation proposed in [52]. The aforesaid entrained mass rate depends on the mass flow rate coming out of the PC, $\dot{m}_{jet}$, on a tuning constant, c_{jet}, and on the density ratio between PC and MC. Similarly, the burned entrained mass, $m_{b,entr}$, is computed by the integration of eq. (3.65).

$$\left(\frac{dm_b}{dt}\right)_{jet} = \frac{dm_{b,entr}}{dt} = \left(\frac{m_{entr} - m_{b,entr}}{\tau}\right) \tag{3.65}$$

$$\tau = \frac{\Lambda_T}{S_L} \tag{3.66}$$

$$\frac{dm_{entr}}{dt} = c_{jet}\dot{m}_{jet}\sqrt{\frac{\rho_{PC}}{\rho_{MC}}} \tag{3.67}$$

The combustion start in the PC is univocally defined by the spark timing, given as a simulation input. On the contrary, the combustion onset in the MC is predicted according to the current flame radius in the PC. As soon as it exceeds a critical value, named r_{crit}, the MC combustion is activated. This parameter, directly correlated to the PC height, can be considered as an additional tuning constant, adjusting the combustion start in the MC.

The A_L in the MC is evaluated at each simulation time step as a function of the burned gas volume and of the piston position under the hypothesis of multiple spherical flame fronts propagating from the jets ejected by the PC. The centers of those spheres are supposed to be placed along the turbulent jet axis a predefined distance from the PC holes. Under the hypothesis that the flame mainly develops when the turbulent jets have almost dissipated their initial kinetic energy [56]. As for the pre-chamber, a smooth spherically shaped propagation is considered with a center moving at a speed proportional to the jet velocity. Presumed ignition sites are located along each turbulent jet, from which the flame propagates spherically. The position of

sphere centres, differently from the PC, is assumed fixed during the combustion development, assigned as an additional input parameter.

3.6 Knock and Heat Transfer modelling

During the calibration phase in the test bed, in order to avoid the occurrence of abnormal combustions, the Knock Limited Spark Advance (KLSA) has to be identified. If a numerical calibration has to be carried out, a knock model must be also coupled to the combustion model.

Auto-Ignition (AI) processes are best described using sophisticated chemical kinetic schemes, which involve hundreds of species and thousands of reactions [57]. The primary problem of this method is its high CPU use. Simpler models based on empirical formulations of auto-ignition delay [58] can be utilized. The primary shortcoming of such a formulation is the restricted ability to use the correlation outside of the air/inert/fuel quantities addressed during correlation development. In addition, the chemical effects generated by sophisticated knock suppression techniques, such as EGR or water injection, are difficult to anticipate. In [59], a tabular technique, which relies on the off-line solution of chemical processes in a Constant-Pressure (CP) or Constant-Volume (CV) reactor, is shown to provide a suitable compromise between accuracy and complexity for the estimate of the AI. The table displays the AI time, τ_{AI}, as a function of pressure, temperature, equivalence ratio and residual content. In the engine model, the knock event happens when the AI integral, given by equation (3.68), is greater than unity.

$$\int \frac{dt}{\tau_{AI}} \tag{3.68}$$

In fact, to generate a tiny safety margin, a threshold level that is adjustable below the unit threshold is defined. As previously stated, the AI table is derived from the off-line solution of a kinetic scheme conducted at different pressure, temperature, and air-to-fuel ratios for the unburned reactants in a reactor with constant pressure.

The pre- and main-chamber heat transfer is represented by a Hohenberg-like correlation [4]. This correlation calculates the gas-cylinder wall heat transfer as a function of the instantaneous volume, pressure, and temperature of the cylinder. The average piston speed also considers the engine speed. In the case of the PC, the extent of heat transfer is considered to be governed only by the in-PC pressure and temperature, while engine rotating speed is ignored. No special method is used to evaluate the heat losses in the PC holes.

Reference

1. De Nola, F., Giardiello, G., Gimelli, A., Molteni, A. Muccillo, M., "Definition of a Methodology Promoting the Use of 1D Thermo-Fluid Dynamic Analysis for the Reduction of the Experimental Effort in Engine Base Calibration," SAE Technical Paper, 2019-24-0013, 2019, doi:10.4271/2019-24-0013.
2. Boretti, A. Scalzo, J., "Exploring the Advantages of Variable Compression Ratio in Internal Combustion Engines by Using Engine Performance Simulations," SAE Technical Paper 2011-01-0364, 2011, doi:10.4271/2011-01-0364.
3. Woschni, G. "A universally applicable equation for the instantaneous heat transfer coefficient in the internal combustion engine," SAE Technical paper, 670931, 1967, doi:10.4271/670931.
4. Hohenberg, G., "Advanced Approaches for Heat Transfer Calculations," SAE Technical Paper 790825, 1979, doi:10.4271/790825.
5. Thermodynamics and Fluid Mechanics Group, Annand, W., "Heat transfer in the cylinders of reciprocating internal combustion engines," Proceedings of the Institution of Mechanical Engineers, 177(1), 973-996,1963, doi:10.1243/PIME_PROC_1963_177_069_02.
6. Ghojel, J. I. (2010). Review of the development and applications of the Wiebe function: a tribute to the contribution of Ivan Wiebe to engine research. International Journal of Engine Research, 11(4), 297-312.
7. Demesoukas, S., Caillol, C., Higelin, P., Boiarciuc, "Zero-Dimensional Spark Ignition Combustion Modeling-A Comparison of Different Approaches", SAE Technical Paper, 2013-24-0022, 2013, doi:10.4271/2013-24-0022.
8. Richard, S., Bougrine, S., Font, G., Lafossas, F.A., Le Berr, F., "On the Reduction of a 3D CFD Combustion Model to Build a Physical 0D Model for Simulating Heat Release, Knock and Pollutants in SI Engines", Oil & Gas Science and Technology 64(3):223-242, 2009, doi:10.2516/ogst/2008055.
9. Matthews, R., D., Chin, Y., W., "A Fractal-Based SI Engine Model: Comparisons of Predictions with Experimental Data", SAE transactions 910075, 1991, doi:10.4271/910079.
10. Perlman, C., Frojd, K., Seidel, L., Tuner, M. et al., "A Fast Tool for Predictive IC Engine In-Cylinder Modelling with Detailed Chemistry," SAE Technical Paper 2012-01-1074, 2012, doi:10.4271/2012-01-1074.
11. Rakopoulos, C., Michos, C., Giakoumis, E., "Thermodynamic analysis of SI engine operation on variable composition biogas-hydrogen blends using a quasi-dimensional, multi-zone combustion model," SAE International Journal Engines 2(1):880-910, 2009, doi:10.4271/2009-01-0931.

12. Verhelst, S., Sheppard, C., G., W., “Multi-zone thermodynamic modelling of spark-ignition engine combustion–an overview,” Energy Conversion and management 50(5): 1326-1335, 2009, doi:10.1016/j.enconman.2009.01.002.
13. Franke, C., Wirth, A., Peters, N., “New Aspects of the Fractal Behaviour of Turbulent Flames,” 23 Symp. (Int.) on Combustion, Orleans, 1990.
14. De Bellis, V., Severi, E., Fontanesi, S., Bozza, F., “Hierarchical 1D/3D approach for the development of a turbulent combustion model applied to a VVA turbocharged engine. Part II: Combustion model,” Energy Procedia 45, 1027-1036, 2014, doi:10.1016/j.egypro.2014.01.108.
15. De Bellis, V., Bozza, F. and Tufano, D., “A Comparison Between Two Phenomenological Combustion Models Applied to Different SI Engines,” SAE Technical Paper, 2017-01-2184, 2017, doi:10.4271/2017-01-2184.
16. Blizard, N. and Keck, J., "Experimental and Theoretical Investigation of Turbulent Burning Model for Internal Combustion Engines," SAE Technical Paper 740191, 1974, doi:10.4271/740191.
17. Keck, J., Heywood, J., and Noske, G., "Early Flame Development and Burning Rates in Spark Ignition Engines and Their Cyclic Variability," SAE Technical Paper 870164, 1987, doi:10.4271/870164.
18. Tabaczynski, R., J. “Turbulence and turbulent combustion in spark-ignition engines”, Progress in energy and combustion science 2(3) 143-165, 1976, doi: https://doi.org/10.1016/0360-1285(76)90010-1.
19. Dai, W., Davis, G., Hall, M., and Matthews, R., "Diluents and Lean Mixture Combustion Modeling for SI Engines with a Quasi-Dimensional Model," SAE Technical Paper 952382, 1995, doi:10.4271/952382.
20. Morel, T., Rackmil, C., Keribar, R., and Jennings, M., "Model for Heat Transfer and Combustion In Spark Ignited Engines and its Comparison with Experiments," SAE Technical Paper 880198, 1988, doi:10.4271/880198.
21. Gouldin, F., “An application of Fractals to Modeling Premixed Turbulent Flames”, Combustion and Flame 68(3):249-266, 1987, doi:10.1016/0010-2180(87)90003-4.
22. Gatowsky, J., A., Heywood, J., B., “Flame Photographs in a Spark-Ignition Engine”, Combustion and Flame 56:71-81, 1984.
23. Bates, C., S., “Flame Imaging Studies of Combustion Completion in a SI Four-Stroke Engine”, TvU Thoughtventions Unlimited LLC, http://www.tvu.com/.
24. North, G., L., Santavicca, D., A., “The fractal nature of premixed turbulent flames,” Combustion Science and Technology 72(4-6): 215-232, 1990, doi:10.1080/00102209008951648.
25. Peters, N., “Laminar flamelet concepts in turbulent combustion,” Symposium (International) on Combustion 21(1): 1231-1250, 1988, doi:10.1016/S0082-0784(88)80355-2.

26. Rhodes, D. B., Keck, J. C. “Laminar burning speed measurements of indolene-air-diluent mixtures at high pressures and temperatures,” SAE Technical Paper, 850047, 1985.
27. Hara, T., Tanoue, K. “Laminar flame speed of ethanol, n-heptane, iso-octane air mixtures,” JSAE paper, 20068518, 2006.
28. Bougrine, S., Richard, S., Nicolle, A., Veynante, D. “Numerical study of laminar flame properties of diluted methane-hydrogen-air flames at high pressure and temperature using detailed chemistry,” International journal of hydrogen energy 36(18), 12035-12047, 2011, doi:10.1016/j.ijhydene.2011.06.053.
29. Hann, S., Grill, M., & Bargende, M. “Reaction Kinetics Calculations and Modeling of the Laminar Flame Speeds of Gasoline Fuels,” SAE Technical Paper, 2018-01-0857, 2018, doi:10.4271/2018-01-0857.
30. Gülder, Ö. L. “Correlations of laminar combustion data for alternative SI engine fuels,” SAE Technical Paper, 841000, 1984, doi: 10.4271/841000.
31. Amirante, R., Distaso, E., Tamburrano, P., and Reitz, R.D., “Laminar Flame Speed Correlations for Methane, Ethane, Propane and their Mixtures, and Natural Gas and Gasoline for Spark-Ignition Engine Simulations,” International Journal of Engine Research 18(9):951–970, 2017, doi:10.1177/1468087477200018.
32. Amirante, R., Distaso, E., Tamburrano, P., and Reitz, R.D., “Analytical Correlations for Modeling the Laminar Flame Speed of Natural Gas Surrogate Mixtures,” Energy Procedia 126:850–857, 2017, doi:10.1016/j.egypro.2017.08.289.
33. Teodosio, L., Bozza, F., Tufano, D., Giannattasio, P. et al., “Impact of the Laminar Flame Speed Correlation on the Results of a Quasi-Dimensional Combustion Model for Spark-Ignition Engine,” Energy Procedia 148:631–638, 2018, doi:10.1016/j.egypro.2018.08.151.
34. Heywood, J.B., Internal Combustion Engine Fundamentals. Vol. 930 (New York: Mcgraw-Hill, 1988), ISBN:007028637X.
35. Riccardi, M., De Bellis, V., Sforza, L., Beatrice, C. et al., "Advanced Turbulence Model for SI Combustion in a Heavy-Duty NG Engine," SAE Technical Paper 2022-01-0384, 2022, https://doi.org/10.4271/2022-01-0384.
36. Franken, T., Sommerhoff, A., Willems, W., Matrisciano, A. et al., "Advanced Predictive Diesel Combustion Simulation Using Turbulence Model and Stochastic Reactor Model," SAE Technical Paper 2017-01-0516, 2017, doi:10.4271/2017-01-0516.
37. Bozza, F., Teodosio, L., De Bellis, V., Fontanesi, S. et al., “Refinement of a 0D Turbulence Model to Predict Tumble and Turbulent Intensity in SI

Engines. Part II: Model Concept, Validation and Discussion," SAE Technical Paper 2018-01-0856, 2018, doi:10.4271/2018-01-0856.
38. Fogla, N., Bybee, M., Mirzaeian, M., Millo, F. et al., "Development of a K-k-ε Phenomenological Model to Predict In-Cylinder Turbulence," SAE Int. J. Engines 10, no. 2 (2017): 562-575, doi:10.4271/2017-01-0542.
39. Noguchi, M., Sanda, S. and Nakamura, "Development of Toyota lean burn engine," SAE Technical Paper, 760757, 1976, doi:10.4271/760757.
40. Pape, J., Getzlaff, J., Gruenig, C., Kuhnert, D. and Latsch, R., "Investigations on Pre-Chamber Spark Plug with Pilot Injection," SAE Technical Paper 2007-01-0479, 2007, doi:10.4271/2007-01-0479.
41. Attard, W.P., Fraser, N., Parsons, P. and Toulson, E., "A Turbulent Jet Ignition Pre-Chamber Combustion System for High Fuel Economy Improvements in a Modern Vehicle Powertrain," SAE Technical Paper 2010-01-1457, 2010, doi:10.4271/2010-01-1457.
42. Roethlisberger, R., Favrat, D., "Comparison between direct and indirect (prechamber) spark ignition in the case of a cogeneration natural gas engine, part I: engine geometrical parameters," Applied Thermal Engineering, 22(11), 1217-1229, 2002, doi:10.1016/S1359-4311(02)00040-6.
43. Xu, G., Wright, Y., Schiliro, M., Boulouchos, K., "Characterization of combustion in a gas engine ignited using a small un-scavenged pre-chamber," International Journal of Engine Research, 2018, doi: 10.1177/1468087418798918.
44. Jamrozik, A., "Lean combustion by a pre-chamber charge stratification in a stationary spark ignited engine," Journal of Mechanical Science and Technology, 29(5):2269-2278, 2015, doi:10.1007/s12206-015-0145-7.
45. Toulson, E., Schock, H., Attard, W., "A Review of Pre-Chamber Initiated Jet Ignition Combustion Systems," SAE Technical Paper 2010-01-2263, 2010, doi:10.4271/2010-01-2263.
46. Shah, A., Tunestål, P., Johansson, B., "CFD Simulations of Pre-Chamber Jets' Mixing Characteristics in a Heavy Duty Natural Gas Engine," SAE Technical Paper 2015-01-1890, 2015, doi:10.4271/2015-01-1890.
47. Serrano, D., Zaccardi, J.M., Müller, C., Libert, C. Habermann, K., "Ultra-Lean Pre-Chamber Gasoline Engine for Future Hybrid Powertrains," SAE Technical Paper, 2019-24-0104, 2019, doi:10.4271/2019-24-0104.
48. Sens, M., Binder, E., Benz, A., Kramer, L., at all. "Pre-chamber ignition as a Key Technology for Highly Efficient SI Engines-New Approaches and Operating Strategies," 39th International Vienna Motor Symposium, Apr. 2018
49. Bardis, K., Xu, G., Kyrtatos, P., Wright, Y. et al., "A Zero Dimensional Turbulence and Heat Transfer Phenomenological Model for Pre-Chamber Gas

Engines," SAE Technical Paper 2018-01-1453, 2018, doi:10.4271/2018-01-1453.
50. Cruz, I., Alvarez, C., Teixeira, A., Valle, R., "Zero-dimensional mathematical model of the torch ignited engine," Applied Thermal Engineering, 103, 1237-1250, 2016, doi:10.1016/j.applthermaleng.2016.05.017.
51. Kouremenos, D.,A, Rakopoulos C.,D., Hountalas, D., D. "Thermodynamic Analysis of Indirect Injection Diesel Engines by Two-Zone Modeling of Combustion", ASME. J. Eng. Gas Turbines Power, 112(1):138-149, 1990. doi:10.1115/1.2906468.
52. Hiraoka, K., Nomura, K., Yuuki, A., Oda, Y. et al., "Phenomenological 0-Dimensional Combustion Model for Spark-Ignition Natural Gas Engine Equipped with Pre-Chamber," SAE Technical Paper 2016-01-0556, 2016, doi:10.4271/2016-01-0556.
53. Shojaeefard, M. H., Keshavarz, M. "Flame propagation model for a rotary Atkinson cycle SI engine," International Journal of Automotive Technology, 19(1), 9-25, 2018, doi:10.1007/s12239-018-0002-7.
54. Auer, M., Wachtmeister, G. "Phenomenological models for pre-calculation of the combustion in gas engines," MTZ worldwide,70(6), 52-59, 2019, doi:10.1007/BF03226962.
55. Mueller, C., Morcinkowski, B., Habermann, K., Uhlmann, T., Schernus, C. "Development of a Pre-Chamber for Spark Ignition Engines in Vehicle Applications," in 4th International Conference on Ignition Systems for Gasoline Engines, Dec. 2018.
56. Mastorakos, E., Allison, P., Giusti, A., De Oliveira, P. et al., "Fundamental Aspects of Jet Ignition for Natural Gas Engines," SAE Int. J. Engines 10(5):2429-2438, doi:10.4271/2017-24-0097.
57. Lu, T., Law C., "Toward accommodating realistic fuel chemistry in large scale computations," Progress in Energy and Combustion Science 35(2):195-215, 2009, doi:10.1016/j.pecs.2008.10.002.
58. Livengood, J., C., Wu, P., C., "Correlation of Autoignition Phenomena in Internal Combustion Engines and Rapid Compression Machines," Symposium (International) on Combustion 5(1):347-356, 1955, doi:10.1016/S0082-0784(55)80047-1.
59. Bozza, F., De Bellis, V. Teodosio, L., "A Tabulated-Chemistry Approach Applied to a Quasi-Dimensional Combustion Model for a Fast and Accurate Knock Prediction in Spark-Ignition Engines" SAE Technical Paper, 2019-01-0471, 2019, doi: 10.4271/2019-01-0471.

4 Assessment of the advanced turbulent combustion model for a heavy-duty SI CNG fuelled engine

The first phase carried out during the PhD research work was focused on the assessment of the turbulence and fractal combustion models on a SI diesel-derived heavy-duty engine fuelled with CNG.

4.1 Engine description

The main features of the engine under study (Figure 4.1) are reported in Table 4.1. This engine is designed to guarantee long-distance when installed on heavy-duty trucks (over 16 tons of gross vehicle weight). It is a heavy-duty, turbocharged SI engine with a compression ratio of 12:1. The considered engine is retrofitted from a Compression Ignition (CI) application, through the installation of ported CNG injectors and spark-plugs. The CNG is injected through a Multi Point Injection (MPI) system, and it is metered to ensure a close-to-stochiometric air/fuel mixture in the combustion chamber.

The load control is realized by the waste-gated turbocharger at mid/high load, and by the throttle valve at low load. An intercooler is located after the compressor to limit the inlet temperature of the air. Each cylinder is equipped with a centred spark-plug, and two intake and exhaust valves, both with fixed timing (Figure 4.2).

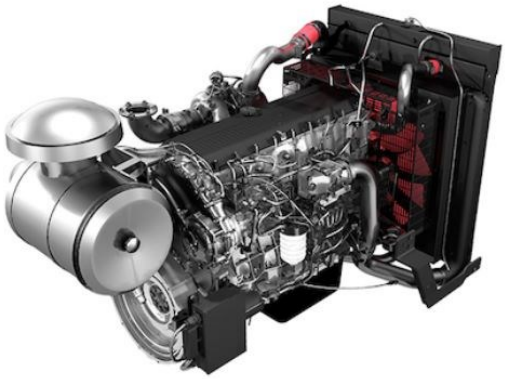

Figure 4.1 - Overview of the 6-cylinder engine under exam

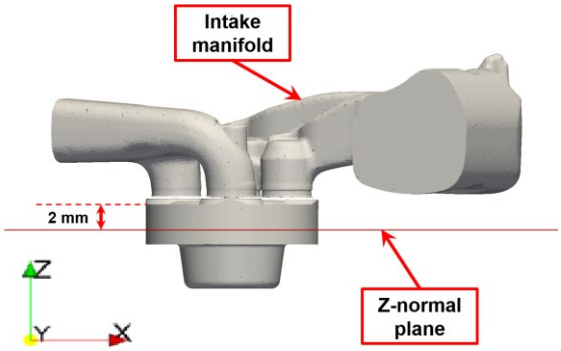

Figure 4.2 - Layout of the intake and exhaust systems, with the piston at the TDC position (numerical domain for the 3D-CFD simulations)

The experimental campaign is carried out at Istituto di Scienze e Tecnologie per l'Energia e la Mobilità Sostenibili (STEMS), analysing the engine at full- and part-load conditions. The engine is tested at five different speeds from 1100 up to 1900, for 5 different load levels. In total, 25 operating points, listed in Table 4.2, are investigated, identified by the couple engine speed and load (rpm@BMEP). For each condition, overall performance data, such as Brake Specific Fuel Consumption (BSFC), fuel rate, and emissions are collected. Additionally, the instantaneous pressure cycle is recorded through a pressure transducer, and post-processed to derive

the angular positions of representative combustion stages (spark event and 10%, 50% as well as 75% of Mass Fraction Burned).

Table 4.1 - Main features of the selected CNG SI heavy-duty engine

Turbocharged SI Engine	
Cylinder Arrangement	6l (in-line) vertical
Displacement, l	12.85
Compression Ratio	12:1
Stroke, mm	150 mm
Bore, mm	135 mm
Valves per cylinder	4
Bowl depth	~30 mm
Bowl radius	~37 mm
Average squish height	~2.5 mm @ TDC
Maximum brake power, kW	338 @ 1900 rpm
Maximum brake torque, Nm	2000 @ 1100 / 1620 rpm
Injection System	MPI
Valve number	4
IVO – IVC at 2 mm lift, CAD AFTDC	383-515
EVO – EVC at 2 mm lift, CAD AFTDC	146-333
External EGR	NO

Looking at combustion phasing in Table 4.2, expressed by the Crank Angle Degree (CAD) at which 50% of the mixture is burned (MFB_{50}), it is evident that the engine works at knock-limited conditions for the higher loads. Whereas for BMEP levels below 13 bar, the typical optimal MFB_{50} around 8-10 CAD is detected, which leads to the maximum brake torque efficiency.

Table 4.2 - List of operating points

Case	**Operating condition rpm @ BMEP [bar]**		**SA CAD BFTDC**	**MFB_{50} CAD AFTDC**
1	1900	16.6	13.8	17.5
2		13.3	16.6	14.1
3		10.0	23.5	7.5
4		6.6	26.2	6.6
5		3.3	25.8	9.7
6	1620	19.4	11.3	19.0
7		15.6	13.4	16.4
8		11.7	19.1	10.4
9		7.8	24.3	7.0
10		3.9	23.8	10.0
11	1500	19.4	10.7	19.2
12		15.6	13.0	16.1

13		11.7	18.7	10.3
14		7.8	23.0	7.5
15		3.9	23.8	10.0
16	1300	19.5	9.9	18.4
17		15.6	12.2	15.2
18		11.7	17.9	10.3
19		7.8	20.8	8.9
20		3.9	22.4	10.1
21	1100	19.5	9.0	17.7
22		15.6	11.1	15.0
23		11.7	16.7	9.9
24		7.8	18.3	9.9
25		3.9	19.7	11.3

4.2 Tuning and validation of the turbulence model

This section presents the predictions of the 0D flow/turbulence model, developed during this research activity, at 2 operating conditions and compares them to the results obtained via 3D-CFD simulations, widely detailed in [1]. The operating conditions considered are at 1200 rpm and 1900 rpm, whose main engine settings are listed in Table 3.

A single-cylinder 1D model of the engine under study is developed within a commercial software (GT-Power) based on a 0D/1D modeling environment, where the engine is schematized through a network of 1D pipes and 0D volumes. The 0D flow/turbulence pattern is implemented as user sub-model using GT-Power tools and it ran in motored conditions just to evaluate the cold flow impact on turbulence generation, with no combustion influence.

The 3D-CFD simulations of the gas exchange process were performed by PoliMi research group with Lib-ICE software, which is a code based on the OpenFOAM technology and extensively used for simulating IC engines for both academical and industrial tasks [2, 3, 4]. The tumble and swirl radii, r_T and r_S, derived from 3D analyses are here defined as:

$$r_T = \frac{\sum_{cyl} m_i[(x_i - x_G)^2 + (z_i - z_G)^2]}{\sum_{cyl} m_i \sqrt{(x_i - x_G)^2 + (z_i - z_G)^2}} \quad (4.1)$$

$$r_S = \frac{\sum_{cyl} m_i[(x_i - x_G)^2 + (y_i - y_G)^2]}{\sum_{cyl} m_i \sqrt{(x_i - x_G)^2 + (y_i - y_G)^2}}$$

(4.2)

where mi is the mass in the *i*th cell; x_i, y_i, z_i are the Cartesian coordinates of the *i*th cell center; and x_G, y_G, z_G are the Cartesian coordinates of the in-cylinder mass center. The tumble and the swirl radii are here defined around the y-axis and z-axis, respectively (see Figure 4.2).

Table 4.3 - The investigated operating conditions

Operating condition	***Cruise***	***Max power***
Engine speed [rpm]	1200	1900
Brake torque [Nm]	850	1700
Brake power [kW]	100	338
Air-fuel ratio λ	1	1
EGR [%]	14.5	11.2

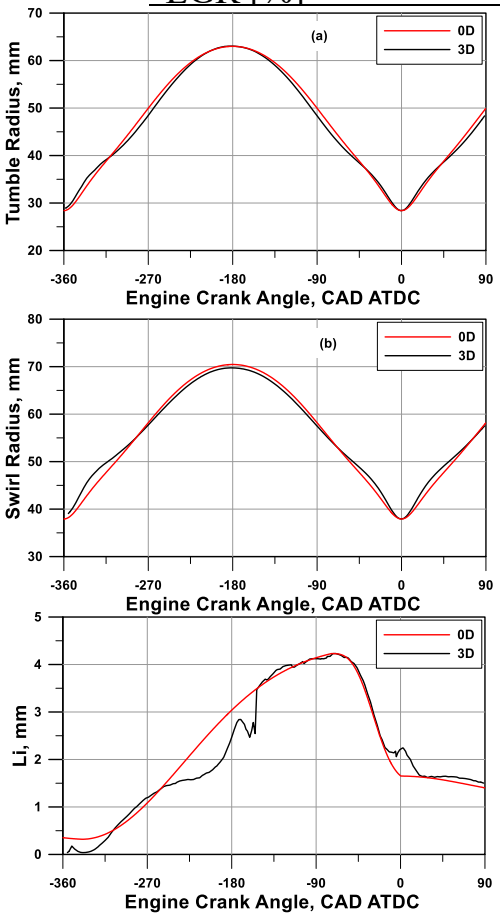

Figure 4.3 - Comparison between 3D-CFD and 0D results of tumble (a) and swirl (b) radii and normalized integral length scale (c).

The flow/turbulence model is tuned manually through a simple trial and error procedure to obtain a good match of all quantities of interest with 3D results. These last are synthesized in scalar quantities through mass-averaging process within the cylinder. Since 3D simulations started at the beginning of the exhaust phase, with null initial swirl, and covered a single engine cycle, a full cycle-by-cycle convergence is

not reached. All the 0D/3D comparisons presented below cover intake, compression and a portion of expansion stroke, when cyclic convergence can be assumed adequate. The values of the flow/turbulence model constants after the tuning are listed in the Table 4. They are kept fixed for the tested operating conditions, with no case-dependent specific tuning.

As mentioned previously in this *K-k-T-S* model, some data, more related to geometrical characteristics of the engine and combustion chamber, are not calculated, but imposed according to predefined patterns. Using equation (3.46), the radii of tumble and swirl are determined by modifying the c_{r0X} and c_{rmX} parameters to match the 3D levels at BDC and TDC, respectively. Similarly, the integral length scale is computed by assigning levels at certain angular points (firing TDC, minimum and maximum levels during intake and compression strokes). Figure 4.3 demonstrates that the 0D patterns properly match the 3D counterparts, particularly during the intake and compression strokes, which are the most significant phases for a good forecast of combustion. 3D-CFD simulations revealed no notable variations in the outcomes of tumble/swirl radius and integral length scale for the two analysed engine rotational speeds. Thus, 0D/3D assessment is only presented for the speed of 1900 rpm.

Table 4.4 - Values of flow model tuning constants

Tuning constant	**Value**	**Tuning constant**	**Value**
c_{Kin0}	0.60	c_{Sin}	0.08
c_{Tin0}	0.45	c_{Sex}	0.02
$c_{fd0,T}$	0.55	$c_{fd0,S}$	0.05
$c_{fdm,T}$	1.0	$c_{fdm,S}$	1.0
c_{PKk}	3.5		

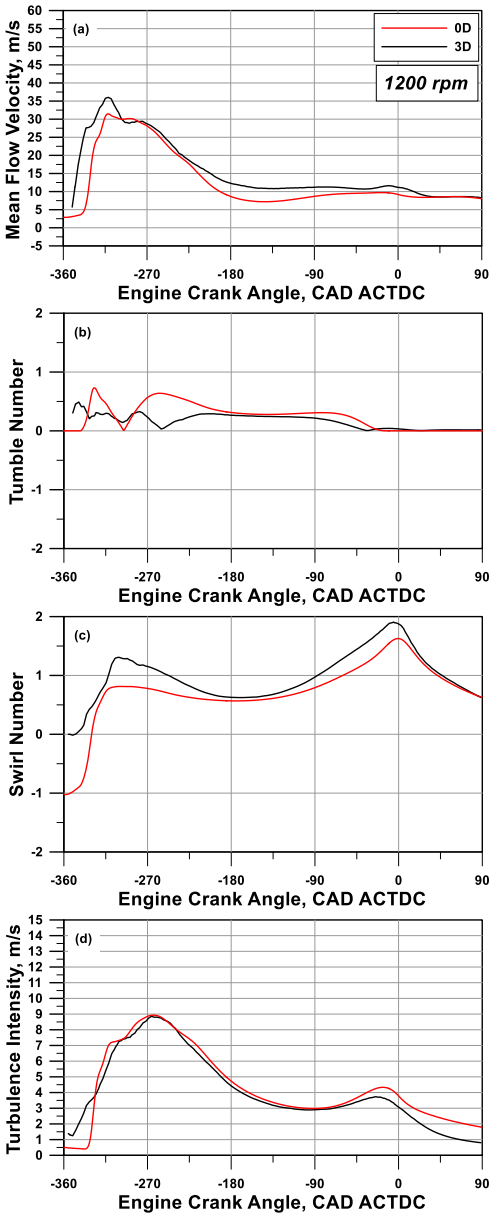

Figure 4.4 - Comparison between 3D-CFD and 0D results at 1200 rpm of mean flow velocity (a), tumble number (b), swirl number (c) and turbulence intensity (d).

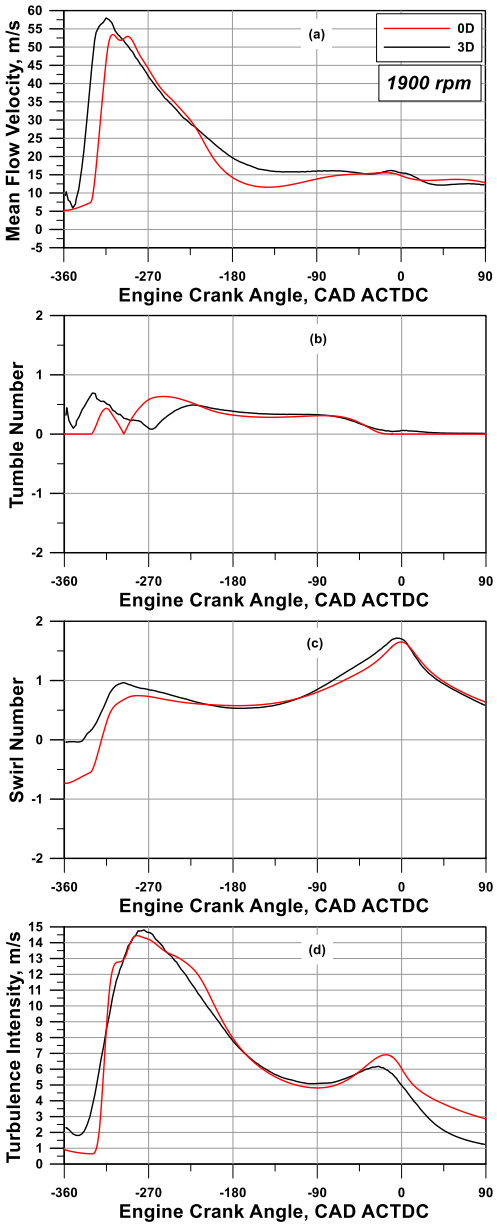

Figure 4.5 - Comparison between 3D-CFD and 0D results at 1900 rpm of mean flow velocity (a), tumble number (b), swirl number (c), and turbulence intensity (d).

Figure 4.4 and Figure 4.5 shows that the overall behaviour of the model is quite satisfactory in the comparison with 3D outcomes, for both the analysed operating conditions. Although the simulations were carried out for the entire engine cycle, only between -360 and 90 CAD is shown, because in this angular arc the spark ignition starts. The mean flow velocity, the tumble number, the swirl number, and the turbulence intensity denote a very good agreement with the related 3D profiles, during most of the engine cycle. The mean flow velocity, tumble and swirl, increases during the intake phase due to incoming flow through the intake valve. According to expectations, those velocities appropriately scale with engine rotational speed, passing from 1200 rpm to 1900 rpm. After a partial decay during the ending part of the intake phase, mean flow velocity persists and even accelerates near TDC because of the swirl motion speeding up. The swirl radius reduces, approaching the TDC, due

to the smaller volume available in the combustion chamber, so for the angular momentum conservation, the swirl velocity enhances. The squish is not directly described by a dedicated equation, but its effects are indirectly taken into account as energy lost in the decay of the swirl.

As emerged from 3D analyses, tumble momentum presents comparable components around two principal axes (x-axis and y-axis) perpendicular to the cylinder symmetry axis (z-axis). For this reason, those momentum components are combined according to:

$$T_{XY} = \sqrt{T_X^2 + T_Y^2} \tag{4.3}$$

For sake of consistency, the absolute values of 0D-computed tumble number are compared to 3D results in Figure 4.4b and Figure 4.5b. The 0D prediction appears quite poor during the intake phase, due to its incapability to reproduce multiple and unstructured tumble eddies generated during this phase in the engine under study. The model accuracy drastically improves during the compression stroke, where tumble collapse towards TDC is quite well captured.

Looking at Figure 4.4c and Figure 4.5c, the tumble and swirl number profiles are overall satisfactorily reproduced during most of the engine cycle, with a higher accuracy towards the ending portion of the compression stroke, when the contribution of those motions to turbulence generation become more relevant. The turbulent intensity is satisfactorily predicted in the 0D pattern over the considered portion of the engine cycle. During the intake phase and the early stage of the compression stroke, 0D turbulence prediction mainly relies on accuracy in the simulation of mean flow velocity. Near to the TDC, the characteristic speed-up of turbulence intensity is captured by the model through the cascade mechanisms of kinetic energy from unordered and ordered flows to smaller scales.

4.2.1 Comparison with GT-Suite turbulence model

In this section a comparison of 0D results between the above-mentioned *K-k-T-S* turbulence model and the commercial code embedded in the GT-Suite v.2016 tool is shown, with the purpose to evaluate pros and cons of both turbulence models.

The *K-k-ε* model calibration is completed with the purpose to match the peak of in-cylinder turbulence intensity in the crank angular degrees range in which the combustion starts. The calibration strategy is a trial and error one and a no case-dependent specific tuning is approached.

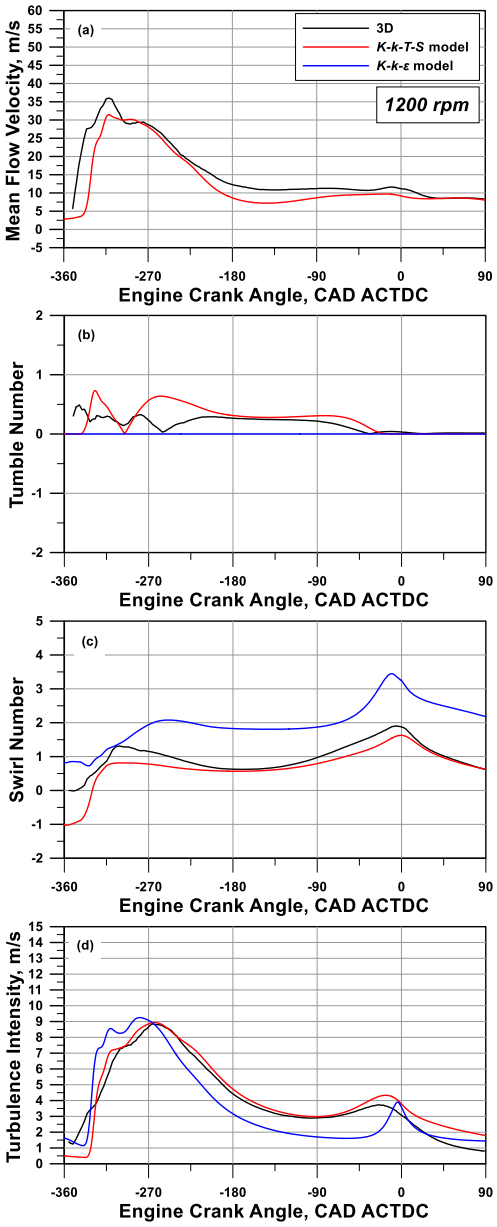

Figure 4.6 - Comparison between 3D-CFD and 0D results at 1200 rpm of mean flow velocity (a), tumble number (b), swirl number (c) and turbulence intensity (d) for K-k-T-S and K-k-ε models.

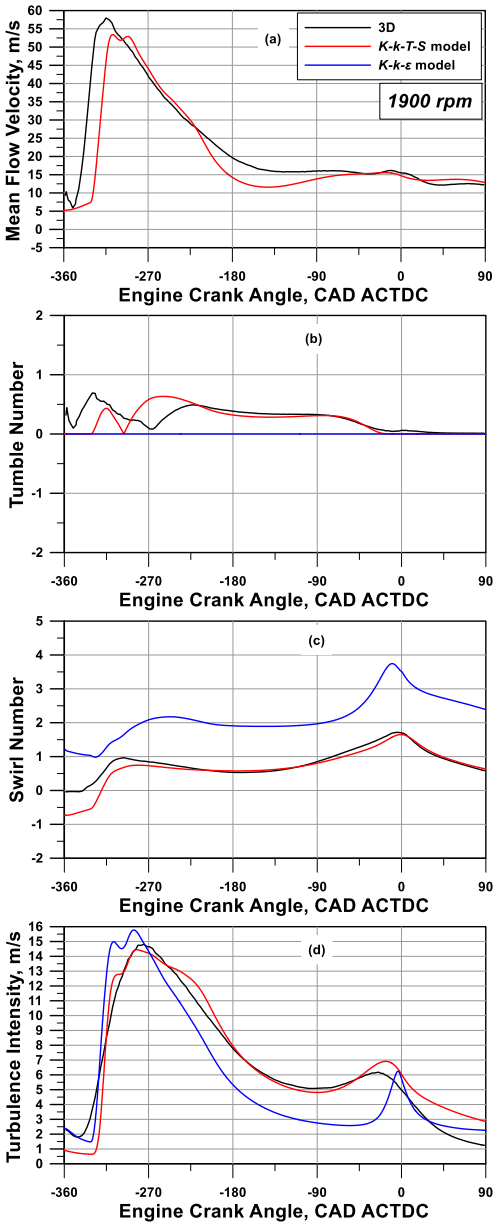

Figure 4.7 - Comparison between 3D-CFD and 0D results at 1900 rpm of mean flow velocity (a), tumble number (b), swirl number (c) and turbulence intensity (d) for K-k-T-S and K-k-ε models.

K-k-ε model available in GT-Power v2016 does not permit to tune the tumble and swirl evolution inside the cylinder during the compression stroke. In GT-Power v2019, a tuning constant was introduced which allows to modulate the tumble decay, but this is not the case of swirl motion. *K-k-ε* model initialize tumble and swirl by the steady related coefficients of intake valve/port, obtained by experimental tests or by 3D steady simulations. In the case of the considered engine, tumble coefficient data were not available, while the 0D predicted swirl was too high compared to the one evaluated through 3D simulations. Among the pros of this model there is certainly the possibility of calibrating it using less tuning constants, see Table 4.5, but the *K-k-ε* model is not able to obtain the same results as the *K-k-T-S* one, both with regard to the ordered and unordered flows. The *K-k-T-S* model needs to be calibrated by more tuning constants, but this obstacle is easily avoided by using a calibration strategy

that is presented in section 3.4.3.5. In addition, *K-k-T-S* turbulence model is able to replicate in-cylinder flow motion for all engine type, tumble- and swirl-assisted one, just by intervening on the proper tuning constants.

Table 4.5 - Values of K-k-ε model tuning constants

Tuning constant	**Value**	**Tuning constant**	**Value**
C_1	3.0	C_2	3.0
C_3	0.3	C_{tumb}	1.0

4.2.2 Comparison with *K-k-T* turbulence model

In this section a comparison of 0D results between the *K-k-T* model and the *K-k-T-S* one is shown. The *K-k-T* turbulence model, is a previous step of the turbulence model developed during this research activity, presented extensively in [5]. It considered not only an equation for the kinetic energy of the mean flow, *K*, and one of the turbulent flow, *k*, but also an equation for the specific angular momentum of the tumble motion, *T*. In tumble-assisted SI engines, this model is highly recommended, but in the engine under exam, where the combustion chamber is in the piston crown and the cylinder head has a flat geometry, the flow motion during the intake phase is mainly governed by the *swirl* motion rather than *tumble* one. Figure 4.8 and Figure 4.9 depict the comparisons between the results of the presented *K-k-T-S* model and the ones of the *K-k-T* variant. The figures show that the novel model is able to obtain a better prediction of mean flow kinetic energy around the FTDC. On the opposite, the *K-k-T* model does not perceive the effect of swirl motion in sustaining the mean flow velocity when the piston moves around the FTDC. This reflects in an improved turbulence estimation by the *K-k-T-S* model, especially for the higher rotational speed.

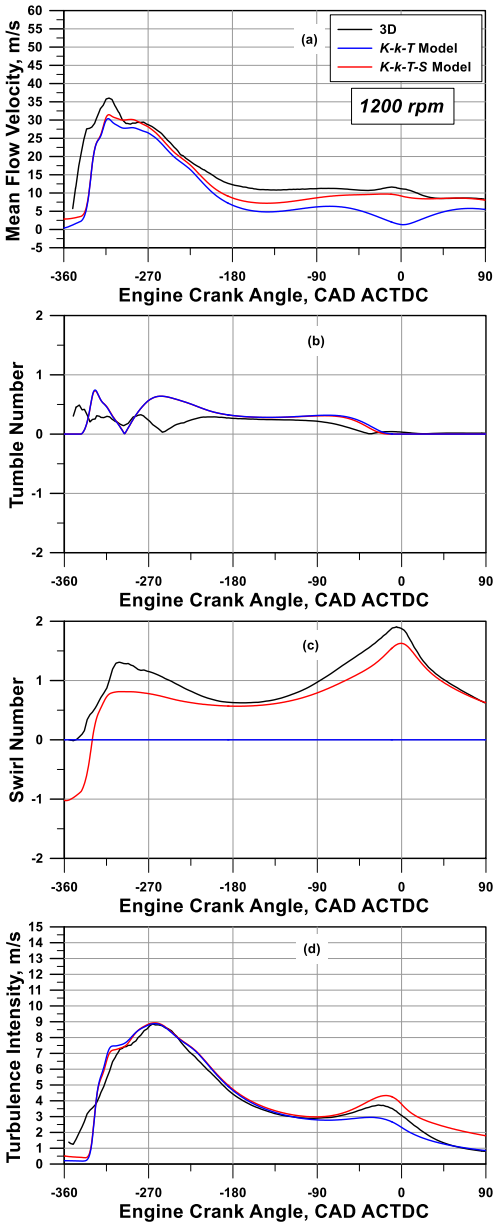

Figure 4.8 - Comparison between 3D-CFD and 0D results at 1200 rpm of mean flow velocity (a), tumble number (b), swirl number (c) and turbulence intensity (d) for K-k-T-S and K-k-T models.

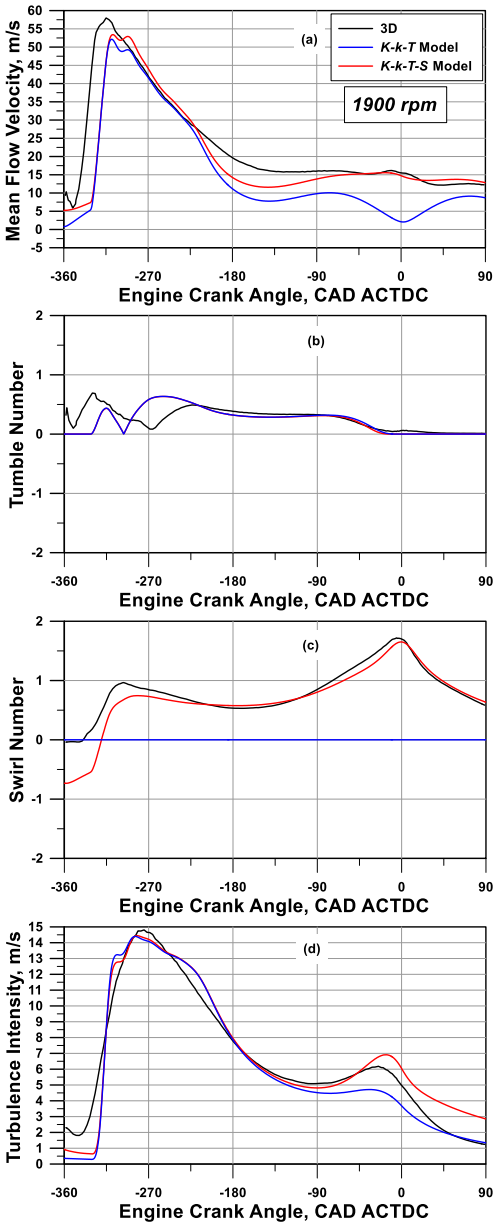

Figure 4.9 - Comparison between 3D-CFD and 0D results at 1900 rpm of mean flow velocity (a), tumble number (b), swirl number (c) and turbulence intensity (d) for K-k-T-S and K-k-T models.

4.3 Fractal combustion model tuning and validation

The model of the engine under study is developed within a 0D/1D environment, where the engine is schematized through a network of 1D pipes and 0D volumes. The turbocharger system is handled by a standard map-based approach, whereas the in-cylinder phenomena are described by refined, in-house developed, phenomenological sub-models for turbulence, combustion, and heat transfer.

To reproduce in the 1D model the same operating conditions experienced in the experimental campaign, some control parameters are imposed as a simulation input. More specifically, the fuel is automatically metered to match the measured air/fuel ratio, whereas two PIDs are introduced for load control. The former acts on the turbocharger wastegate opening, which targets the measured boost level. The latter

modifies the throttle valve position, following the measured BMEP level. The experimentally-derived MFB50 is imposed in the simulations, iteratively adjusting the SA at run-time, until the prescribed MFB50 is matched.

4.3.1 Laminar flame speed correlation

As already pointed out, for the estimation of the burn rate, a laminar flame speed correlation is required. The laminar flame speed experimental-derived correlation presented in section 3.4.2 is utilized, recalled here:

$$S_L(\phi, T_u, p) = S_{L0}\left(\frac{T_u}{T_0}\right)^{\alpha}\left(\frac{p}{p_0}\right)^{\beta} \tag{4.4}$$

In the experimental activity, the fuel injected in the combustion chamber is a CNG, whose average composition is summarized in Table 4.6. The fuel is mainly composed by methane (84.78 %) and ethane (8.88%), with a similar percentage of molecular nitrogen (1.90 %), propane (1.88%) and carbon dioxide (1.87%). The remaining 0.69 % is composed of 4 minor species. Depending on the feedstock quality, some small variations may however occur.

Table 4.6 - Composition of CNG used in the experiments.

Fluid		**Volume percentage**
Methane	CH_4	84.78 %
Ethane	C_2H_6	8.88 %
Nitrogen	N_2	1.90 %
Propane	C_3H_8	1.88 %
Carbon Dioxide	CO_2	1.87 %
N-Butane	C_4H_{10}	0.50 %
N-Pentane	C_5H_{12}	0.08 %
Helium	He	0.07 %
N-Hexane	C_6H_{14}	0.04 %

In order to better assess the impact of the CNG composition, and particularly of the ethane and propane content on S_L, a preliminary analysis is carried out. To this aim, two different fuels are considered, the former is composed of pure methane (with χ_1=χ_2=0), the latter is a mixture of propane, methane and ethane, with a percentage of 89%, 9%, 2%, respectively (labelled in the following as CNG surrogate). The correlation predicted influence of the equivalence ratio on the laminar flame speed is

represented in Figure 4.10 at various temperature and pressures, for pure methane and CNG surrogate. The S_L differences between pure CH_4 and the blend are negligible. Minor differences only occur under very-lean or very-rich conditions. In the light of the above comparisons and considering that the tested engine works under close-to-stochiometric conditions, it was assumed to treat the CNG as a pure methane for the S_L calculation, neglecting the presence of any other species.

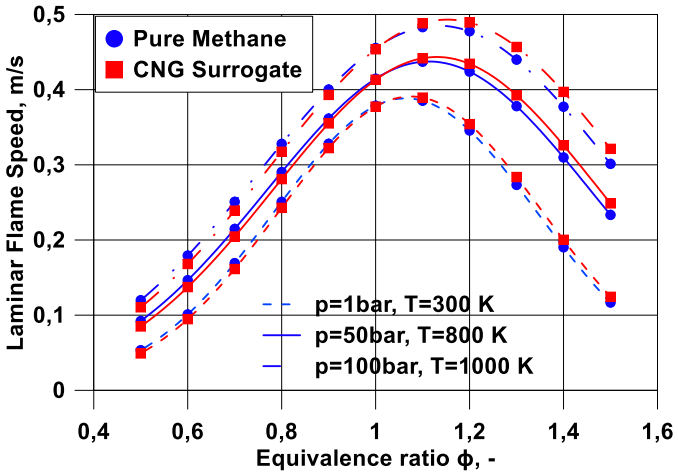

Figure 4.10 - Comparison of the predicted laminar flame speed as a function of the equivalence ratio for pure methane and CNG surrogate.

4.3.2 Model tuning

The combustion model is firstly tuned at full load curve, to minimize the overall speed-averaged error between the computed and experimental characteristics combustion angles. To this aim, three tuning constants have to be specified, each of them acting, as said, on a specific phase of the combustion process, namely the transition between an initially laminar to a fully-turbulent combustion, the fully-developed flame wrinkling, and the combustion tail. Using a trial-and-error procedure, a single set of tuning constants is identified, following the steps presented in [6], whose tuning constants are defined in section 3.4.2:

1. $MFB_{10\text{-}50}$ error is minimized by c_{wrk} adjustments;
2. $MFB_{0\text{-}10}$ error is controlled by c_{trans} tuning;
3. $MFB_{50\text{-}75}$ error is minimized by a proper x_{wc} selection.

In Figure 4.11, the results of the full-load curve tuning procedure are reported in terms of characteristic combustion events, namely SA, MFB_{10}, MFB_{50}, and MFB_{75}. Since the MFB_{90} is always hard to measure experimentally due to the inaccuracy to catch the end of combustion, MFB_{75} is considered to adjust the speed of the combustion tail.

Since the MFB_{50} is imposed in the calculations, the combustion model accuracy can be mainly appreciated in terms of experimental/numerical comparison on the SA.

A slow initial burning rate, expressed as [MFB_{10}-SA] duration, is evident in the results. Being the considered engine retrofitted from a CI application, a low turbulence level is established inside the combustion chamber, which lengthens the transition from an initially laminar to a fully-turbulent combustion. Since the phenomenon is directly considered in the model, a good match of both the SA and the MFB_{10} can be observed. The burning speed during the combustion core, expressed in terms of [MFB_{50}-MFB_{10}], is also very well reproduced.

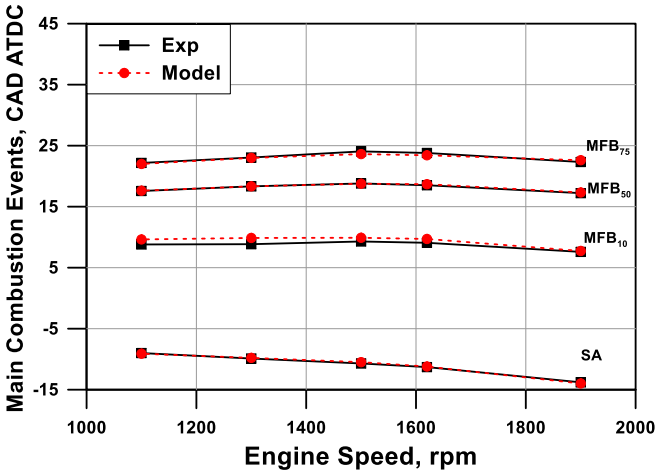

Figure 4.11 - Experimental vs numerical comparison of characteristic combustion angles at full load.

4.3.3 Model validation

Once tuned at full load, the combustion model is applied to the analysis of all the other operating points listed in Table 4.2, using the same set of previously defined tuning constants. Firstly, the model validation is proved in terms of global performance, where the Root Mean Squared Error (RMSE) is presented as a global indicator of the model accuracy.

$$RMSE = \sqrt{\sum_{i=1}^{N} (z_{f_i} - z_{o_i})^2 / N} \tag{4.5}$$

To show the model sensitivity to the engine load, in Figure 4.12-Figure 4.18, the five load levels tested at each speed (see Table 4.2) have been differenced by various symbols and colours.

In Figure 4.12 the measured and computed air flow rates are compared. The RMSE is rather low (10.92 kg/h) and all the analysed points are within the error band ± 5%, denoting an accurate schematization of the engine geometry, of the turbocharging system, and a proper specification of the valve flow coefficients.

The experimental/numerical correlation between the main combustion events is reported in Figure 4.13-Figure 4.14, while in Figure 4.15 is shown the burn duration. Globally, the model produces with good accuracy the prediction of all these quantities. In particular, the SA is well-captured with an RMSE of about 1.15 CAD (Figure 4.13). Since the load spans from 20% to 100% of the full load, this result can be considered excellent, being the model capable to perceive the progressive advance of the spark timing at reducing load. This is obtained thanks to the ability to consider the superimposed effects of the simultaneous decrease of in-cylinder turbulence, pressure and temperature. The good accuracy in the prediction of combustion phases for all load levels is further confirmed by Figure 4.14 in which the numerical/experimental correlation of MFB_{10} is shown. Even for the MFB_{10} the accuracy is very good, in fact, the error never exceeds ±2 CAD for all the prescribed loads, with an RMSE of 0.84 CAD.

The burn duration is again considered between 10% and 75% of the fuel burned. In Figure 4.15, the burn duration prediction is good in comparison with the measured counterparts, with a RMSE of 0.77 CAD, confirming the robustness of both combustion and turbulence models.

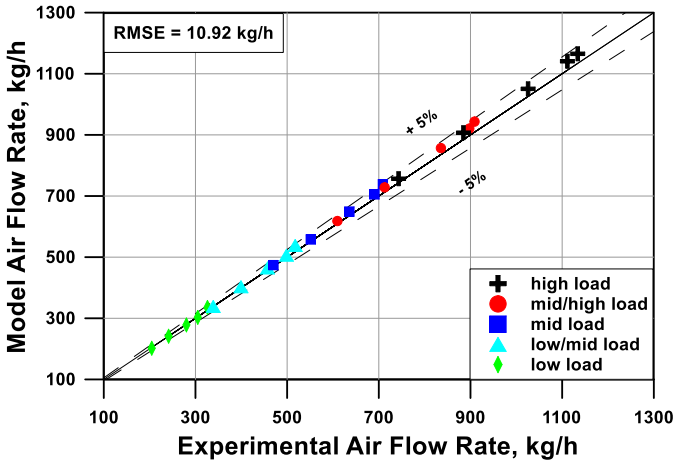

Figure 4.12 - Experimental vs numerical airflow rate comparison.

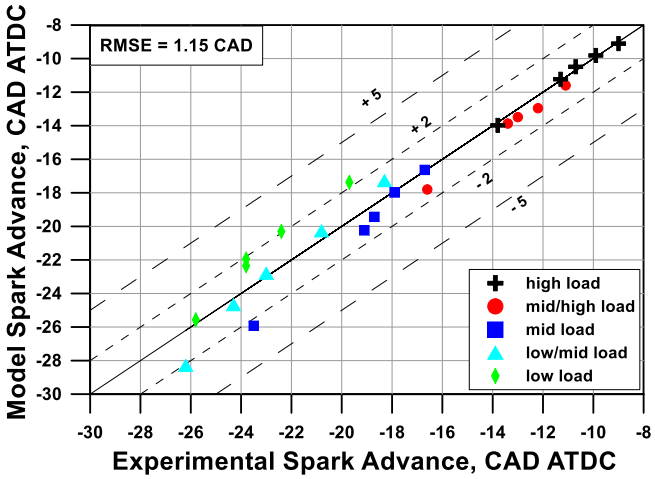

Figure 4.13 - Experimental vs numerical spark advance comparison.

The above combustion results can be considered overall satisfactory, taking into account that no case-dependent tuning is applied, and the assessment includes both full and part load operating points. The globally appropriate accuracy in the combustion process description is confirmed by the numerical/experimental comparisons of peak pressure level, depicted in Figure 4.16. The peak pressure level is to some extent overestimated / underestimated at high / low-load, but always inside a range of ±5%, with an RMSE of 0.74 bar.

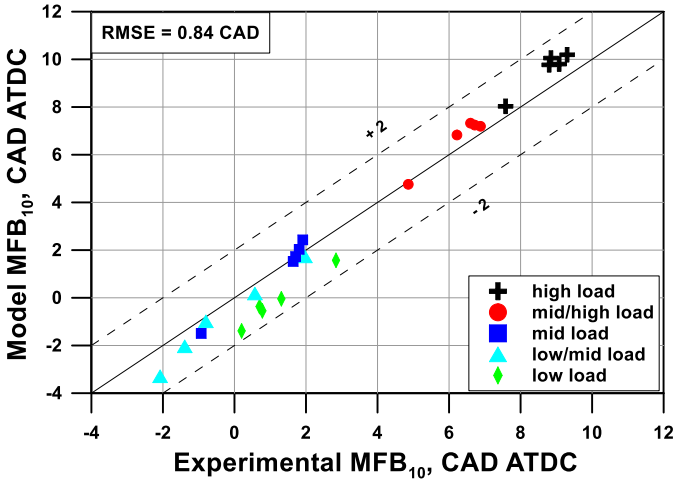

Figure 4.14 - Experimental vs numerical MFB_{10} comparison.

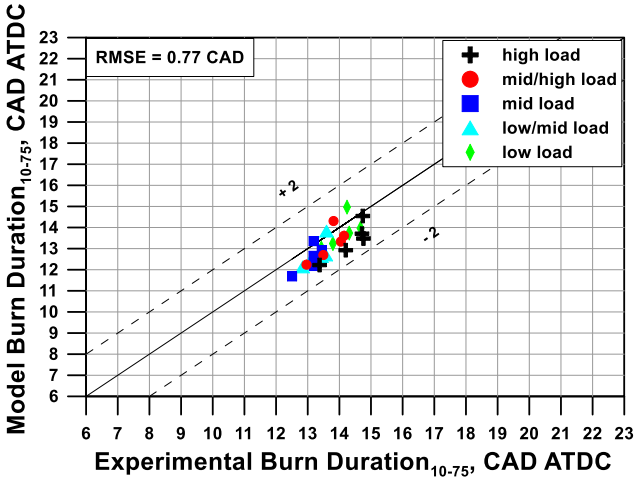

Figure 4.15 - Experimental vs numerical Burn Duration 10-75 comparison.

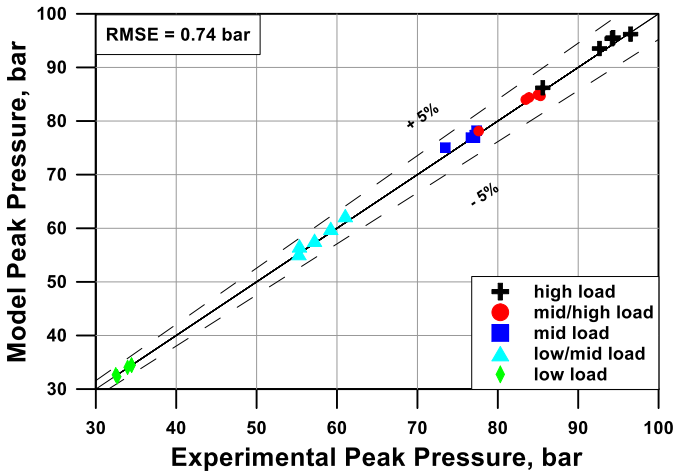

Figure 4.16 - Experimental vs numerical pressure peak comparison.

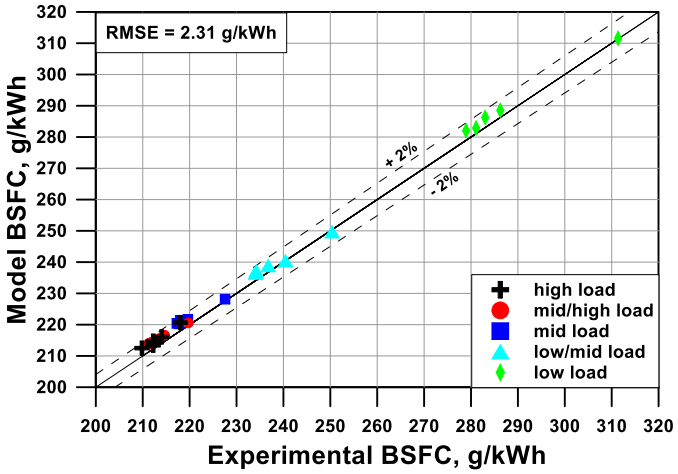

Figure 4.17 - Experimental vs numerical BSFC comparison.

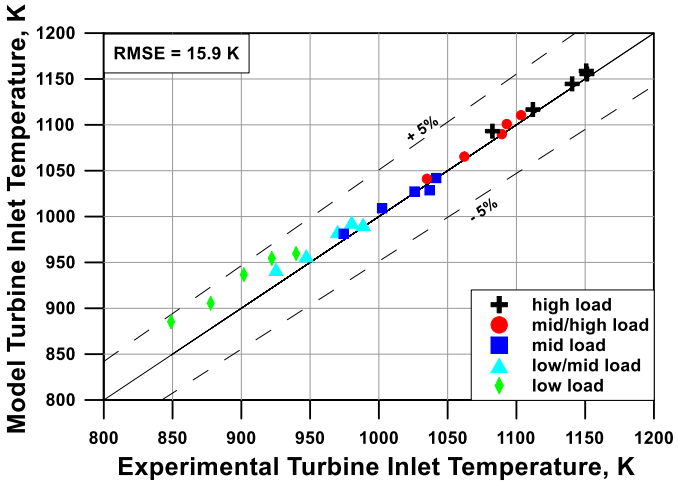

Figure 4.18 - Experimental vs numerical turbine inlet temperature.

As a further confirmation of the model reliability in terms of wall heat transfer, flow, and combustion prediction, the BSFC comparison is reported in Figure 4.17. All the operating points are included in the band ± 5%, with an RMSE equal to 2.31 g/kWh. The highest errors occur systematically at low loads, where the fuel consumption is slightly overestimated.

In Figure 4.18 the correlation between experimental data and numerical results on turbine inlet temperature is shown. The accuracy is good, with an RMSE equal to 15.9 K. A little overestimation for low load levels is observed, but numerical results are always in the range of ±5% of deviation, depicting a good calibration of both in-cylinder and exhaust pipes wall heat transfer.

An additional experimental/numerical comparison concerns the NO_x emissions, reported in Figure 4.19. The extended Zeldovich mechanism, applied without any tuning, demonstrates to be reliable enough in sensing both load and speed variations, with a RMSE of about 109 ppm.

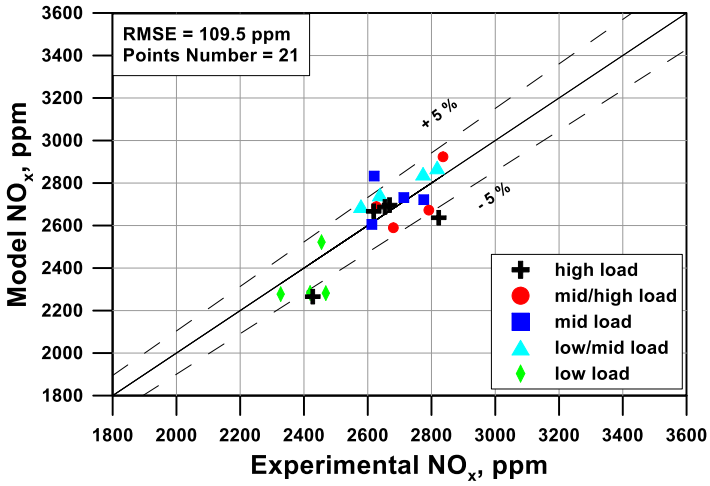

Figure 4.19 - Experimental vs numerical NO_x raw emissions

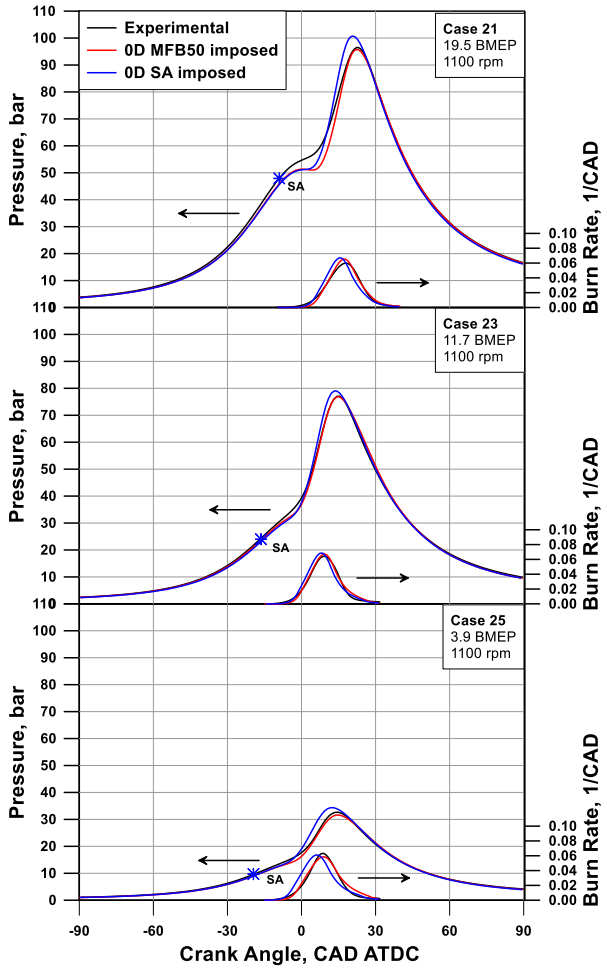

Figure 4.20 - Experimental vs numerical comparison of in-cylinder pressure traces and burn rates at 1100rpm@ 19.5 (a), 11.7 (b), 3.9 (c) BMEP.

A more impressive check of the simulation reliability is given by the experimental/numerical comparisons of the pressure traces and the related burn rates, shown in Figure 4.20-Figure 4.22. In particular, nine representative operating points from Table 4.2 are selected, at different engine speeds and loads. The black lines represent the experimental traces, whereas the red ones correspond to the model outcomes. The comparison is done for mean pressure cycles, experimental traces are obtained for 200 firing cycles with a percentual error of 1%.

The agreement between experimental/numerical pressure trends is quite good in terms of global shape, timing and peak levels for all the analysed operating points. During the compression stroke, a slight underestimation of the pressure traces is visible with a higher extent at increasing load. The underestimation of the pressure traces could be probably due to the prediction of a slightly faster combustion, with delayed beginning, which reflects in lower pressure levels around the TDC. At this stage of the research activity, a model of kernel development is not considered, but this is expected to improve the model predictivity. Another possible reason for pressure mismatch around the TDC could be some inaccuracy in the experimental measurement of the boost level, which is targeted in the model by the turbocharger

WG control. Regarding the burn rate, the model well follows the experimental profiles, detecting the evident slow-down when the load decreases. The demonstrated accuracy of the combustion model, as already mentioned, mainly relies on the capability to perceive superimposed effects of in-cylinder, turbulence, pressure, temperature and residual content.

For sake of completeness, the 1D simulations are repeated with experimental SA imposed and the corresponding results are plotted in Figure 4.20-Figure 4.22 with blue lines. In this case, the model tuning is kept unchanged to have a fair comparison with results with MFB50 imposed. The figures put into evidence that the model accuracy slightly worsens when imposing the SA instead of the MFB50. This modelling lack is expected to improve with a better description of the early combustion stage, including the flame kernel formation and development.

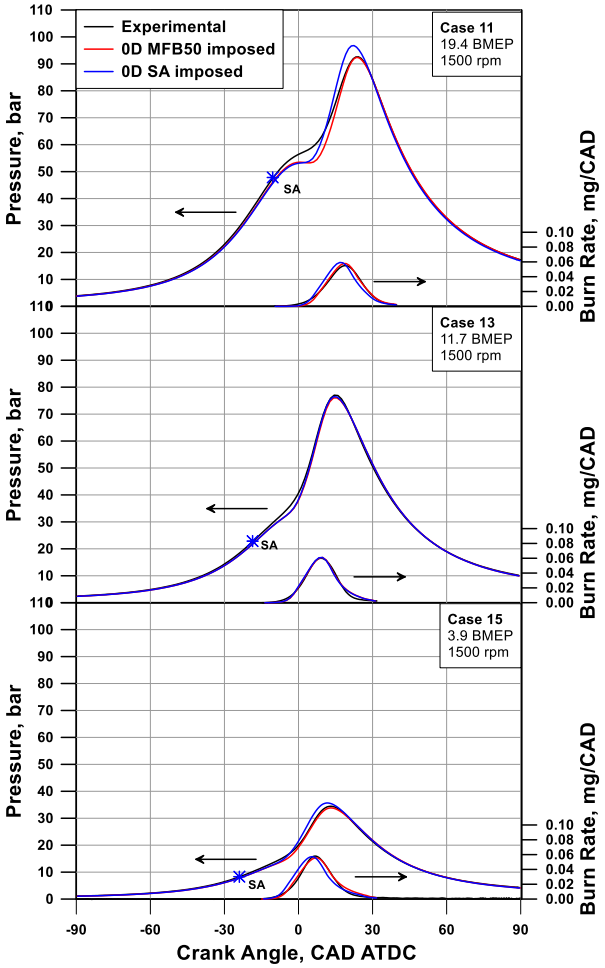

Figure 4.21 - Experimental vs numerical comparison of in-cylinder pressure traces and burn rates at 1500 rpm@ 19.4 (a), 11.7 (b), 3.9 (c) BMEP.

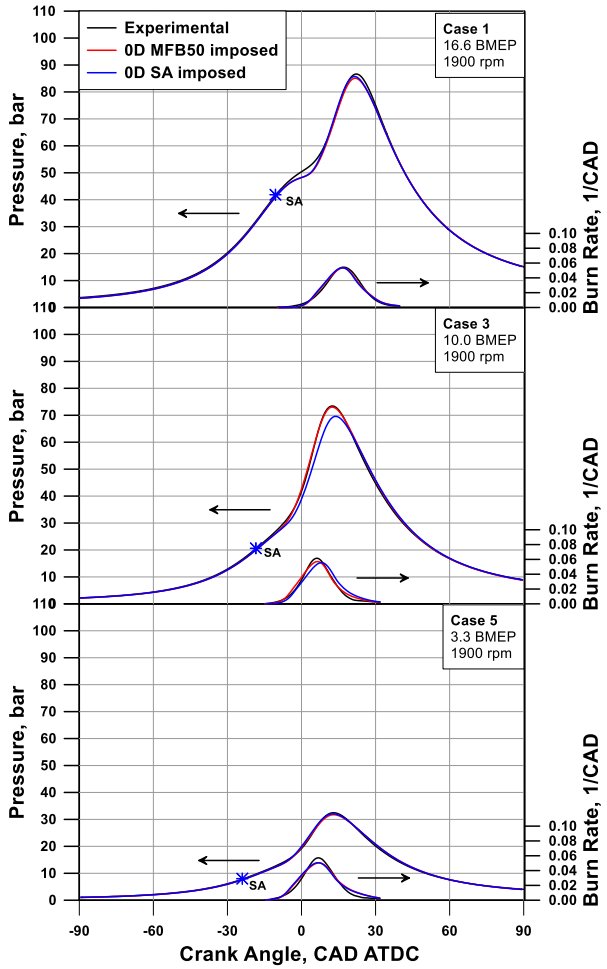

Figure 4.22 - Experimental vs numerical comparison of in-cylinder pressure traces and burn rates at 1900 rpm@ 16.6 (a), 10.0 (b), 3.3 (c) BMEP.

4.4 Comparison with Eddy burn-up combustion model

In this section a comparison of the results obtained by the two above-mentioned predictive combustion model, the fractal and the eddy burn-up one, is described. The aim of this activity is to evaluate the predictive capabilities of both combustion models in terms of characteristic combustion events and burn rate profiles.

The formulation of the considered combustion models and their main differences have been discussed in the section 3.4. However, in order to carried out a proper assessment, some common aspects are preserved. In particular, they are coupled to the same turbulence sub-model, laminar flame speed correlation and laminar flame front area evaluation.

Turbulence parameter required by the combustion models are derived by the same *K-k-T-S* turbulence model, due to its better reliability for this type of engine. The laminar flame speed is computed by the same numerical correlation, equation (4.4), for the same fuel compositions (Table 4.6).

Combustion start can be specified in a 1D model in two different ways: the measured SA is directly assigned, and the MFB_{50} is numerically estimated, or, alternatively, the

experimentally-derived MFB_{50} can be assigned. In the latter case, the SA is changed at each simulation period through a controller, until the computed MFB_{50} matches the experimental value. This option is followed here, in order to ensure a combustion development with similar in-cylinder conditions for both combustion models. Model accuracy is hence estimated in terms of predicted SA and combustion durations.

In a first stage, the combustion models have been tuned at full load, see Figure 4.23, then the identified optimal constants for both models, reported in Table 4.7, are kept fixed for all 25 operating points.

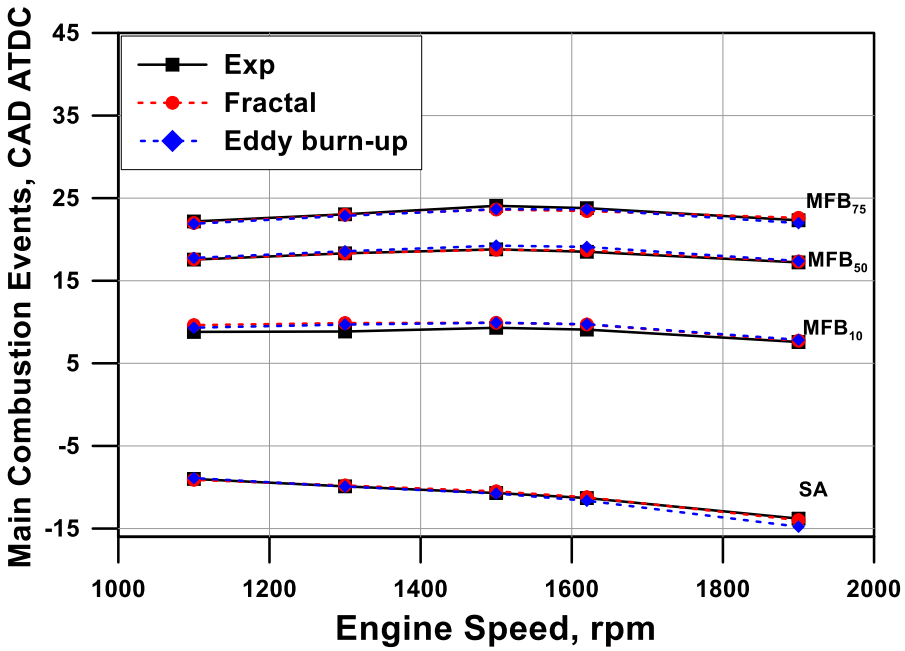

Figure 4.23 - Experimental vs numerical comparison of characteristic combustion angles at full load of both combustion models.

Table 4.7 - Identified tuning constants for fractal and eddy burn-up combustion models

Fractal	c_{trans}	1.5
	c_{wrk}	0.1
	x_{wc}	0.3
Eddy Burn-up	c_k	0.2
	c_s	3.6
	c_t	5

Model validation is then assessed in terms of global performance parameters, such as the volumetric efficiency, BSFC, in-cylinder peak pressure, etc. For sake of brevity, the validation data are here presented in terms of numerical/experimental BSFC and

maximum in-cylinder pressure comparisons, as reported in Figure 4.24 and Figure 4.25.

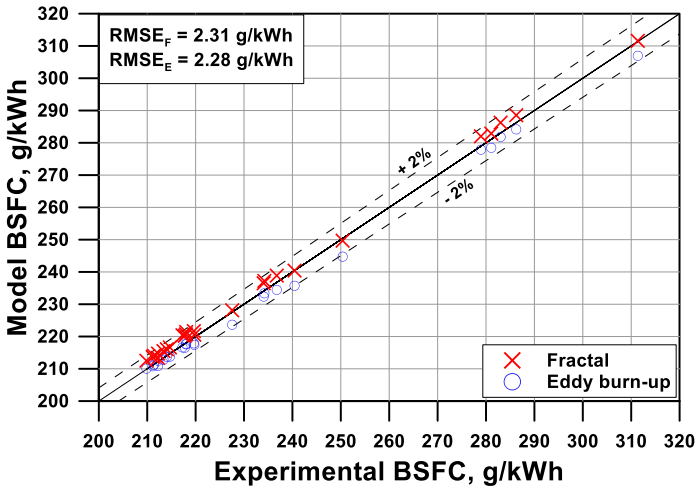

Figure 4.24 - Numerical/experimental comparison of BSFC between the two phenomenological combustion models

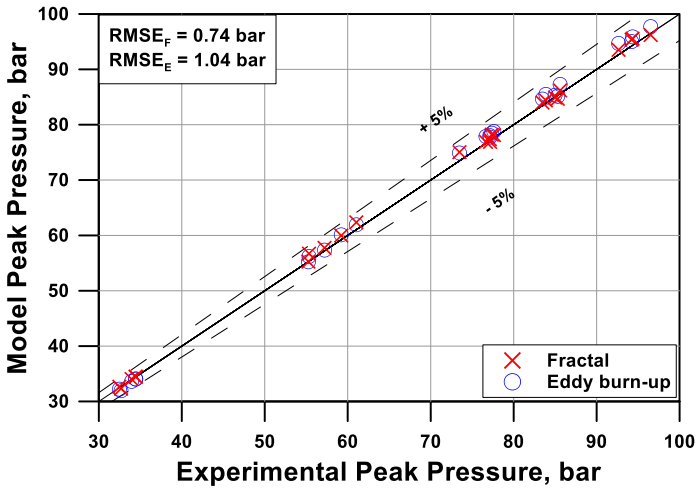

Figure 4.25 - Numerical/experimental comparison of peak pressure between the two phenomenological combustion models

Once tuned, the eddy burn-up model almost provides the same results. The eddy burn-up model denotes a good agreement with the experimental BSFC data, with a percent error within a range of ±2%, as well as the fractal model one. The model accuracy can be considered adequate to support the consistency of the analyses presented in following.

Regarding the combustion evolution, the differences between the two models can be more clearly evidenced in the next figures. To this aim, the numerical/experimental comparisons, in terms of Spark Advance, MFB_{10-50} and MFB_{10-75} are proposed in Figure 4.26, Figure 4.27 and Figure 4.28. In those figures, the fractal and eddy burn-up model outcomes are compared with the experimental data. To quantify the accuracy levels, the mean squared error on the duration of various combustion phases is computed. It can be observed that a satisfactory tuning has been effected on both models, with a similar RMSE.

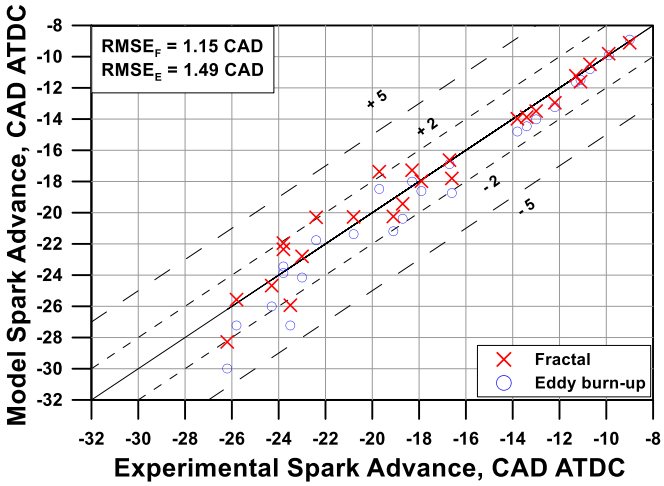

Figure 4.26 - Numerical/experimental comparison of spark advance between the two phenomenological combustion models

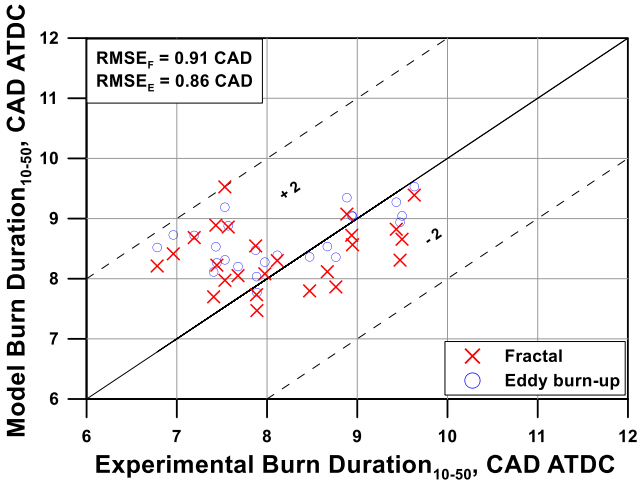

Figure 4.27 - Numerical/experimental comparison of MFB_{10-50} between the two phenomenological combustion models

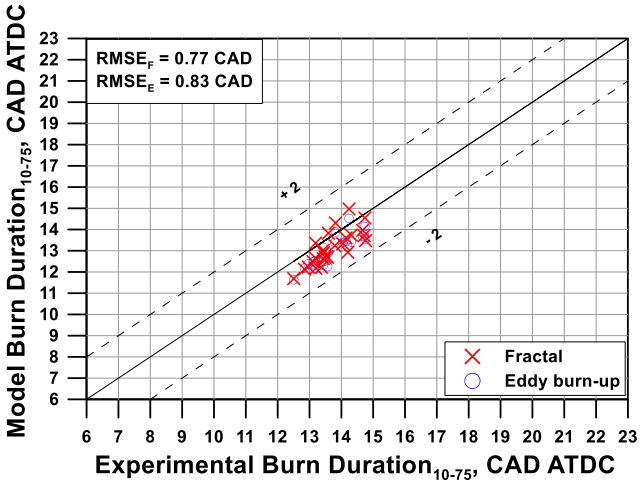

Figure 4.28 - Numerical/experimental comparison of MFB_{10-75} between the two phenomenological combustion models

As general remark, it can be underlined that the predictive capability of both combustion models is quite similar.

A further verification of the good predictive capability of both combustion models is made by the comparison between the pressure trends and burn rate resulting from the two models in Figure 4.29, Figure 4.30 and Figure 4.31. The plots confirm the good capability of both models in describing the combustion process along its whole development and completion.

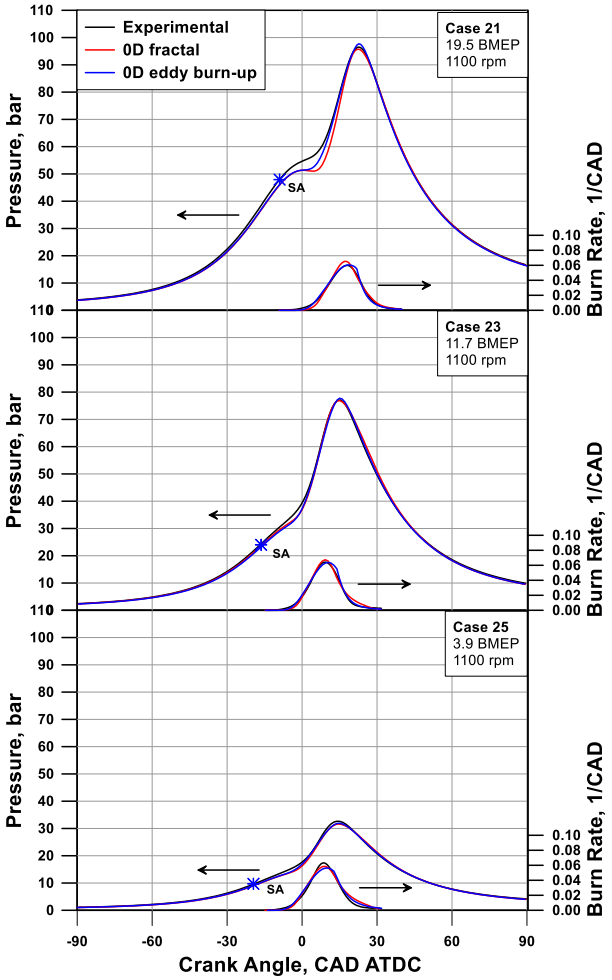

Figure 4.29 - Experimental vs numerical comparison of in-cylinder pressure traces and burn rates at 1100rpm@ 19.5 (a), 11.7 (b), 3.9 (c) BMEP.

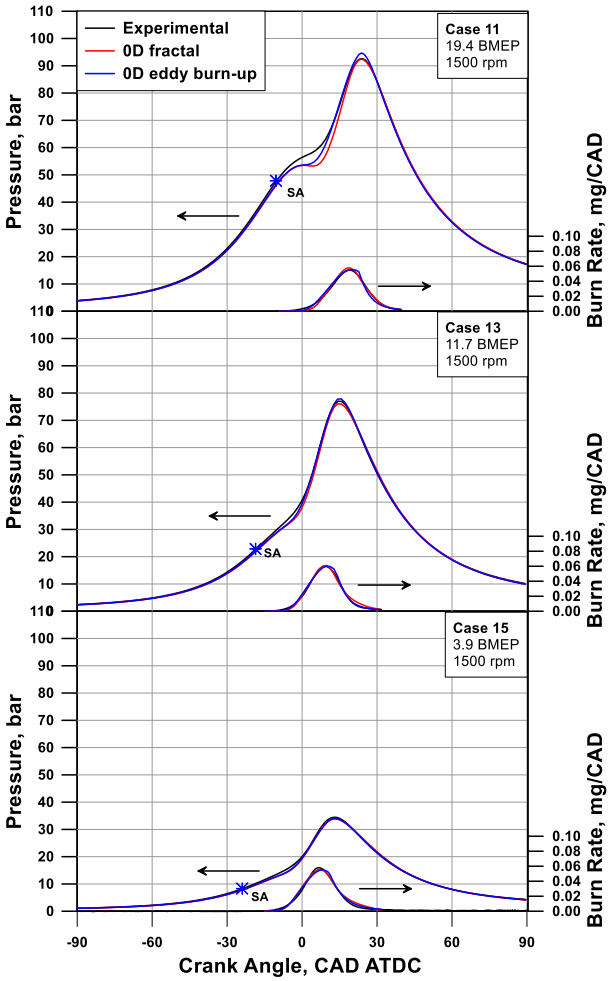

Figure 4.30 - Experimental vs numerical comparison of in-cylinder pressure traces and burn rates at 1500rpm@ 19.5 (a), 11.7 (b), 3.9 (c) BMEP.

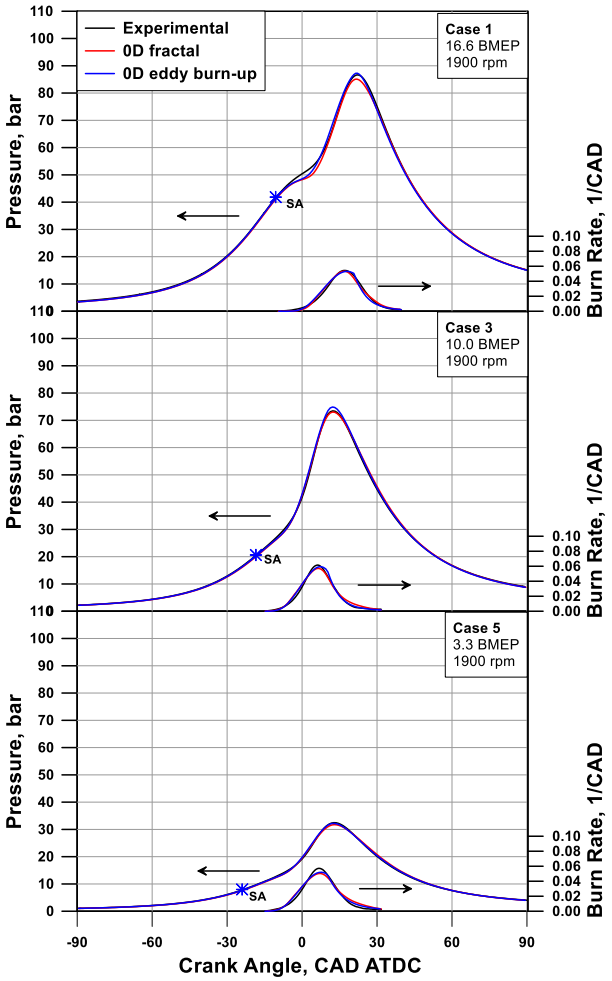

Figure 4.31 - Experimental vs numerical comparison of in-cylinder pressure traces and burn rates at 1900rpm@ 19.5 (a), 11.7 (b), 3.9 (c) BMEP.

Regarding the tuning effort, the fractal approach is simpler to calibrate since each tuning constant exerted a quite isolated effect on a single combustion process phase. The eddy burn-up model is less intuitive to calibrate, presenting a more difficult tuning effort, as a consequence of the relevant constant coupling. Despite this, the results underlined that the main combustion events are satisfactorily predicted by both models in comparison with experimental data.

4.5 Summary of the research activity on SI heavy-duty engine

The main topic of this research activity was to enhance the predictive capabilities of a fractal combustion model, through the coupling with an appropriate turbulence model suitable for large bore engines, including swirl motion interacting with the squish motion as turbulence production source in addition to tumble collapse. The developed models are adopted to simulate the operation of an SI CNG heavy-duty engine retrofitted from a CI Diesel engine, where intake port and piston shape are conceived to promote swirl motion within the cylinder.

The *K-k-T-S* turbulence model is tested for the two different engine operating conditions, and validated against 3D-CFD simulation results under motored

conditions. Despite the difficulties in describing in a 0D pattern a complex 3D flow motion, the model quite well reproduces the mean flow, tumble, swirl and turbulence intensity profiles during the phases most relevant for combustion prediction, that are intake, compression and expansion phases. A comparison between three turbulence model is described, the *K-k-ε*, *K-k-T* and the *K-k-T-S* one. The first two are surely indicated for their reduced effort in the calibration strategy but express their best only within a class of engines, the tumble-assisted one. In this case, the *K-k-T-S* turbulence model was able to obtain better results than the other two, despite the less comfortable calibration strategy. In addition, this model can be fitted for any type of engine, light- and heavy-duty.

The turbulence model is hence embedded in a phenomenological combustion model to simulate the engine behaviour under various operating conditions, different in terms of rotational speed and load. Once tuned, the fractal model accuracy was verified in terms of both global performance, combustion phasing and pressure traces against an extensive experimental dataset composed of 25 operating points. The results underlined the model capability in predicting air flow rate and BSFC, with a reasonable error band of ±2%. Concerning the pressure traces and the burn rates, the experimental/numerical agreement is satisfactory in all operating points. This also reflects in a good prediction of the main combustion events and durations. It is worth to underline that the results were obtained using a unique set of tuning constants for all the operating points, demonstrating that the physics behind the model is accurate enough to utilize it in a predictive way.

Another predictive combustion model, the eddy burn-up one, is tested to evaluate its predictive capability against the fractal approach. A detailed comparison between the two models, both coupled with the same sub-model for turbulence description, has been carried out. The proposed assessment of the combustion models underlined that their degree of accuracy is comparable. However, the fractal model showed a reduced tuning effort than the eddy burn-up one.

Reference

1. Riccardi, M., De Bellis, V., Sforza, L., Beatrice, C. et al., "Advanced Turbulence Model for SI Combustion in a Heavy-Duty NG Engine," SAE Technical Paper 2022-01-0384, 2022, https://doi.org/10.4271/2022-01-0384.
2. Lucchini, T., D'Errico, G., Paredi, D., Sforza, L. et al., “CFD Modeling of Gas Exchange, Fuel-Air Mixing and Combustion in Gasoline Direct-Injection Engines,” SAE Technical Paper 2019-24-0095, 2019, doi:10.4271/2019-24-0095
3. Sforza, L., Lucchini, T., Gianetti, G., and D'Errico, G., “Development and Validation of SI Combustion Models for Natural-Gas Heavy-Duty Engines,” SAE Technical Paper 2019-24-0096, 2019, doi:10.4271/2019-24-0096
4. Sforza, L., Lucchini, T., Gianetti, G., D'Errico, G. et al., "A 3D-CFD Methodology for Combustion Modeling in Active Prechamber SI Engines Operating with Natural Gas," SAE Technical Paper 2022-01-0470, 2022, doi:10.4271/2022-01-0470
5. Bozza, F., Teodosio, L., De Bellis, V., Fontanesi, S. et al., “A Refined 0D Turbulence Model to Predict Tumble and Turbulence in SI Engines,” SAE Int. J. Engines 12(1):2019, doi:10.4271/03-12-01-0002.
6. De Bellis, V., Bozza, F., Tufano, D., “A Comparison Between Two Phenomenological Combustion Models Applied to Different SI Engines,” SAE Technical Paper, 2017-01-2184, doi:10.4271/2017-01-2184.

5 Ultra-lean pre-chamber SI engine model validation

The second study carried out during this PhD Thesis is focused on the assessment of the turbulence and fractal combustion models on an ultra-lean active pre-chamber SI heavy-duty engine fuelled with CNG.

As well as for the conventional SI engine, the aim of this analysis is to give a contribution to the improvement of the combustion model applied to an active pre-chamber ignition system specific for SI Heavy-Duty (HD) gas engines. In this perspective, the objective of this activity is a first evaluation of the potential of the quasi-dimensional fractal combustion model in a HD gas engine, to be implemented in predictive 1D simulation tools.

5.1 Single cylinder engine description and experimental setup

The experimental testing was conducted by Lund University research team with a Direct Injection (DI) research Single-Cylinder Engine (SCE), converted from a Scania D13 6-cylinder engine, at the Combustion Engine Laboratory of Lund University.

The Table 5.1 lists the major SCE specifications. The long stroke of 160 mm, combined with the arrangement of the valves with the intake port and the combustion chamber shape, allows the SCE to obtain a charge motion level comparable to state-of-the-art series production turbocharged engines.

Table 5.1 - Single-cylinder engine specifications.

Single-cylinder pre-chamber engine	
Displaced volume, cm^3	2124
Stroke, mm	160
Bore, mm	130
Connecting Rod, mm	255
Compression ratio	12.09
Number of valves	4
Pre-chamber volume, cm^3	4.67
Pre-chamber orifices	6
Orifice diameter, mm	1.4
$A_{jet\ orifices}/V_{pre\text{-}chamber}$, cm^{-1}	0.020
$V_{pre\text{-}chamber}/V_{TDC}$, %	2.44
Exhaust Valve Open	16.4 deg bBDC

Intake Valve Close	31 deg aBDC

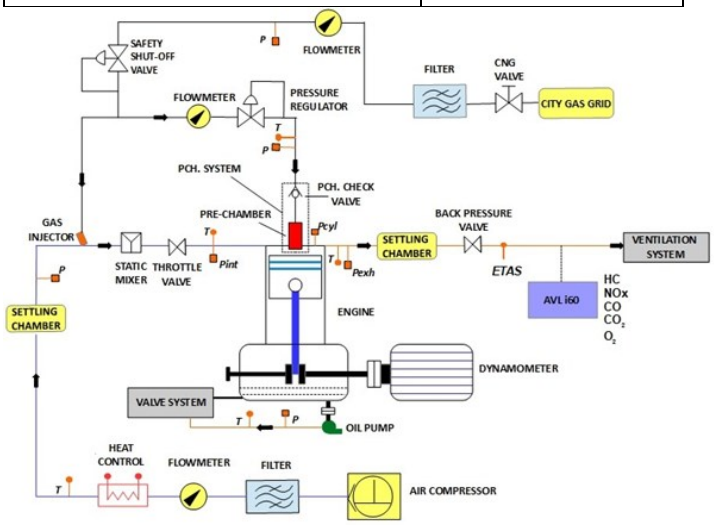

Figure 5.1 - Schematic diagram of the engine

In Figure 5.1, the SCE schematic diagram is reported, for which the pre-chamber is equipped with 6 CFD optimized holes (Figure 5.2). The pre-chamber system was installed in the single active cylinder whereas the remaining cylinders were deactivated by drilling holes in the respective pistons.

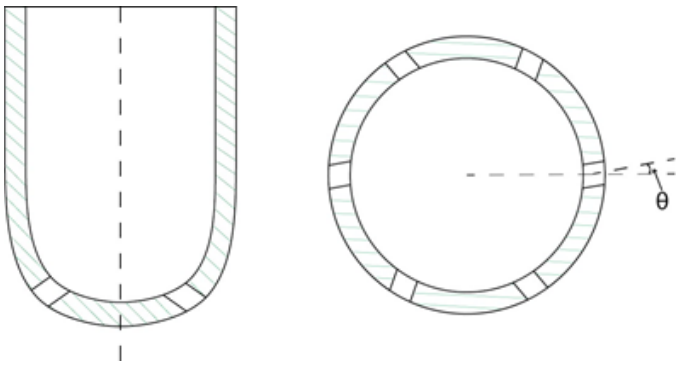

Figure 5.2 - Schematic of lower part of the pre-chamber

The pre-chamber engine is fed by CNG and the fuel is supplied to the engine both with the inlet port and directly into the pre-chamber. The gas pressure for the pre-chamber injection is kept 250 mbar higher than intake pressure using a pressure regulator. The check valve opened when the pressure difference between the supply and the cylinder exceeded 400 mbar. The fuel used in this activity was natural gas, at a pressure of 3.6 bar, from the south-west Swedish grid. Natural gas composition varies slightly over time depending on the original source. Table 5.2 shows the average and standard deviation for the time frame when the tests were carried out.

Considering the environmental condition, the intake air was supplied by an external compressor with a pressure capability up to 11 bar which guaranteed a stable source of pressure and a PID-controlled external air heater ensured stable intake air temperature with an accuracy of 0.5°C.

Table 5.2 - Fuel composition and main properties

Fluid	**Volume percentage**	**STD**
Methane CH_4	91.04 %	2.98
Ethane C_2H_6	5.06 %	1.22
Propane C_3H_8	1.80 %	0.98
i -Butane i -C_4H_{10}	0.32 %	0.15
n-Butane n-C_4H_{10}	0.47 %	0.27
i -Pentane i -C_5H_{12}	0.11 %	0.06
n-Pentane n-C_5H_{12}	0.08 %	0.05
Hexane i -C_6H_{14}	0.05 %	0.02
Nitrogen N_2	0.29 %	0.01
Carbon Dioxide CO_2	0.77 %	0.22
Fuel properties		**STD**
Methane Number [-]	76.33	8.15
LHV [MJ/Nm^3]	38.89	1.28
Normal Density [kg/Nm^3]	0.8048	0.0336

Concerning the experimental set-up, the spark timing intervals were varied from -12 CAD aTDC and exploring the widest possible interval that maintained sufficiently stable combustion. The step between different spark timings was 2 CAD, and for global λ it was 0.2. At full load, finer λ steps of 0.1 were used.

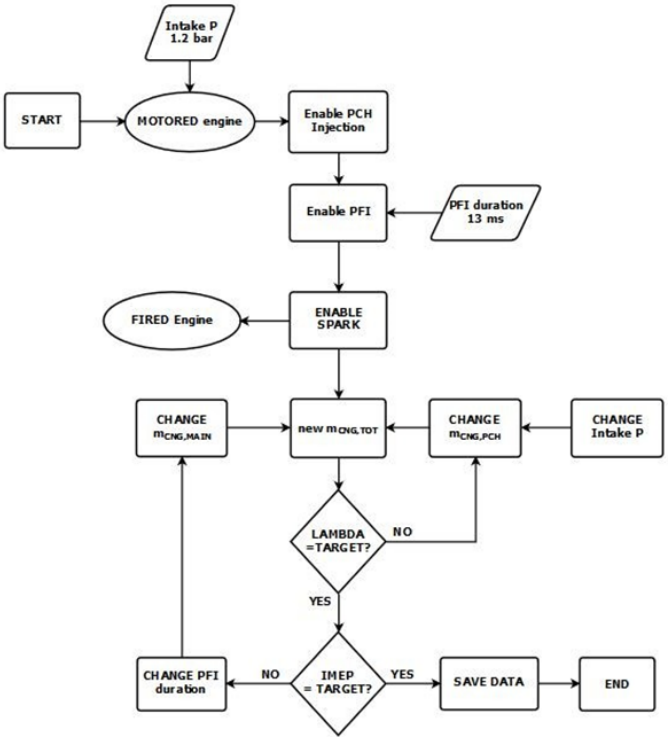

Figure 5.3 - Flow chart illustrating the test procedure

In Figure 5.3 the test procedure is illustrated by the use of a flow chart. The procedure to start the engine is to first motor the engine at the fixed inlet pressure of 1.2 bar. PFI and pre-chamber fuel are activated simultaneously and subsequently the spark.

Pre-chamber fuel flow is determined by the pressure difference between the fuel line and the cylinder. The fuel injection in the intake manifold is controlled by the PFI duration. Both PFI and DI fuel injections affect the IMEP to some extent. An iterative procedure becomes necessary: if lambda is below the target, intake pressure is increased. This affects the IMEP which, if necessary, can be adjusted using the PFI duration.

Other measurements, such as temperatures and fuel flow, were sampled every two seconds, for a total of one minute per operating point. Mean values based on these recordings were used for post processing.

The aim of this activity was to validate the model for an active ultra-lean pre-chamber engine, so the most significant operating points are evaluated. Four operating conditions that include different air-fuel ratio at the same load and different loads at the same λ were considered reasonably sufficient to assess the robustness of the fractal model applied to this engine type. Main specifics of those operating conditions are listed in Table 5.3.

Table 5.3 - Experimental specifics of the analyzed operating conditions.

Feature	C02	C08	C13	C21
λ	1.5	1.7	1.9	1.5
SA [CAD aTDC]	-10	-12	-14	-10
IMEP [bar]	10	10	10	15
Engine speed [rpm]	1500	1500	1500	1500

5.2 Engine model validation

A 1D model of the engine under study is developed within a 0D/1D modelling environment, where the engine is schematized through a network of 1D pipes and 0D volumes. The in-cylinder phenomena are described by refined, in-house developed, phenomenological sub-models for turbulence, combustion and heat transfer. In particular, the MC of the engine is schematized as a variable 0D volume, connected to the constant volume PC through an orifice. Its diameter is assigned to realize the same overall cross-sectional area as the real PC holes. Mass and energy balance equations are solved in both volumes, and a filling/emptying method is used to estimate the mass exchange between them, based on pressure difference, overall cross-sectional area, and discharge coefficient of the orifice.

The flame speed, S_L, is evaluated by a numerically-derived correlation, function of the thermodynamic state, equivalence ratio and charge dilution, detailed in [1]. This correlation was derived by 1D flame simulations for blends of methane, covering a λ range between 0.77 and 1.66. For the scope of this research activity, since the λ levels for some operating conditions (C08 and C13 of Table 5.3) exceed the above range validity, an exponential law is used to extrapolate the S_L values, in a manner similar to the method presented in [2].

Since cylinder-out emissions are evaluated a brief description of emissions models used in this research activity is mandatory. The estimation of NO_x is realized through a multi-zone approach for the burned gas. The local temperatures are applied to evaluate the time evolution of the NO_x according to the well-known extended Zeldovich mechanism [3]. The approach adopted for NO_x prediction does not consider neither nitrous oxide or prompt mechanisms, or any interaction of chemistry with turbulence. Despite the simplifications above mentioned, the methodology proved performing in an adequate manner under both stoichiometric and very lean conditions, as shown in [4]. Regarding the unburned hydrocarbons (uHC) simulation, the model considers emissions related to both filling/emptying of crevice volumes and flame wall quenching, as detailed in [5]. The estimation of uHC emission from the crevice regions is realized through a simple filling and emptying model [6], only considering as crevice the volume between the cylinder liner and the top land of the

piston ring pack. The temperature of the unburned gas trapped in this volume is imposed equal to the piston wall one, while the pressure within the crevice is supposed equal to the cylinder one. The evaluation of uHC source from flame wall quenching is achieved employing a simplified model, where the flame wall extinction distance is estimated by the correlation in [7]. During the simulation, the area swept by the flame front is determined assuming a spherical propagation of the flame front. The current version of the model does not consider the uHC formation from bulk flame quenching [8]. The partial oxidation of the uHCs from crevices and flame wall quenching is achieved according to the kinetic rate proposed in [9].

The phenomenological model was validated through comparisons with both experimental and 3D CFD data for the four engine operating points listed in Table 5.3.

5.2.1 3D-CFD/0D model comparison

Since the pre-chamber was not sensed for pressure analysis, also a comparison between 3D-CFD and 0D simulation results has been approached. Firstly, the result of in-cylinder turbulence intensity is presented, then a comparison between in-cylinder and pre-chamber pressure trends is shown.

Before showing 0D results, some details about 3D-CFD calculation procedure are mandatory. Those are carried out according to the methodology presented in [10].

First, the gas-exchange process is simulated only in the pre-chamber region from SOI-to-IVC. The aim is to correctly predict the fuel quantity remaining inside the pre-chamber after the direct injection process with minimal computational costs. Then, the whole closed-valve domain is considered for the power-cycle simulation. A flame area evolution model is used to describe the flame propagation, while a deposition model is employed to mimic the ignition.

Numerical 3D-CFD simulations are carried out by PoliMi research team with the RANS approach, and the k-ε model is used for turbulence. Two different meshes are adopted. The constant-volume gas exchange of the pre-chamber is performed on a mesh composed of 300k cells, with a general Cartesian structure. Here, the grid size inside the pre-chamber body is about 0.5 mm, with a spherical refinement around the spark-plug (0.25 mm of cell side). A similar grid size (0.25 mm) is also employed inside the nozzles, to properly capture the evolution of the flow jets. On the other hand, a jet-oriented mesh structure in the main-chamber is used to simulate the power-cycle stage. In this case, the number of cells spans from a minimum value of 390k (TDC) to a maximum of 1.3 mln (IVC), since a dynamic layering technique was adopted to accommodate the piston motion.

The first stage of the 0D model validation is focused on the turbulence intensity prediction in comparison with 3D results.

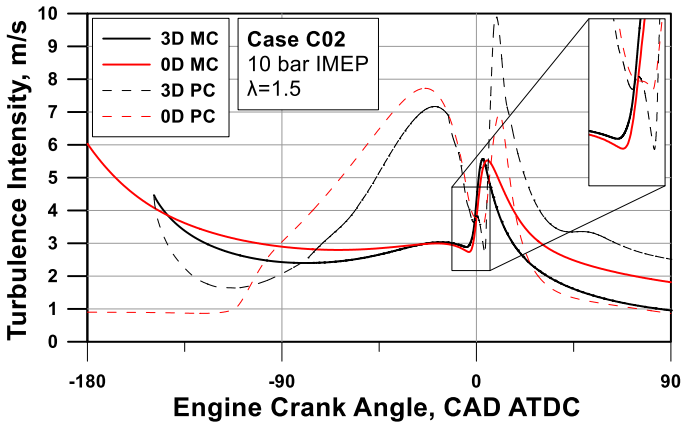

Figure 5.4 - Comparison of 0-D predicted turbulence intensities in PC and MC under fired conditions.

In Figure 5.4 a comparison between the turbulence intensity computed by the 0D model and the one resulting from the mass-averaged turbulence intensity field in the 3D-CFD model is shown during compression and half of expansion stroke. The agreement is satisfactory for the MC (continuous lines) during the compression phase and, in particular, before the firing TDC, where a typical turbulence speed-up due to the collapse of tumble motion occurs. The 0D/3D assessment is quite well taken during the combustion (between about -12 and 14 CAD) except for the very last phase. In 3D results, a tight turbulence peak in the MC is observed just after the TDC, due to the turbulence jets ejected by the pre-chamber. This turbulence production occurs in a confined space of the combustion chamber (along jet peripheries) and is averaged over the entire cylinder in the presented results. A 0D model is not able to capture this spatial inhomogeneity of the turbulence field. The 0D model is tuned to match the rising phase of the turbulence peak after TDC trend, but this choice also determines a slower decay.

Concerning the pre-chamber results (dashed lines), the turbulence increases during the compression stroke, as a consequence of the incoming flow from the main volume. The PC turbulence peak around the TDC is in good agreement with the 3D simulations. Starting from this stage, another turbulence peak arises which can be related to the incoming flow from the main-chamber.

A 5% error for average values is considered acceptable, while for instant values the margin is wider. For the purpose of combustion prediction in PC, it was necessary to focus on 0D/3D turbulence comparison in the angular range between -15 and -5 CAD, where the agreement is good. After TDC, there is a wider 0D/3D difference, but the combustion is already finished and hence this does not affect combustion model outcomes.

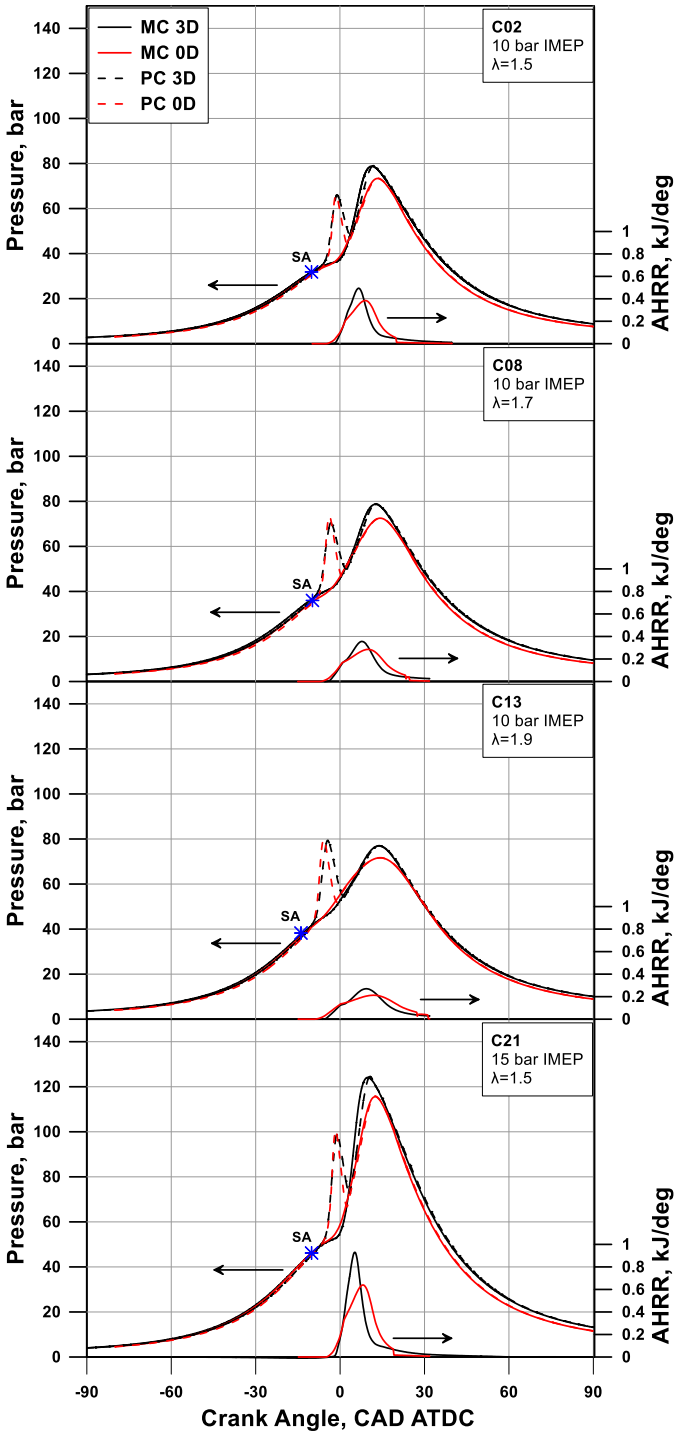

Figure 5.5 - Comparison between 3D-CFD and 0D model results of pressure and apparent heat release for all investigated conditions (Table 5.3)

In Figure 5.5 a comparison between 3D-CFD and 0D/1D pressure and apparent heat release rate profiles is shown for all test cases of Table 5.3. The black lines represent the 3D traces, whereas the red ones correspond to the 0D model outcomes. The agreement between 3D/0D pressure trends in main- (continuous line) and pre-chamber (dashed line) is satisfactory in terms of global shape, timing and peak levels for all the analysed operating points. More specifically, the 0D model pressure results in the pre-chamber quite well agrees with 3D counterparts, denoting a good

calibration of the first part of the combustion, governed by turbulent jets. This is relevant also considering that no experimental data is available about the pre-chamber.

Looking to the apparent heat release rate in the main-chamber, the 0D model well follows the slow initial burning rate of 3D simulations, whereas a systematic faster completion is predicted. This misalignment is probably related to the simplified schematization of the combustion chamber for the laminar flame area derivation adopted in 0D simulations.

5.2.2 Experimental/0D model comparison

In this section a comparison between experimental data and 0D simulation results is presented.

The comparison between experimental (black line) and 0D numerical (red line) trends of pressure cycle and burn rate in the main-chamber for all operating points of Table 5.3 is shown in Figure 5.6. In the first three cases (C02, C08 and C13) it is possible to note the effects produced by a variation of the main chamber air/fuel ratio at fixed engine load. The figures highlight that the measured trends of cylinder pressure and burn rate (normalized with the total fuel mass) are well reproduced by 0D calculations. For further information on the effects of the different parameters please refer to [11].

It is worthwhile mentioning that the combustion model parameters related to the pre-chamber are identified exclusively on the basis of previously discussed 0D/3D comparisons, without any experimental verification. Nevertheless, the first stage of the main chamber combustion, which is produced by the high-velocity jets of hot gases penetrating the chamber, appears to be accurately portrayed. This can be observed looking to the first ramp shape of the burn rate, which is rather well captured in terms of both amplitude and duration, while the second stage of the combustion process is represented by the turbulent flame propagation inside the main chamber after the depletion of the pre-chamber jets of burned gases. This is well reproduced by the simulations in the cases at λ=1.5. The model perceives the slower combustion speeds when the mixture is leaner, even if with an excessive extent.

During the turbulent combustion model calibration, the strategy was to use one set of tuning constants to reproduce all the operating points. For this reason, the above combustion results can be considered satisfactory, taking into account that no case-dependent tuning is applied. The average error on the in-cylinder peak pressure is of 4%, with a maximum error of 6% for the case C21.

In the next figures a comparison between experimental and 0D numerical results of IMEP, exhaust gas temperature, NO_x and HC emissions is shown.

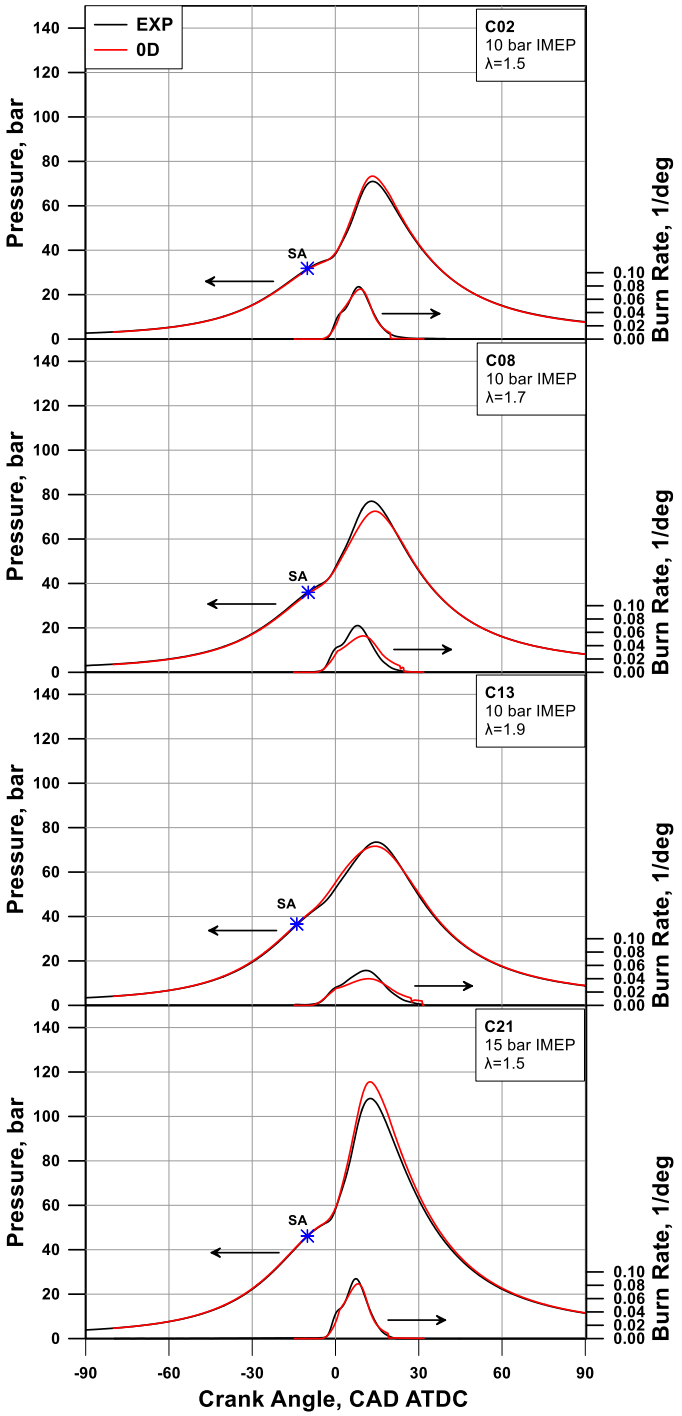

Figure 5.6 - Comparison between experimental data and 0D model results of pressure and burn rate for all investigated conditions (Table 5.3)

The globally adequate accuracy in the description of the combustion process and wall heat transfer is put into evidence by the numerical/experimental comparisons of IMEP, shown in Figure 5.7. IMEP is well predicted for cases at 10 bar IMEP, while it is slightly overestimated at 15 bar IMEP, with a RMSE equal to 0.32 bar.

As a further confirmation of the model reliability in terms of heat transfer, air/fuel ratio and combustion predictions, the numerical/experimental comparison of exhaust gas temperature is shown in Figure 5.8. As expected, the exhaust gas temperature

decreases if the mixture is leaner and increases with the engine load. In all the operating points it is well predicted, with a RMSE equal to 13.1 K

The reliability of the adopted model is further supported by the numerical/experimental comparisons of uHC and NO_x cylinder-out emissions, depicted in Figure 5.9 and Figure 5.10, respectively. HC emissions are sufficiently well predicted for almost all the operating conditions, with a global RMSE equal to 231.3 ppm. The model is able to capture HC production rising for the leanest case (C13), due to the increased contribution of the flame wall quenching. It overestimates the HC emissions in the case with higher load probably because of the error in the in-cylinder peak pressure, which leads to an excessive crevice filling of unburned mixture. Regarding NO_x emissions the accuracy is quite satisfactory for all the operating conditions, with a RMSE equal to 86.9 ppm. The model detects the higher NO_x production when the mixture is less lean and the load is higher. This is mainly related to the higher in-cylinder temperatures, which affects the NO kinetics according to the Zeldovich mechanism.

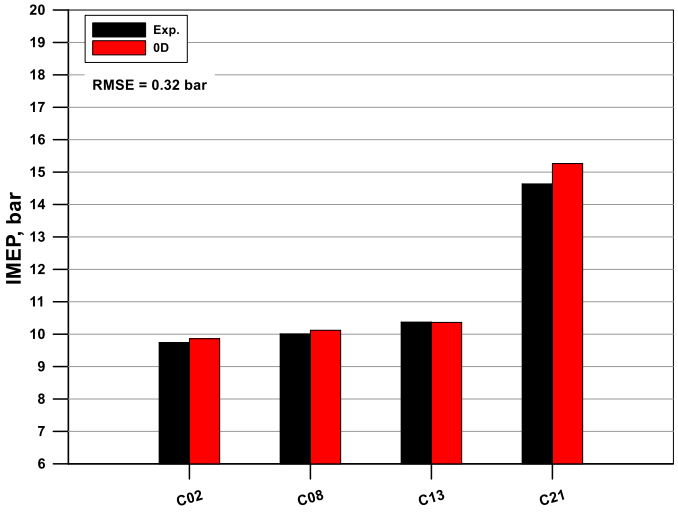

Figure 5.7 - Experimental vs numerical comparison of IMEP for all conditions (Table 5.3)

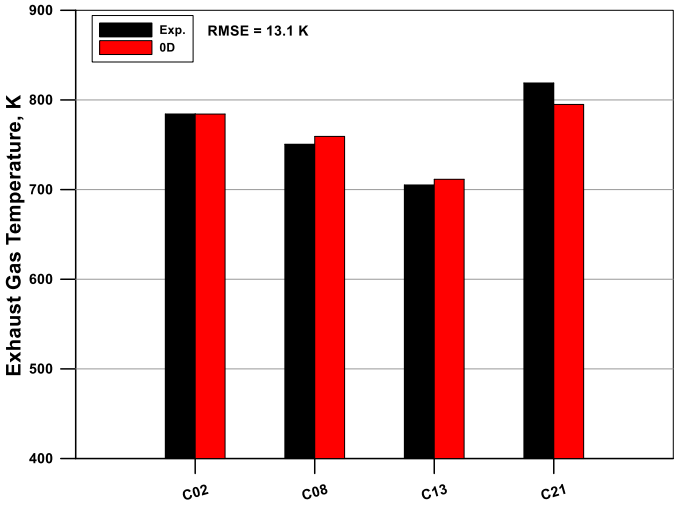

Figure 5.8 - Experimental vs numerical comparison of Exhaust Gas Temperature for all conditions (Table 5.3)

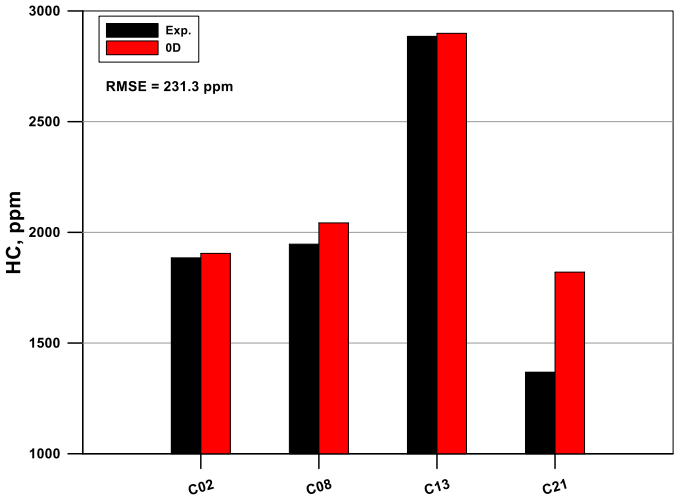

Figure 5.9 - Experimental vs numerical comparison of HC emission for all conditions (Table 5.3)

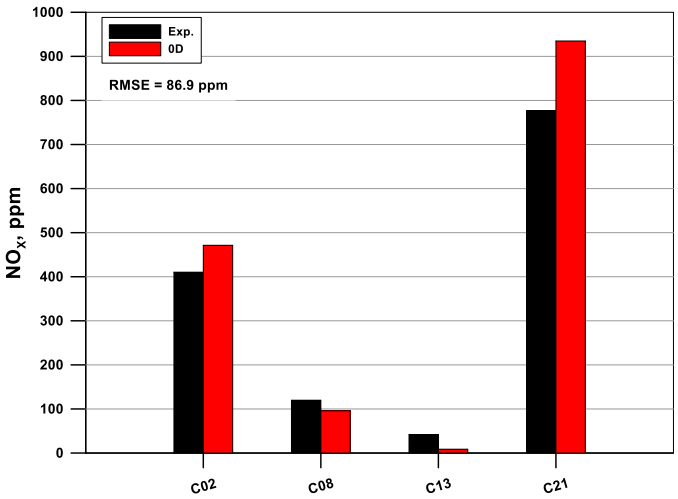

Figure 5.10 - Experimental vs numerical comparison of NOx emission for all conditions (Table 5.3)

5.3 Summary on research activity on ultra-lean active pre-chamber SI heavy-duty engine

The aim of this research activity was to prove the reliability of the already proven fractal combustion model for a new kind of engine technology for on-road engines.

In this work, a heavy-duty SI engine fuelled with CNG is studied through 1D numerical and experimental analyses. Experiments were carried out at the Combustion Engine Laboratory of Lund University with a single-cylinder engine (SCE), fuelled with CNG. The 1D simulation approach includes phenomenological sub-models describing the main in-cylinder processes, such as turbulence, heat transfer and combustion. The target is to accurately simulate the combustion process in Natural Gas SI engines with active pre-chamber utilizing considerably less CPU time and resources.

Four different operating conditions were compared at a fixed engine speed to evaluate the effects of an air/fuel ratio variation inside the main chamber, as well as the impact of load variation.

In a preliminary stage, the turbulence and combustion models were tuned with reference to 3D CFD outcomes, denoting a satisfactory accuracy in predicting pressure traces, burn rate and turbulence intensity in both main- and pre-chamber. Some criticisms emerged in the simulation of the ending combustion phase, probably due to an inaccurate estimation of the laminar flame area evolution during this phase or to a misalignment in the adopted laminar flame speed correlations.

Once tuned, the model accuracy was verified against the experimental data for all the considered operating conditions, in terms of both global performance, combustion phasing and pressure traces. The results underlined the model capability in predicting IMEP, and exhaust gas temperature, with a reasonable error band of ±4%. The NO_x and uHC emissions are also well detected by the model in most case. Concerning the pressure traces and the burn rates, model quite well agrees with the experimental counterparts, sensing both air/fuel ratio and load variations.

It is worth to underline that the results were obtained using a unique set of tuning constants for all the operating points, demonstrating that the physics behind the model is accurate enough to utilize it in a predictive way.

The 0D/1D model proposed in this activity demonstrated to be reliable and accurate for a fast design of active pre-chamber SI engines, fuelled with Natural Gas, also with a limited number of experimental data and geometrical information.

Reference

1. Bougrine S, Richard S, Nicolle A, Veynante D. “Numerical study of laminar flame properties of diluted methane-hydrogen-air flames at high pressure and temperature using detailed chemistry”, Int J Hydrogen Energy 2011;36(18): 12035–47. https://doi.org/10.1016/j.ijhydene.2011.06.053.
2. De Bellis, V., Malfi, E., Lanotte, A., Fasulo, G., Bozza, F., Cafari, A., Caputo, G., Hyvönen, J., “Development of a phenomenological model for the description of RCCI combustion in a dual-fuel marine internal combustion engine”, Applied Energy, 325: 119919, 2022, doi: 10.1016/j.apenergy.2022.119919.
3. Lavoie, G., Heywood, J.B., and Keck, J., “Experimental and Theoretical Study of Nitric Oxide Formation in Internal Combustion Engines,” Combust. Sci. Technol 1 (1970): 313- 326, doi:10.1080/00102206908952211.
4. De Bellis, V., Malfi, E., Bozza, F., Kumar, D. et al., “Experimental and 0D Numerical Investigation of Ultra- Lean Combustion Concept to Improve the Efficiency of SI Engine,” SAE Int. J. Adv. & Curr. Prac. in Mobility 3, no.4 (2021): 1993-2008. https://doi.org/10.4271/2021-01-0384.
5. Malfi, E., De Bellis, V., Bozza, F., Cafari, A. et al., “A Phenomenological Model for the Description of Unburned Hydrocarbons Emission in Ultra-Lean Engines,” International Journal of Engine Research, (2021), doi:10.1177/14680874211005063.
6. Kaplan, J. and Heywood, J., “Modeling the Spark Ignition Engine Warm-Up Process to Predict Component Temperatures and Hydrocarbon Emissions,” SAE Technical Paper 910302, (1991), https://doi.org/10.4271/910302.
7. Suckart, D., Linse, D., Schutting, E. et al., “Experimental and Simulative Investigation Of Flame-Wall Interactions and Quenching in Spark-Ignition Engines,” Automot. Engine Technol. 2 (2017): 25-38, doi:10.1007/s41104-016-0015-z.
8. Ishikawa, N., “Bulk and Wall Flame Quenching in Nonuniform Concentration Fields,” Combustion and Flame 56, no. 3 (1984): 251-259, doi:10.1016/0010-2180(84)90059-2.
9. Westbrook, C.K., Dryer, F.L., “Simplified Reaction Mechanisms for the Oxidation of Hydrocarbon Fuels in Flames”. Combust. Sci. Technol., 27:31–43, 1981, doi:10.1080/00102208108946970.
10. Sforza, L., Lucchini, T., Gianetti, G., D'Errico, G. et al., "A 3D-CFD Methodology for Combustion Modeling in Active Prechamber SI Engines Operating with Natural Gas," SAE Technical Paper 2022-01-0470, 2022, https://doi.org/10.4271/2022-01-0470
11. Onofrio, G., Li, C., Garcia Valladolid, P., De La Morena, J. et al., “Experimental and Numerical Assessment of Active Pre-chamber Ignition in

Heavy Duty Natural Gas Stationary Engine," SAE Technical Paper 2020-01-0819, 2020, doi:10.4271/2020-01-0819.

6 Conclusion

In this research activity, two heavy-duty SI engines, both fuelled with CNG, are numerically investigated, through a hierarchical simulation-level approach. The first is a diesel-derived SI heavy-duty engine, while the second one is an innovative ultra-lean active pre-chamber heavy-duty engine.

Since heavy-duty CNG SI combustion system are derived from Diesel configuration, some features of the flow-field are retained, as certain swirl level and zero or very low tumble. The main topic of the research activity is focused on the developing of an advanced turbulence model fitted firstly for the above-mentioned SI heavy-duty engine, then suitable for any kind of engine technology.

The first step was to analyse the in-cylinder fluid dynamic of the SI heavy-duty engine under exam, to better recognize all the vector components of the in-cylinder flow. It was known that many forms of ordered motion had a part, but just one played a crucial function. The *swirl* motion, in fact, was the main driver of the turbulence intensity production due to shear stresses and its interaction with *squish* flow motion.

Subsequently, the second step was to create an ad hoc turbulence model for this type of engine, which at the same time could be used for any engine technology, both tumble- and swirl- assisted.

The ultimate result is the so-called *K-k-T-S* turbulence model, which considers not only an equation for the kinetic energy of the mean flow, *K*, one of the turbulent flow, *k*, and one for the specific angular momentum of the tumble motion, *T*, but also an equation for the specific angular momentum of the swirl motion, *S*. This model is suitable for any type of engine, just properly calibrating its tuning constants.

The *K-k-T-S* turbulence model is then validated against 3D-CFD simulation results under motored conditions.

The *K-k-T-S* model is then compared to a code embedded in the commercial software GT-Suite, the *K-k-ε* model, and to the *K-k-T*, a previous step of the model developed during this research activity, which does not consider the *swirl* motion as possible source of turbulence intensity. The comparison reported that *K-k-T-S* model is the most suitable for the engine under exam while the other two models are surely indicated for their reduced effort in the calibration strategy but express their best only within a class of engines, the tumble-assisted one. In the present case, the *K-k-T-S* turbulence model was able to obtain better results than the other two, despite the less comfortable calibration strategy. In addition, this model can be fitted for any type of engine.

Once the turbulence model is tested and validated, the heavy-duty SI engine, it is coupled with a quite-standard version of the fractal combustion model, as user

procedure, to evaluate global performance, combustion phasing and pressure traces against an extensive experimental dataset composed of 25 operating points. Regarding the pre-chamber engine architecture, an enhanced version of the fractal model is used, considering all the basic phenomena occurring in an engine fitted with a PC.

To this aim, a 1D model of the above described engines was developed according to its main features, within a 0D/1D modelling environment.

Following that, both engine models were tuned and validated based on 3D calculations and experimental data, by selecting a single set of tuning constants. The SI heavy-duty engine was validated against 25 operating points, predicting with a reasonable error band of ±2% the tested engine performance parameters, such as combustion phasing, air flow rate or BSFC. Regarding the pressure traces and the burn rates, the experimental/numerical agreement is satisfactory in all operating points.

For the pre-chamber engine, the numerical results were verified against 4 operating conditions, which cover different loads and air/fuel ratios. The results underlined the model capability in predicting IMEP, and exhaust gas temperature, with an allowable error band of ±4%. The NO_x and uHC emissions are also well detected by the model in most case. Concerning the pressure traces and the burn rates, model quite well agrees with the experimental counterparts, sensing both air/fuel ratio and load variations.

The results obtained demonstrated that with the enhanced fractal model it is possible to reliably predict both the engine architectures, with a unique engine-dependent set of tuning constants. These outcomes further strengths the robustness of the fractal approach, leading to the conclusion that that the physics behind this model is accurate enough to allow its use in a predictive way.

Despite these excellent results, a slight improvement of the combustion model is considered to be obtained with an appropriate modelling of the kernel development, ensuring a milder characterization of the first phase of combustion. This is much more important for the assessment of gaseous fuel combustion, as it is slower than the usual fossil-derived fuels.